NOAA Technical Report NOS 106
Charting and Geodetic Services Series CGS 2

Prediction and Correction of Propagation-Induced Depth Measurement Biases Plus Signal Attenuation and Beam Spreading for Airborne Laser Hydrography

Rockville, Md.
August 1984

U.S. DEPARTMENT OF COMMERCE
National Oceanic and Atmospheric Administration
National Ocean Service

NOAA Technical Report NOS 106
Charting and Geodetic Services Series CGS 2

Prediction and Correction of Propagation-Induced Depth Measurement Biases Plus Signal Attenuation and Beam Spreading for Airborne Laser Hydrography

Gary C. Guenther
Nautical Charting Division
and
Robert W. L. Thomas
EG&G/Washington Analytical Services Center

Rockville, Md.
August 1984
Reprinted July 1986

U. S. DEPARTMENT OF COMMERCE
Malcolm Baldrige, Secretary

National Oceanic and Atmospheric Administration
Anthony J. Calio, Assistant Administrator

National Ocean Service
Paul M. Wolff, Assistant Administrator

Office of Charting and Geodetic Services
R. Adm. John D. Bossler, Director

Mention of a commercial company or product does not constitute an endorsement by NOAA (NOS). Use for publicity or advertising purposes of information from this publication concerning proprietary products or the tests of such products is not authorized.

CONTENTS

ABSTRACT.....1

1.0 INTRODUCTION.....2

2.0 SIMULATION DESCRIPTION.....5
2.1 Background.....5
2.2 Simulation Mechanics.....6
2.2.1 Definitions and Procedures.....6
2.2.2 Downwelling Distribution.....11
2.2.3 Impulse Response at a Distant Receiver.....11
2.2.4 Inhomogeneous Media.....16
2.2.5 Program Validation.....16
2.3 Simulation Outputs.....18
2.4 Actual Response Functions.....22

3.0 SPATIAL RESULTS.....25
3.1 Bottom Distribution.....25
3.2 Horizontal Resolution.....28
3.3 Upwelling Surface Distribution.....29
3.4 Receiver Field of View.....29

4.0 ENERGY AND PEAK POWER RELATIONSHIPS.....35
4.1 Introduction.....35
4.2 Signal Energy.....35
4.2.1 Nadir Entry.....36
4.2.2 Off-Nadir Entry.....42
4.3 Signal Power.....45
4.3.1 Impulse Response Results.....56
4.3.2 Environmental Response Results.....51

5.0 BIAS PREDICTION.....58
5.1 Methodology.....58
5.2 Bias Computation.....58
5.3 Bias Sensitivities.....63
5.4 Bias Variation.....81
5.5 Formal Bias Description.....94

6.0 BIAS CORRECTION.....96
6.1 Introduction.....96
6.2 Extrapolated Backscatter Amplitude.....98
6.3 Bottom Return Pulse Width.....101
6.4 Bias Correction Conclusions.....105

7.0 CONCLUSIONS.....107

8.0 ACKNOWLEDGMENTS.....109

9.0 REFERENCES.....109

APPENDIX A. Bias Tabulation.....112

Prediction and Correction of Propagation-Induced Depth Measurement Biases plus Signal Attenuation and Beam Spreading for Airborne Laser Hydrography

Gary C. Guenther
NOAA/National Ocean Service
Rockville, Maryland 20852

and

Robert W. L. Thomas
EG&G/Washington Analytic Services Center
Riverdale, Maryland 20737

ABSTRACT. Monte Carlo simulation techniques have been applied to underwater light propagation to calculate the magnitudes of propagation-induced depth measurement bias errors as well as spatial beam spreading and signal attenuation for airborne laser hydrography. The bias errors are caused by the spatial and subsequent temporal dispersion of the laser beam by particulate scattering as it twice traverses the water column. Beam spreading results dictate spatial resolution at the bottom and the receiver field-of-view requirement. Sample temporal response functions are presented. The pulse energy and peak power attenuation relationships developed can be used to predict maximum penetration depths. Predicted depth measurement biases are reported as functions of scanner nadir angle, physical depth, optical depth, scattering - phase function, single-scattering albedo, and receiver field of view for several diverse signal processing and pulse location algorithms. Bias variations as a function of unknown (in the field) water optical parameters are seen to be minimized for certain limited ranges of nadir angles whose values depend on the processing protocol. Bias correctors for use on field data are reported as functions of nadir angle and depth.

1.0 INTRODUCTION

The basic premise of airborne laser hydrography is that the water depth can be determined by measuring the round-trip transit time for a short duration light pulse. The pulse is envisioned as travelling to the bottom and back to the surface along a fixed path at a known angle from the vertical. This simple model does not take into consideration the spatial and temporal spreading of the beam in the water caused by scattering from entrained organic and inorganic particulate materials.

Analytical computations by Thomas and Guenther (1979) indicated the existence of a significant depth measurement bias toward greater depths for operations of an airborne laser hydrography system at nadir. The bias arises from a lengthening of the total integrated path length due to the multiple-scattering transport mechanism by which the laser radiation spreads as it traverses the water column. This is the so-called "pulse stretching" effect. For off-nadir beam entry angles, the assumed or "reference" path is the unscattered ray in the medium (see Fig. 1) generated by Snell's Law refraction at a flat surface. There is a propensity for the core of the downwelling energy distribution to be skewed away from this path toward the vertical into the so-called "undercutting" region, due to the fact that the average path length is shorter, and hence the attenuation is less. The energy returning from this region tends to arrive at the airborne receiver earlier than that from the reference path for the same reason. This causes a depth measurement bias toward the shallow side. These two opposing biases superpose to yield depth estimates which, although they depend on water optical properties, are generally biased deep for small beam entry nadir angles and shallow for large nadir angles. The net biases can greatly exceed international hydrographic accuracy standards.

The key to quantification of the effects of scattering is the generation of a set of response functions for the propagation geometry which characterize the temporal history of radiation reaching the receiver for an impulse input. Although various analytic approximations can be achieved via simplifying assumptions, the actual formal problem is effectively intractable due to the complexity of the multiple scattering. Monte Carlo simulation is a practical

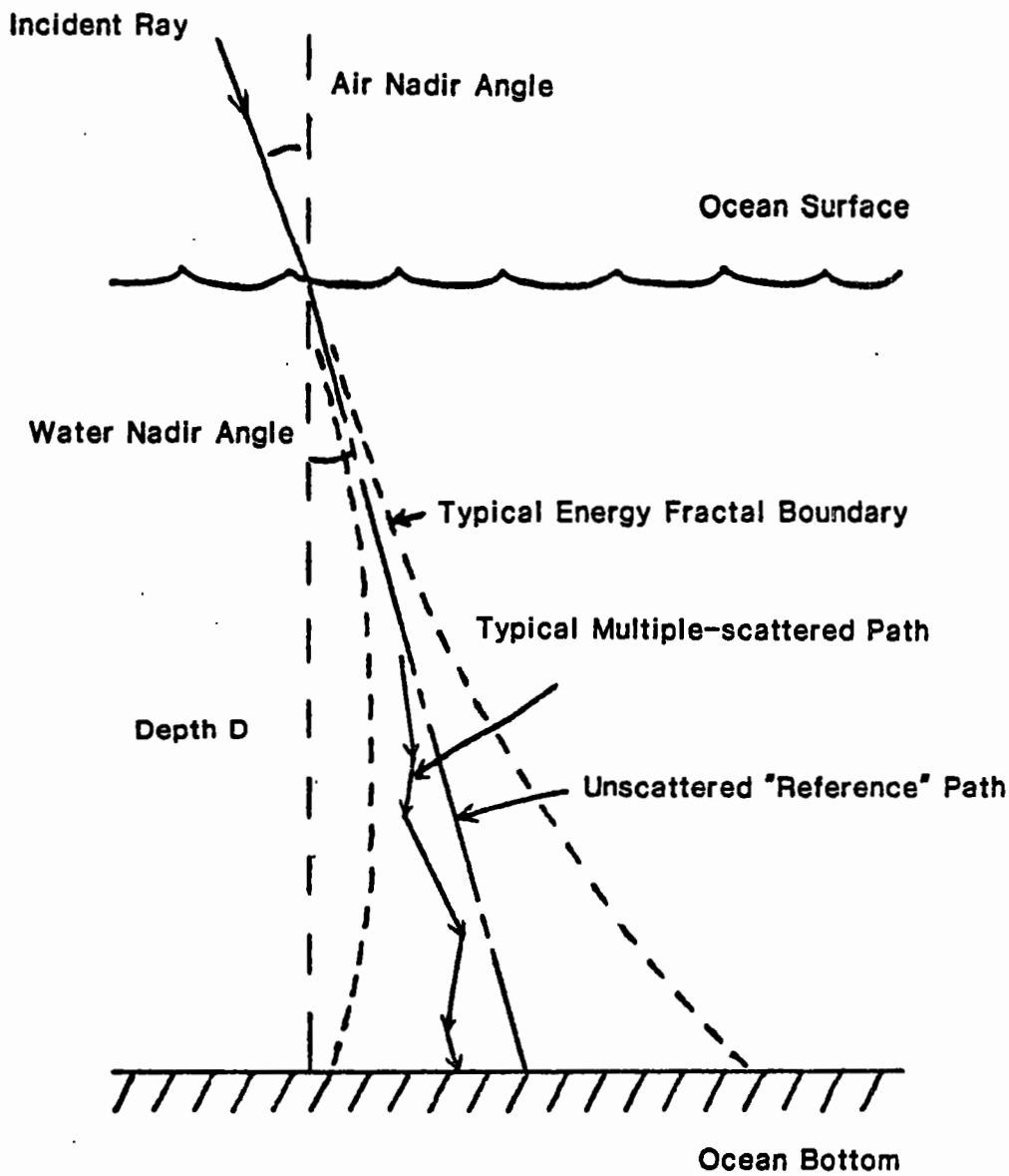

FIGURE 1. SCATTERING GEOMETRY

method of generating the needed impulse response functions (IRFs). A powerful new Monte Carlo simulation technique has been developed and exercised to model the effect of underwater radiative transfer processes on airborne lidar signals for impulse laser inputs to homogenous and inhomogeneous water columns. The water parameters and systems constraints of the computations are appropriate to airborne laser hydrography systems presently under consideration for use in coastal waters. Simulation results include full sets of spatial and temporal distributions. Horizontal resolution at the bottom and receiver field-of-view requirements are derived from the spatial results.

The impulse responses from the simulation have been convolved with a realistic source pulse to yield expected bottom return signal characteristics, the so-called environmental response functions (ERFs) at a distant, off-nadir airborne receiver. Appropriate volume backscatter decay has been added to the leading edge of each ERF. Depth measurement biases have been estimated by applying realistic signal processing and pulse location algorithms to the augmented ERFs. Resulting outputs are pulse shapes, peak power, and, most importantly, depth measurement bias predictions. Bias sensitivities to input parameters are examined in detail.

It is important that the propagation-induced depth measurement biases be accurately calculated, because if the predicted biases do exceed an acceptable magnitude, they can, at least conceptually, be applied to field data as bias correctors in post-flight data processing to maintain system performance within the error budget.

2.0 SIMULATION DESCRIPTION

2.1 Background

Preliminary simulation results were reported in Guenther and Thomas 1981a and 1981b. Dr. H. S. Lee (1982) pointed out that for off-nadir operation, the methodology did not model the effect of geometric variation in the length of the air path to the receiver across the exit spot at the water/air interface. Since it was not possible with the given approach to obtain the necessary spatial/temporal distribution of bottom reflected energy at the surface, a modified technique for calculating the off-nadir receiver impulse response functions was developed.

In the original version, the downwelling response was digitally convolved with a slightly modified version of itself to produce the round-trip temporal response function. This function correctly represents the ensemble of returning photons at the water/air interface and also the return at a distant receiver for nadir operation. Because of varying air-path lengths across the exit spot to a distant off-nadir receiver, however, a set of separate upwelling response functions across the exit spot is required for calculation of the off-nadir receiver response functions. A new solution was developed which independently preserves both temporal and spatial information by pairing each individual downwelling photon path with all (or a selected set of) other paths. For selected receiver fields of view, the known temporal length of the air path from the surface to the receiver for each path pair is added to the associated water transit time to yield a combined, total transit time. The FOV functionality is an added side benefit which was not previously available.

The net effect of this modification is to permit the earlier arrival of a portion of the energy scattered back toward the aircraft into the "undercutting" region due to a shorter air path. This in turn causes the resultant biases to be somewhat more in the shallow direction than previously calculated, by an amount which increases with increasing off-nadir angle. The newly derived biases and bias functionalities are reported herein.

Additionally, the previously reported bias results for processing procedures planned for the U. S. Navy's Hydrographic Airborne Laser Sounder (HALS) system -- the log/difference/CFD protocol (Guenther 1982) -- were based on the simplifying assumption that the effect of the volume backscatter energy preceding the bottom return is negligible. This assumption was questionable for some of the "dirtier" water clarity conditions expected in coastal waters and undoubtedly led to a certain amount of error in the bias predictions. The HALS processing procedure for simulation data has now been upgraded to include the volume backscatter signal appropriate to each respective ERF, and the biases reported herein fully reflect those expected under field conditions.

2.2 Simulation Mechanics

In the Monte Carlo approach, the transport of photons to the bottom is modeled as a series of individual, random scattering and absorption events in the water column. Spatial and temporal distributions of photons arriving at the bottom are accumulated over a large number of representative paths. These distributions are then manipulated analytically to produce the estimated response at a distant airborne receiver.

2.2.1 Definitions and Procedures

Traditionally, the mean free path for radiation transport through water is described through a parameter called the "narrow-beam attenuation coefficient", $\alpha(\lambda)$, which is compromised of two components: scattering and absorption. If "s" is the scattering coefficient and "a" is the absorption coefficient, then $\alpha(\lambda) = a(\lambda) + s(\lambda)$. The values of these water optical properties depend strongly on wavelength, λ. For coastal waters, the minimum attenuation occurs in the green portion of the visible spectrum. Airborne bathymetric lidar systems operate in the green in order to maximize depth penetration potential. In this report, the wavelength dependence of the water parameters will not be explicitly shown, and all reported numeric values will be appropriate for green wavelengths If a monochromatic beam of radiance, N_0, is incident on a column of water, then the amount that remains neither scattered nor absorbed after travelling a distance, d, is $N_0 \exp(-\alpha d)$.

Since the mean of the exponential occurs at $\alpha d = 1$, the mean free path, q, is equal to α^{-1}. The vertical "optical depth" of the medium, defined as the number of mean free path lengths required to vertically traverse the medium to the bottom for a depth, D, is D/q which is thus equal to αD.

In the simulation, the distance between scattering events is assumed to be exponentially distributed with a "mean free path", q. Individual path lengths, L, are generated from the expression $L = -q \ln \rho$, where ρ is a rectangularly distributed random number in the interval (0,1).

The "albedo for single scattering", ω_0, is the average fraction of the incident energy at each scattering event that is not absorbed: i.e., $\omega_0 = (\alpha - a)/\alpha = s/\alpha$. For typical coastal waters, ω_0 ranges from about 0.55 to 0.93 at green wavelengths. In the simulations, photons are not actually eliminated by absorption as they might be in the real world. Following the method of Plass and Kattawar (1971), their behavior is represented by retaining photon weights (initially unity) which are multiplied by a vector of ω_0 values at each scattering event. In this way, the photons are not removed from the simulation, and results can be conveniently accumulated for many values of ω_0 at the same time.

Photons change direction at all scattering events. The scattering angle ψ from the incident direction is generated according to the "phase function", $P(\psi)$, which defines the probability that the photon will scatter into a unit solid angle at ψ. Since the solid angle between ψ and $\psi + d\psi$ is $2\pi \sin\psi \, d\psi$, the probability of occurrence of ψ in that range is $p'(\psi)d\psi = 2\pi \sin\psi \, P(\psi) \, d\psi$. Note that the phase function is simply the "volume scattering function" normalized to exclude specific water clarity conditions by dividing by the scattering coefficient, "s". The random value of each simulated scattering angle, ψ_k, is generated by calculating and tabulating the cumulative probability for a given phase function as a function of ψ and sampling the interpolated results with values of ρ, where ρ is another rectangularly distributed random number between 0 and 1.

Typical phase functions for water at green wavelengths (Petzold 1972) exhibit very strong forward scattering. For the lidar simulations, two bounding phase functions for coastal waters designated "NAVY" or "clean" (Petzold HAOCE-5) and "NOS" or "dirty" (Petzold NUC-2200) were utilized. As seen in Fig. 2, these phase functions increase by a factor of more than 1,000 as the scattering angle diminishes from 10 to 0.1 degrees. The cumulative distribution functions in Fig. 3 demonstrate that roughly a quarter of the scattering occurs at angles of less than 1° and that three-fourths occurs under 10°. Scattering results both from opaque inorganic particles and translucent organics. Size distributions vary widely with location. The large forward scattering observed indicates that the dominant scatterers are inorganics of over micron size as well as organics of various sizes (Gordon 1974).

The "inherent" parameters α, ω_0, and $P(\psi)$, along with D, are the independent descriptors of the transport medium characteristics required as inputs by the simulation and are thus also the optical properties upon which the biases are ultimately parameterized. The relationships between these parameters and the parameters governing the "apparent" properties of the medium have been discussed by Gordon, Brown, and Jacobs (1975). The most important apparent optical parameter is $K(\lambda)$, the so-called "diffuse attenuation coefficient," which is defined as the fractional rate of decay of the downwelling flux with depth. For small depths, K depends on both the depth itself and the angle of incidence of the radiation at the surface; but for larger depths these dependences become very small, and K approaches an asymptotic value. The ratio, K/α, as seen in Fig. 4 for typical natural waters, is a monotonically decreasing function of ω_0, which has a value of unity when ω_0 is zero and which decreases to zero as ω_0 tends to unity (Timofeyeva and Gorobets 1967, Prieur and Morel 1971). There are small dependences on the phase function and optical depth, but these are unimportant for applications in coastal waters.

The energy loss of the downwelling beam as a function of depth, and hence the maximum useable "penetration" depth for a laser system, is most easily described in terms of K. In a similar fashion, K dictates the intensity and rate of decay of the volume backscatter signal preceding the bottom return.

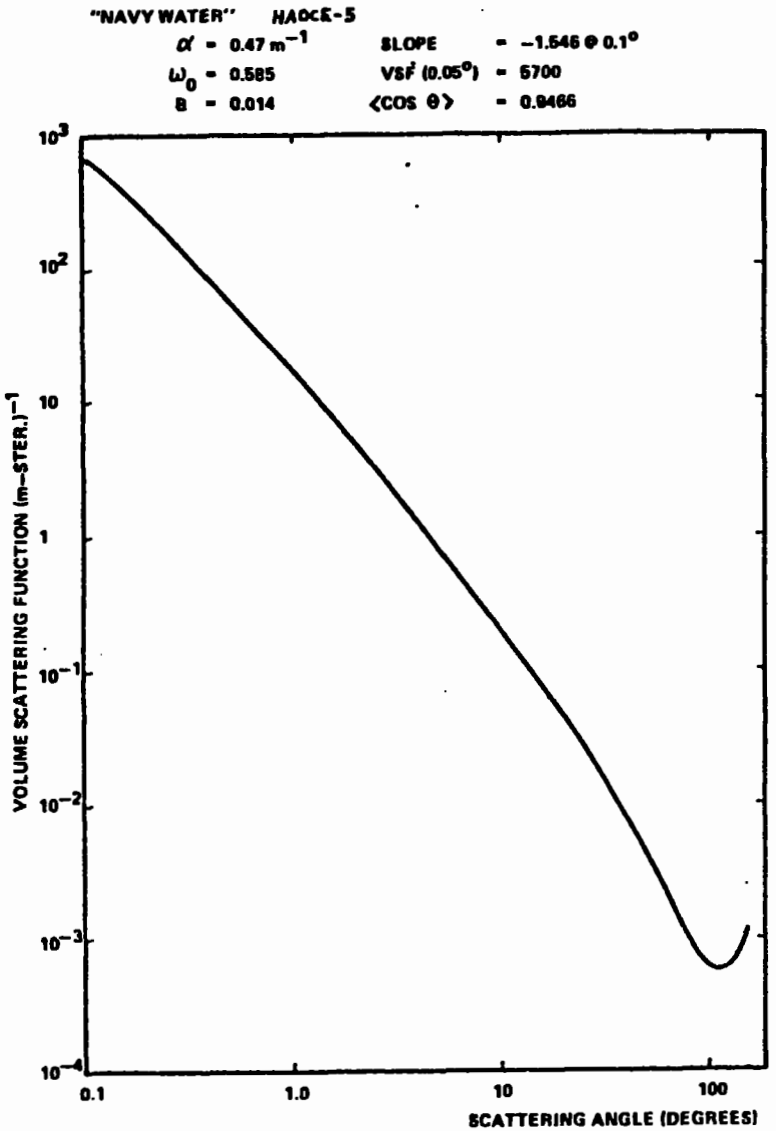

VOLUME SCATTERING FUNCTION FOR 'CLEAN' OR 'NAVY' WATER

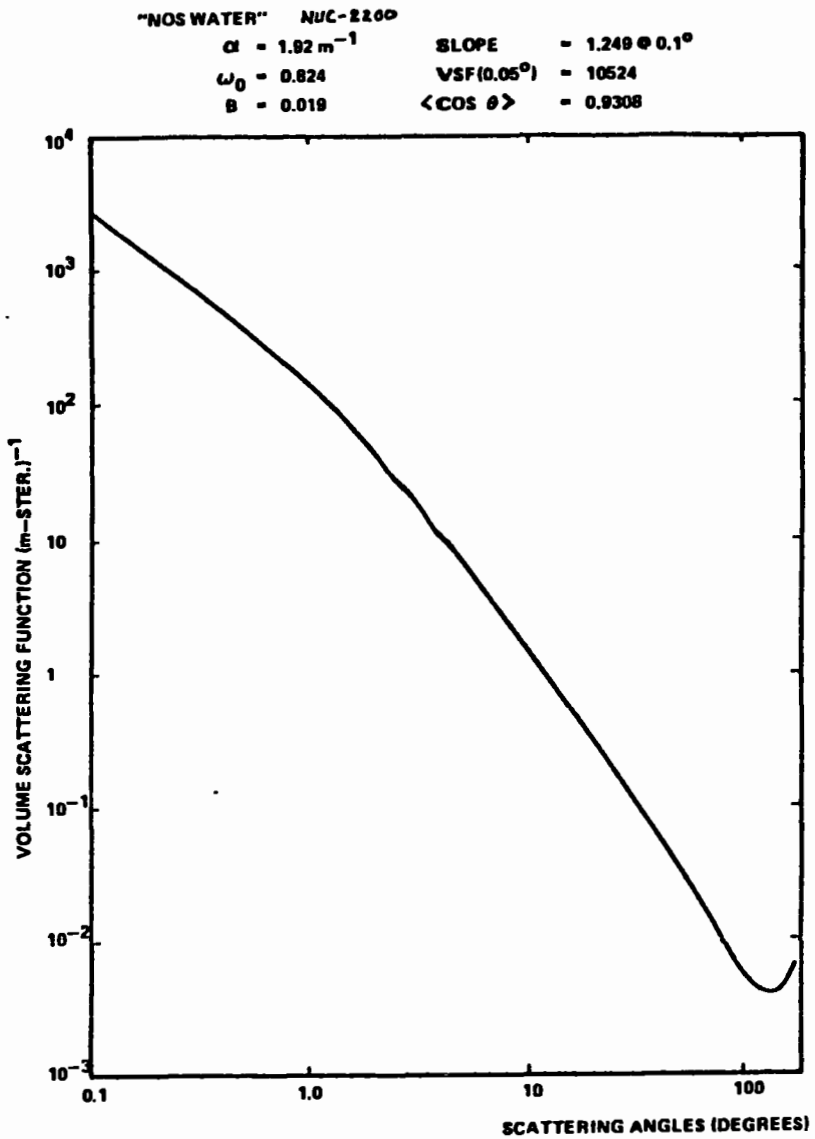

VOLUME SCATTERING FUNCTION FOR 'DIRTY' OR 'NOS' WATER

FIGURE 2. TYPICAL VOLUME SCATTERING FUNCTIONS (PETZOLD 1972)

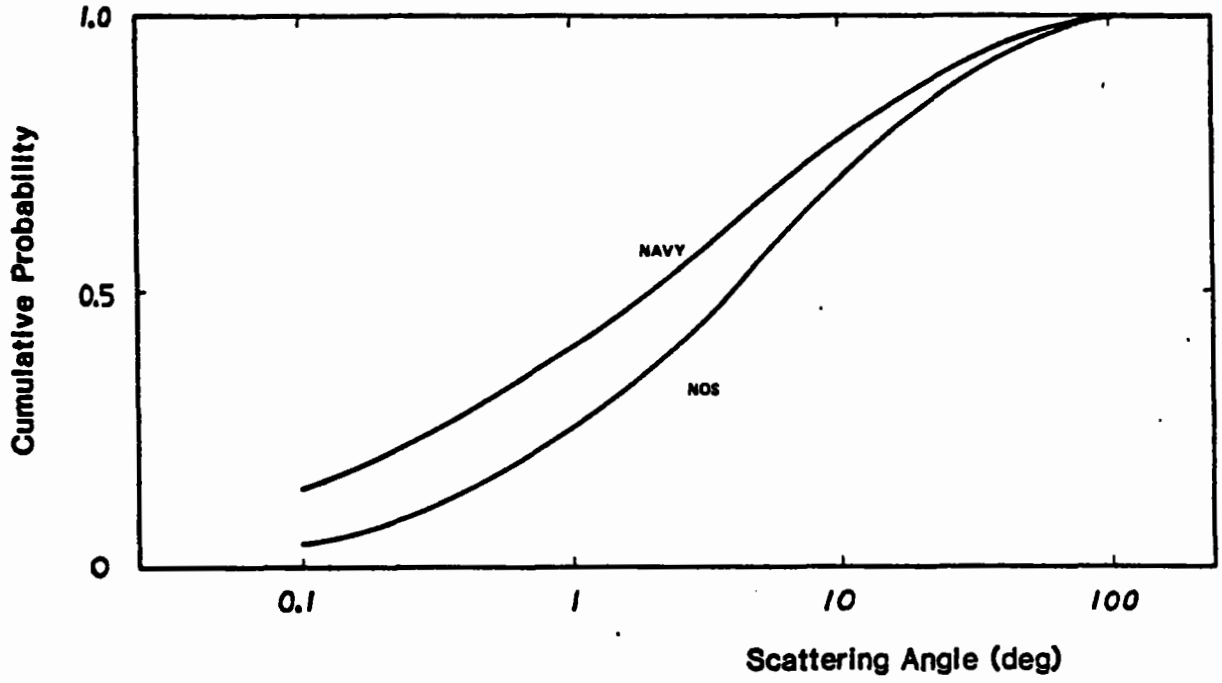

FIGURE 3. PHASE FUNCTION CUMULATIVE DISTRIBUTION

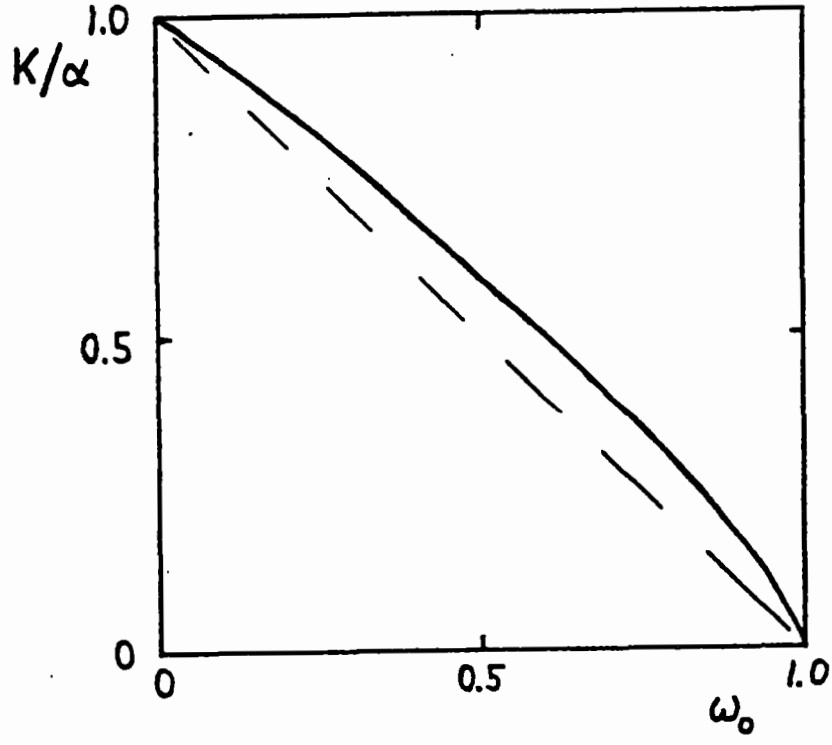

FIGURE 4. DEPENDENCE OF K/α ON SINGLE-SCATTERING ALBEDO

The biases, however, are not functionally dependent on K or KD, but rather on αD or $sD=\omega_0 \alpha D$. Combinations of α and ω_0 which produce the same value of K do not yield the same biases.

2.2.2 Downwelling Distributions

Spatial, temporal, and angular distributions of downwelling photons are accumulated at each of a series of optical depths between 2 and 16 as photons pass through these various levels. In this way, results for a complete set of bottom optical depths are generated in a single run. The lengths of the photon paths for photons reaching the bottom are summed to allow an evaluation of the associated time delay. The minimum time of transit to the bottom is $t_w = D/c$, where c is the velocity of light in water. The time "delay" for paths of length L_i is then computed as $t_D = \Sigma L_i/c - t_w$. By performing this computation for a large number of downwelling photons, the downwelling impulse response function $d(t_D)$ is accumulated as a histogram representing the distribution of arrival times of photons incident on the bottom. For simulations intended to produce power and depth measurement bias results, which need not conserve total energy, photons accruing delays of greater than a quarter or a half of the depth transit time (depending on the nadir angle) were terminated to save computer time because they would contribute only to the extended tail of the temporal distribution.

An important gain in the information content of the results arises from the realization that, for given values of αD and ω_0 all temporal results scale linearly with the depth. This is illustrated in Fig. 5 where representative photon paths are shown for two cases with the same αD but with different values of D. The photon paths for the two cases are geometrically "similar" so that the fractional time delays, t_D/t_w, are identical. The absolute time delays thus scale linearly with D, and one set of normalized response functions can be used to generate absolute results for all depths.

2.2.3 Impulse Response at a Distant Receiver

Several techniques were considered for completing the simulation to a distant airborne receiver. The direct, geometric approach of tracking photon paths to a distant receiver after a round-trip path through the water was

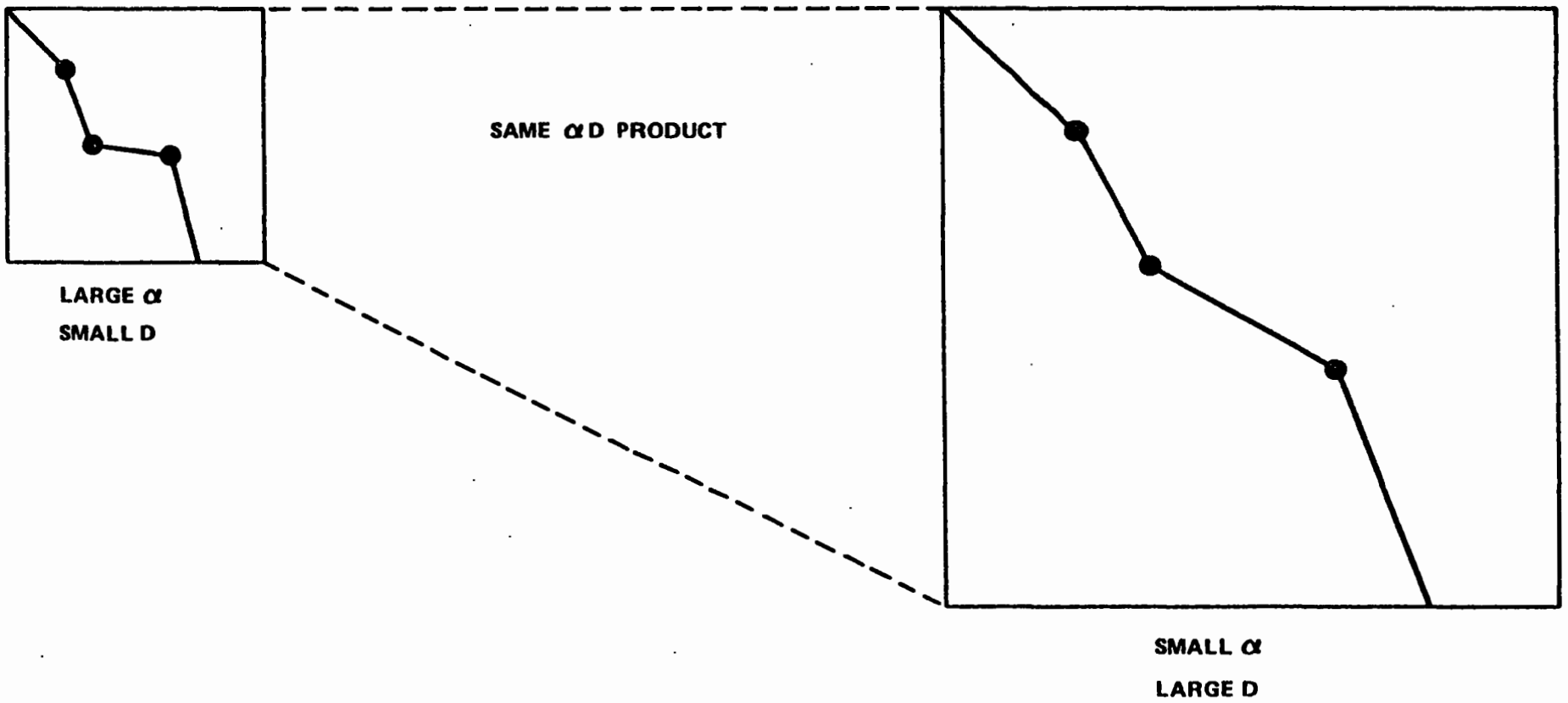

FIGURE 5. ILLUSTRATION OF SCALING RULE FOR DIFFERENT DEPTHS

considered impractical because the very low probability of such events would lead to excessive computer usage. A sometimes useful technique involving "virtual" photons, termed the "method of statistical estimation" by Spanier and Gelbard (1969), involves the calculation and summing at each scattering event of weighted scattering probabilities in the direction of the distant receiver. This approach was attempted, but lead to noisy, irreproducible behavior for as many as 10^5 incident photons due to the highly peaked nature of the Petzold coastal phase functions. (The method was moderately successful with broader phase functions such as the "KB" function favored by Gordon, Brown, and Jacobs (1975) for clear ocean water.)

The round-trip impulse response function (IRF) in the water can be computed from the downwelling distributions using the principle of "reciprocity" (Chandrasekhar 1960). Reciprocity is a statement of symmetry or reversibility which, when applied to airborne lidar, implies that the ensemble of viable scattering paths in the water is identical for downwelling and upwelling radiation, because the exiting photons must leave the medium in the opposite direction from which they entered in order to reach the distant receiver colocated with the laser source. In other words, reciprocity requires that the statistical ensemble of the unmodelled upwelling paths in the direction of a distant receiver for photons reflected at the bottom be identical to that for the simulated downwelling paths from a colocated transmitter. This is not a declaration that the downwelling and upwelling paths are physically identical, but rather that the set of simulated downwelling photon tracks can be regarded as representative for both cases. The subset of the downwelling paths utilized by upwelling radiation is determined by the weighting function for the bottom reflection.

To obtain a round-trip impulse response function in the water, the computed impulse response $d(t_D)$ for downwelling transport can be convolved digitally over the upwelling distribution, $u(t_D)$. For an assumed Lambertian bottom reflection distribution, the upwelling distribution is computed by multiplying the weights of downwelling photons reaching the bottom by the cosine of their arrival nadir angles. The convolution result is the round-trip IRF at the water/air interface. This result, however, does not include the subsequent variation in the air-path length to the distant receiver across the upwelling surface distribution. This is an important effect which

significantly alters the shape of the IRF, except perhaps at nadir where the air-path variation is not as great, and it cannot be neglected. For off-nadir angles, the shortest total round-trip path, as seen in Fig. 6, is no longer the one including a vertical path to the bottom, but rather, due to the shorter air path, one in which the photons arrive at the bottom closer to the aircraft. Thus, highly scattered energy which would have returned in the trailing edge of the IRF actually defines the leading edge. With the convolution approach, the temporal response varies in an unknown manner across the upwelling distribution, and the distant receiver IRF cannot be calculated.

In order to calculate the IRF at a distant, off-nadir receiver, one must know the time history of each returning photon and its location in the upwelling surface distribution. This can be accomplished by using the concept of reciprocity in a slightly different, more discrete way. As before, the simulated downwelling paths are judged to be representative of the upwelling paths for photons which will exit the water in the direction of the receiver, and specific upwelling paths are selected by Lambertian (cosine) weighting of the downwelling paths. Rather than implicitly computing the effect of all possible path pairings of the downwelling photons by convolution, one can form each possible path pair directly, as seen in Fig. 7 for two sample paths. Propagation delay times of paired paths are combined with their appropriate geometric air-path delays from the surface exit location to the receiver. For selected fields of view, historgams of these total transit delay times are formed to produce the receiver IRFs.

Since the set of all possible path pairs is not statistically independent, a smaller subset of these pairs can be used (to save computer time) with very little loss in information. Several variations of photon number and pairing combinations were examined in order to find the most cost-effective approach. Reported results are based on 1000 downwelling photon paths paired with a block of 25 randomly selected upwelling paths for a total of 25,000 round-trip paths. This is a minimum acceptable number, as the resulting IRFs are somewhat noisy for cases of high attenuation, i.e., concurrent low ω_0 and high αD. A larger number of photons and/or pairings would be beneficial, but a much larger set would be required to significantly improve performance.

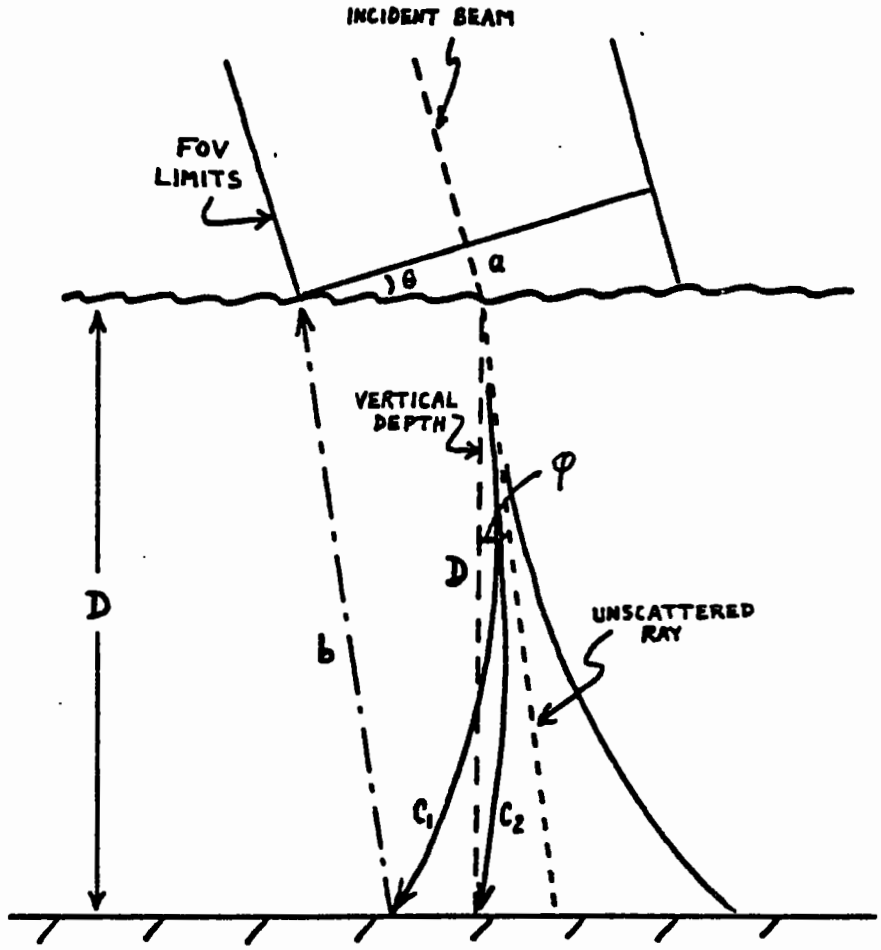

$$C_1 + b < C_2 + D + a$$

FIGURE 6. AIR PATH GEOMETRY

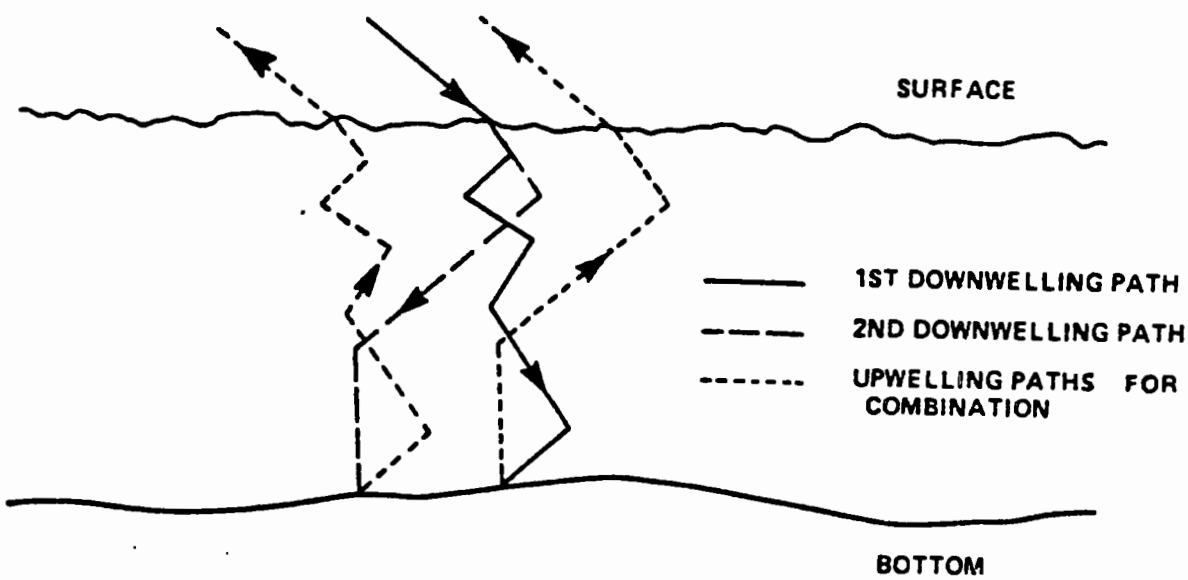

FIGURE 7. PATH PAIRING EXAMPLE

2.2.4 Inhomogeneous Media

The simulations were primarily performed for homogeneous water in which the density and nature of the scattering particles are independent of depth. It is well known, however, that significant departures from homogeneity occur frequently in coastal waters. It was important, therefore, to assess the error magnitudes caused by using homogeneous case biases when significant departures from homogeneity occur. The existing Monte Carlo simulation program was modified (Guenther and Thomas 1981c) to permit simultaneous estimation of impulse response functions for several exaggerated vertical distributions of scatterers and absorbers, as seen in Fig. 8. The resulting IRFs were digitally convolved with a 7-ns triangular source pulse to produce the "environmental response functions" (ERFs). Linear fractional threshold pulse locators were applied to the ERFs to determine the biases and the differences in bias errors between the homogeneous case and the various inhomogeneous models. The biases, even for these extreme inhomogeneities, were found to differ from those of the homogeneous case by less than 10 cm. The simulation results for homogeneous waters are thus considered to be sufficiently representative for typical natural coastal waters.

2.2.5 Program Validation

Because of the complexity of the scattering processes and geometry, it is believed that analytic calculations can provide only approximations, and that Monte Carlo simulation is the most direct approach and provides the most accurate computation of the impulse response functions. The program must, therefore, be validated on the basis of ancillary outputs which can be compared with known quantities or relationships.

The Monte Carlo laser hydrography simulation is an extension of an existing program whose various modules were debugged and validated through extensive application to atmospheric scattering problems. Modifications were made primarily to the scattering functions and geometry. It was thus important to confirm known facts such as that the downwelling flux decays exponentially with optical depth and that the rate of decay is appropriate for the given optical properties. As seen in section 4.2, the functionality between K/α and ω_0 derived from the simulation was found to be in excellent

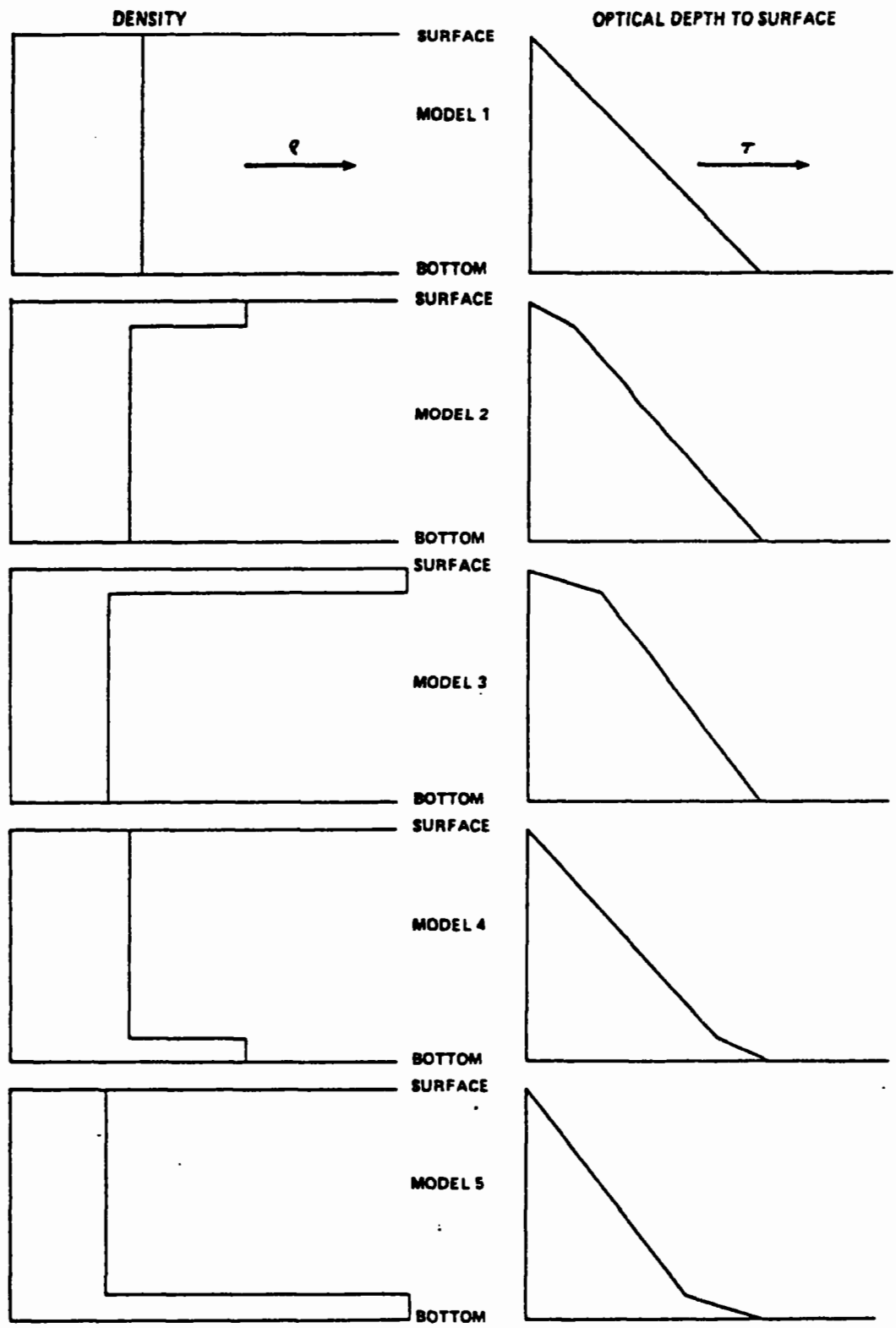

FIGURE 8. SCATTERING PARTICLE DENSITY AND OPTICAL DEPTH TO THE SURFACE

agreement with experimental data from Timofeyeva and Gorobets (1967) and the theory of Prieur and Morel (1971). In addition, the spatial and temporal distributions are consistent with simplified analytic propagation models; and the subsequently derived biases for nadir entry are in good agreement with the analytic estimates of Thomas and Guenther (1979). These successful predictions lend credence to the overall results.

Sufficient photons were simulated to insure that the standard error in sampled quantities, such as energy in the IRF time bins, was generally less than ten percent, regardless of the random number sequence, for parameter ranges of interest. Results for ω_0=0.4 did not meet this criterion and were rejected from further use. High αD IRFs with ω_0=0.6 were also slightly noisier than desired.

2.3 Simulation Outputs

For each of the two phase functions, six simulation runs (with nadir angles in air of 0, 10, 15, 20, 25, and 30 degrees) were performed, for a total of twelve runs. To ensure comprehensive results sets, simulations over full ranges of αD (2 - 16) and ω_0 (0.6 - 0.9) were run for each case. Five values of optical depth and three values of single-scattering albedo were employed in each simulation run so that 15 sets of results were generated in each run. Spatial and temporal bottom distributions were printed for each case. A data base containing 180 normalized impulse response functions, each resolved into 50 time bins, has thus been created.

Typical IRFs are seen in Figs. 9, 10, and 11. Much of the evident simulation noise will be smoothed out by subsequent convolution with a typical source pulse, as seen in the following section. The abscissae are in units of vertical transit time, t_w. The conversion to actual time, which is depth dependent, is $t(ns) = 4.44\ t_w\ D(m)$. The IRF widths thus scale linearly with depth. For the "NAVY" phase function and a single-scattering albedo of 0.8, Fig. 9 shows the effect of nadir angle for a fixed optical depth of 8, while Fig. 10 presents a progression of optical depths at a 20° nadir angle. The effect of single-scattering albedo is seen in Fig. 11. The durations of the IRF leading and trailing edges are seen to increase substantially as nadir angle, optical depth, and single-scattering albedo increase.

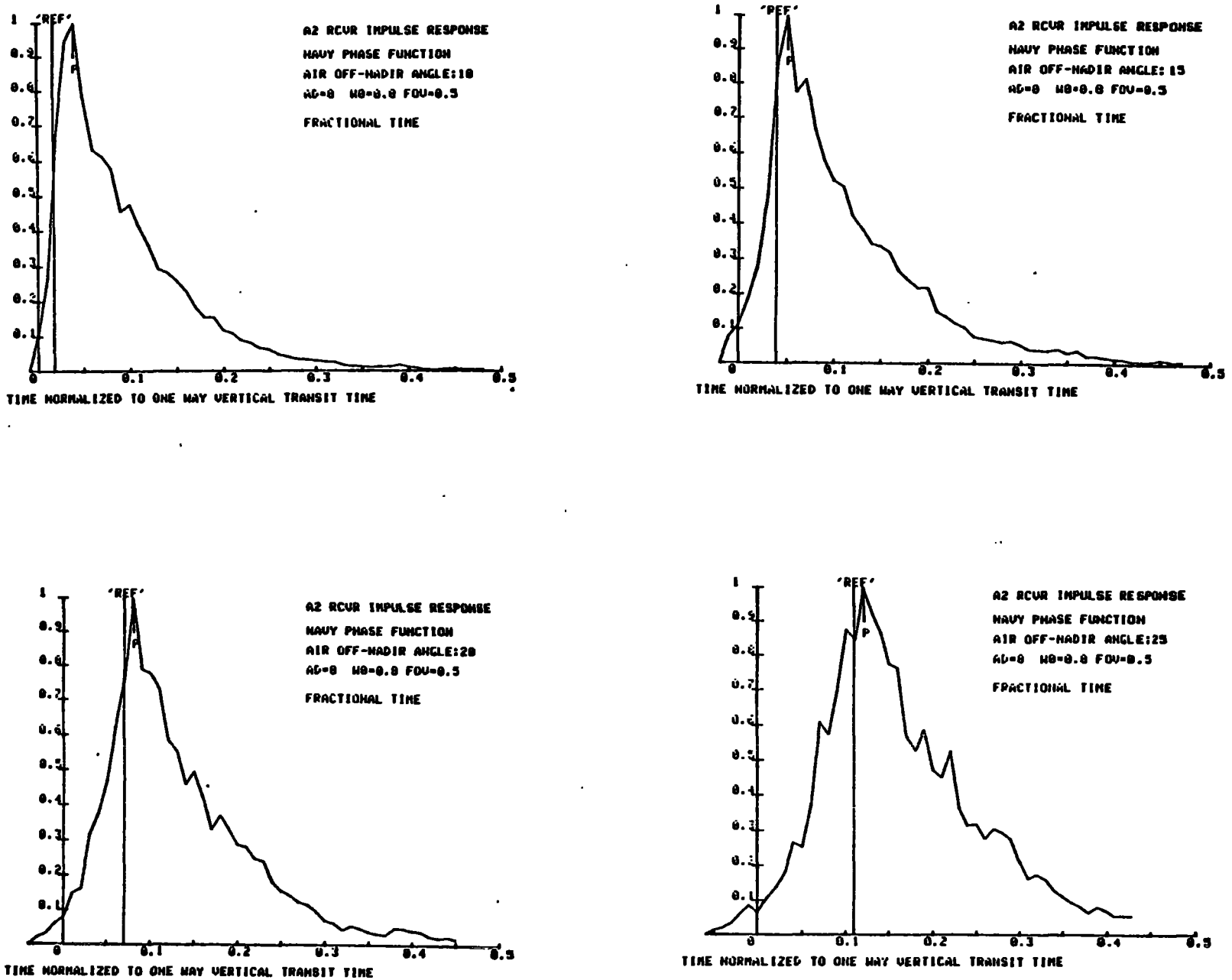

FIGURE 9. IMPULSE RESPONSE FUNCTIONS FOR VARYING ANGLES

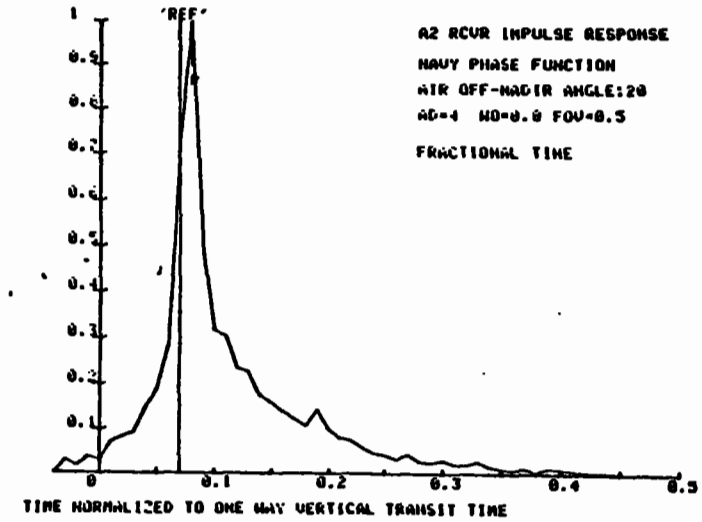

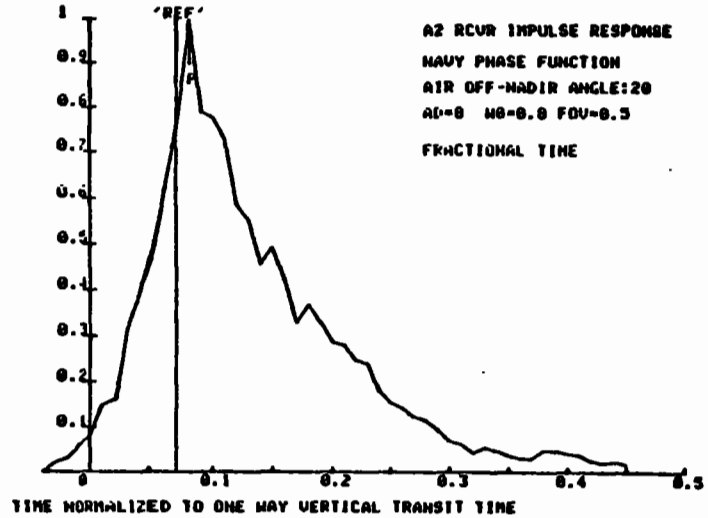

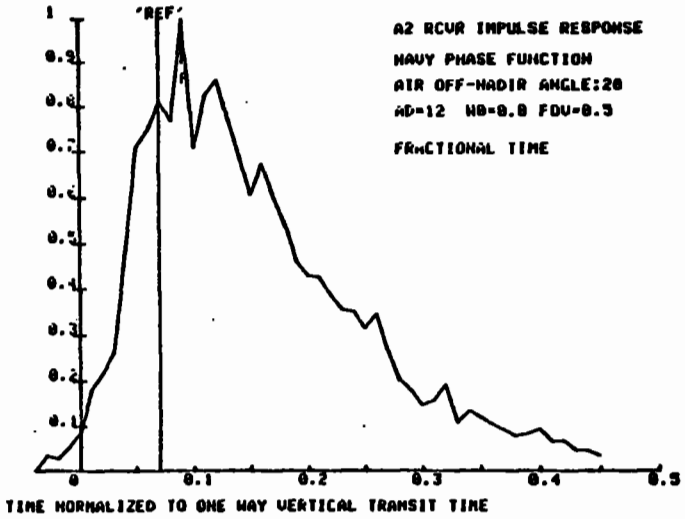

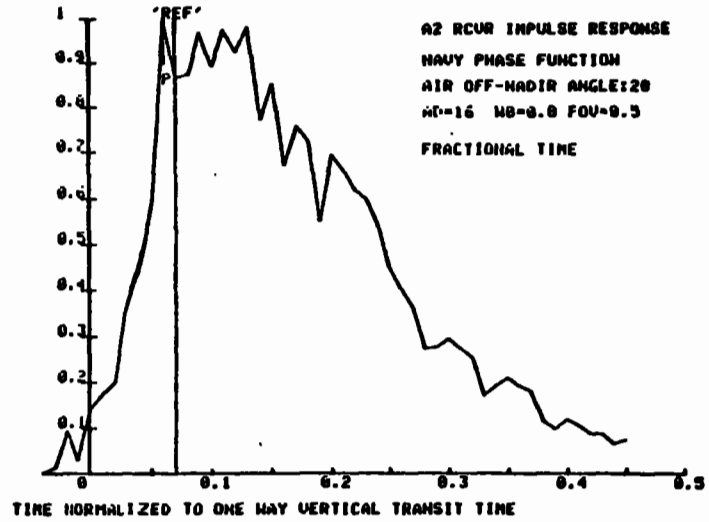

FIGURE 10. IMPULSE RESPONSE FUNCTIONS FOR VARYING OPTICAL DEPTHS

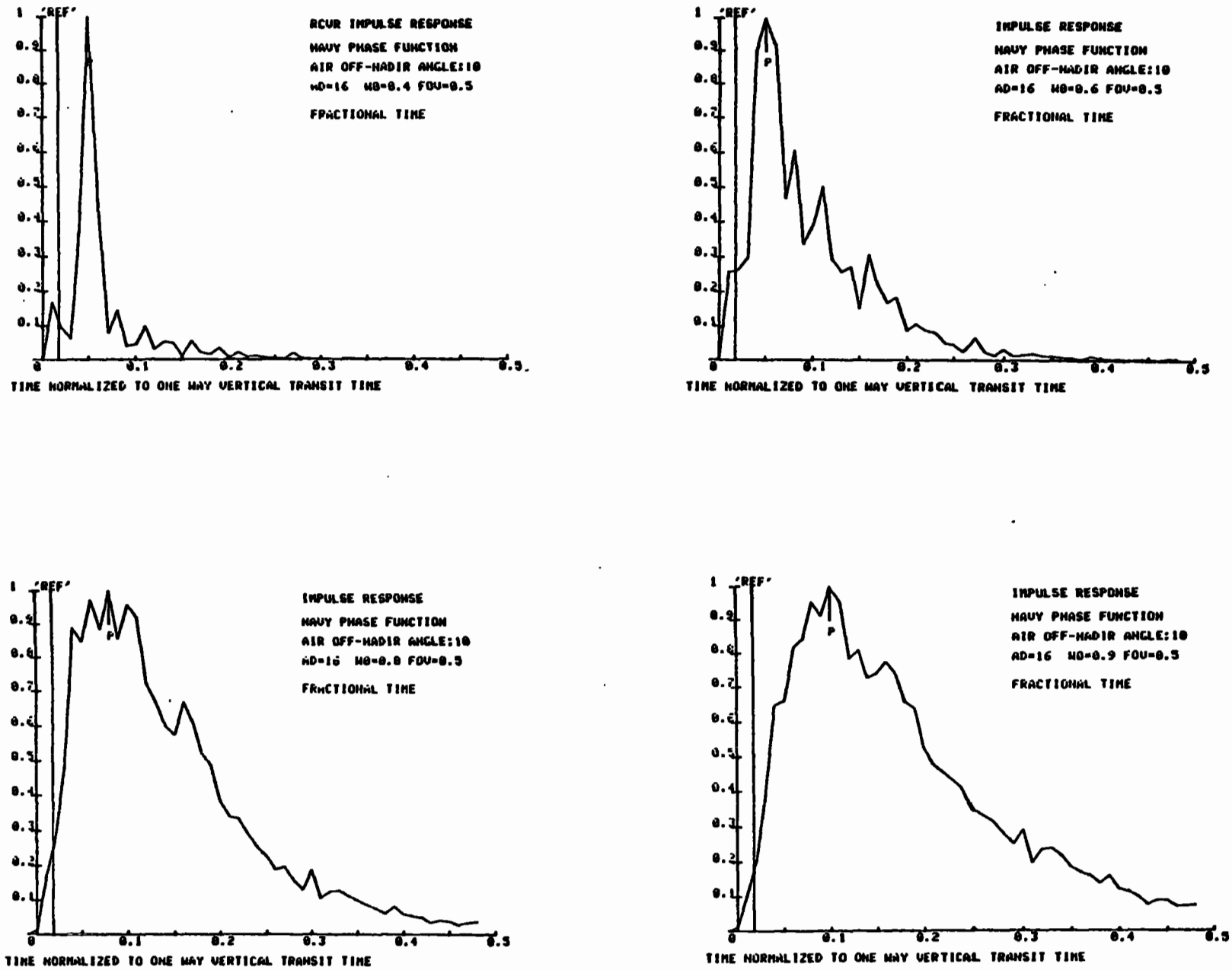

FIGURE 11. IMPULSE RESPONSE FUNCTIONS FOR VARYING ω_0

2.4 Actual Response Functions

For finite source pulses, the temporal response functions are calculated by convolving a selected source function with the appropriate impulse response functions. Realistic lidar receiver inputs or "environmental response functions" (ERFs) have been computed by digitally convolving the IRFs, scaled to depths of 5 m, 10 m, 20 m, and 40 m, with a 7-ns (FWHM) triangular source pulse which is representative of laser pulses from a state-of-the-art, high repetition rate, frequency-doubled Nd:YAG laser. Depth measurement biases for twelve different combinations of signal processing and pulse location algorithms have been calculated from these ERFs. The ERFs and their associated peak powers and biases are archived on magnetic media for future use.

Figures 12 and 13 present 20-m ERFs derived from the IRFs illustrated in Figs. 9 and 10. The simulation noise has been significantly smoothed by the convolution. For very narrow IRFs, the ERFs are similar to the source pulse; for broad IRFs, the ERFs are similar to the IRFs. Most cases of practical application lie between these limits, and the ERF shapes are a unique combination of both. For a source function significantly different from a 7-ns triangle, the ERFs and resulting biases would need to be recomputed by convolving the new source function with the depth-scaled, archived IRFs.

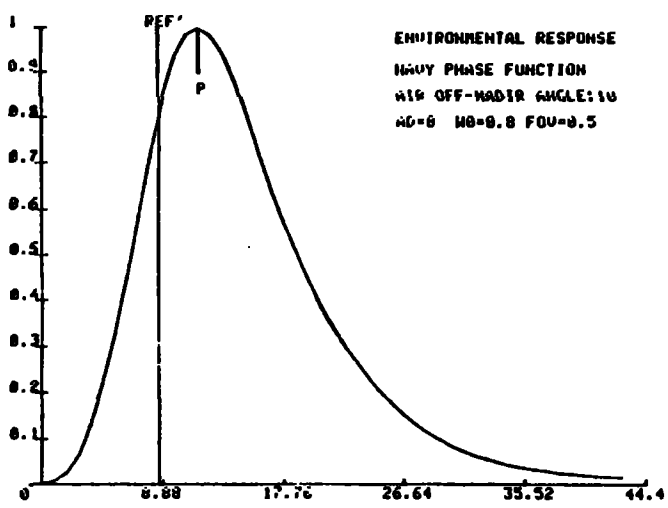

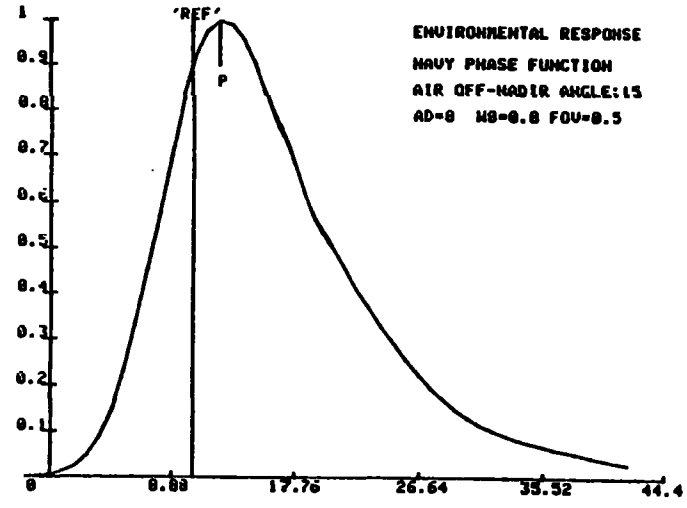

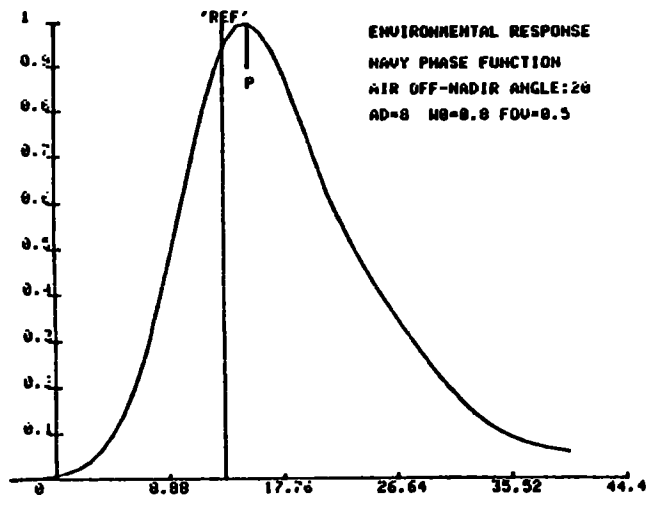

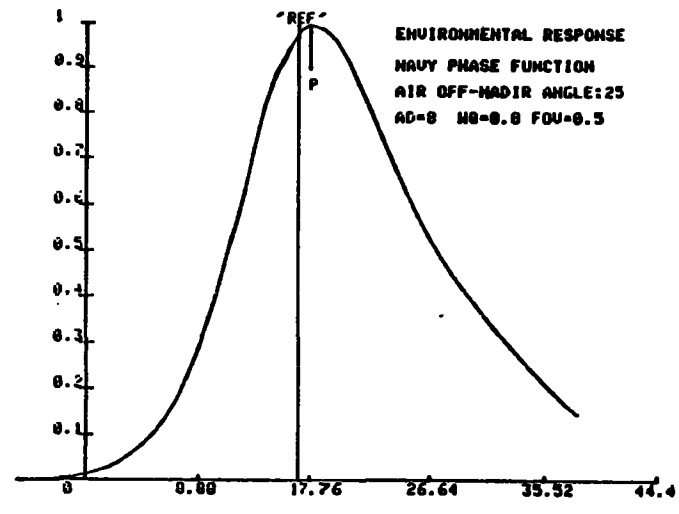

FIGURE 12. ENVIRONMENTAL RESPONSE FUNCTIONS FOR VARYING ANGLES

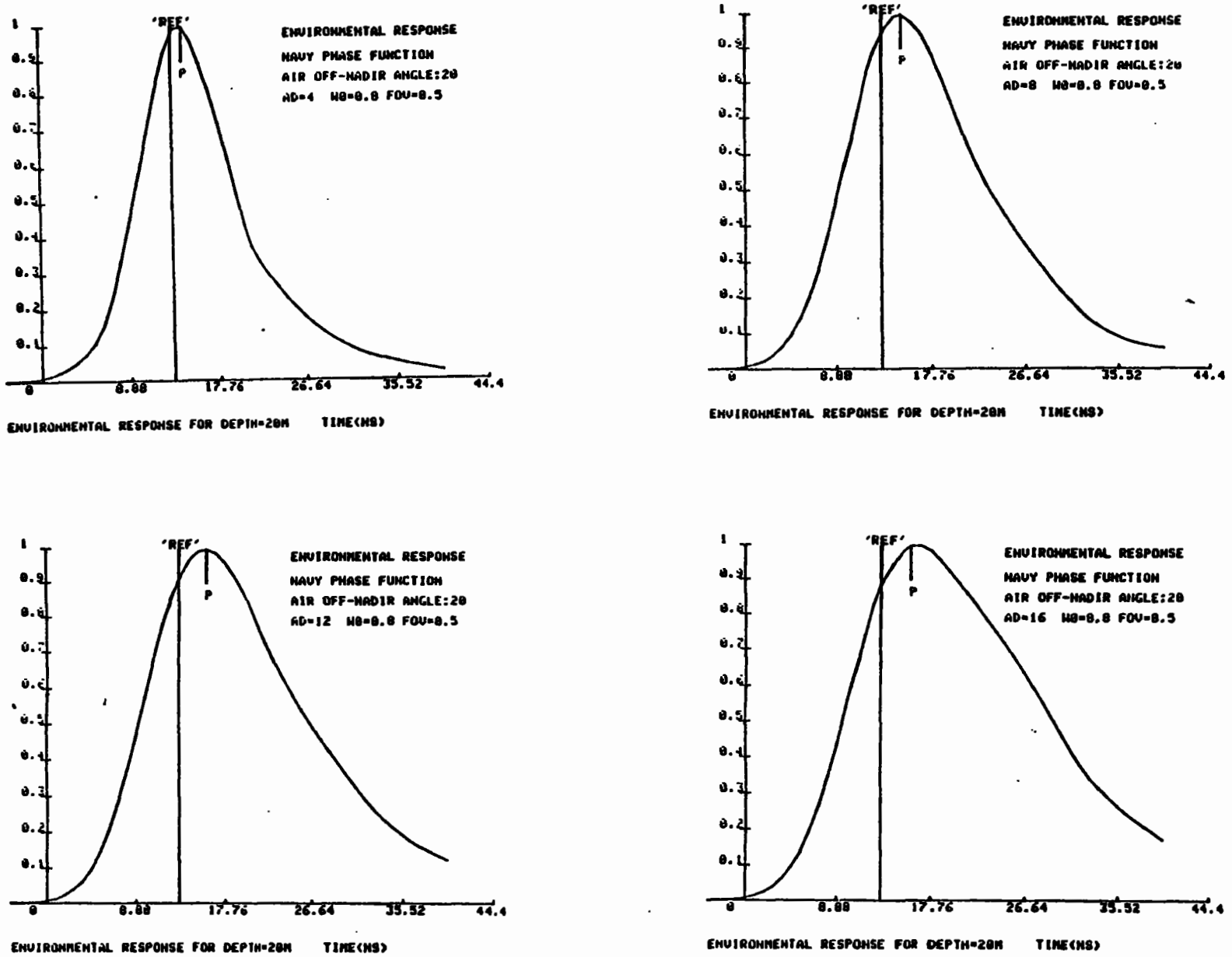

FIGURE 13. ENVIRONMENTAL RESPONSE FUNCTIONS FOR VARYING OPTICAL DEPTHS

3.0 SPATIAL RESULTS

3.1 Bottom Distribution

Scattering in the water column causes the incident beam to spread out spatially into an expanding cone. The extent of the spreading depends in a complex manner on the geometry, the optical depth, the phase function, and the single-scattering albedo of the water. For off-nadir angles, the energy density distribution is significantly skewed toward the vertical due to reduced attenuation, as seen in Fig. 14. This plot was generated by integrating the arriving energy at the bottom in a series of strips perpendicular to the direction of the aircraft. The skewness is more pronounced for higher optical depths, higher off-nadir angles, and more highly scattering phase functions such as "NOS". This early-arriving energy has a large effect on the shape of the impulse response function.

Quantitative relationships for the spatial extent of the beam have previously been developed by analytic approximation and physical measurements. Concise energy distributions for a variety of water types were measured in a laboratory tank by Duntley (1971). Unfortunately for our purposes, these results were based on a detector whose shape was a spherical "cap", all of which was at a constant distance from the laser source. The geometry of interest for laser hydrography is a tilted plane. A simple analytic expression based on small angle forward scattering approximations reported by Jerlov (1976) has the same drawback, in that it does not treat the increased optical depths for off-axis paths. Not surprisingly, therefore, his radial energy distribution predictions are in fair accordance with the Duntley measurements, although somewhat larger due to the simplistic assumptions.

Energy distributions for a planar detector (consistent with airborne laser hydrography geometry) have been estimated as an ancillary output of the Monte Carlo propagation simulation. Plots of 50% energy and 90% energy bottom distribution diameters, d_B, normalized to a vertical water depth, D, are shown in Fig. 15 (left axis) for nadir entry and several values of ω_0. The curves, which are averaged between NAVY and NOS phase functions, are labeled by the nth percentile energy fraction contained within. Curves for RMS diameters

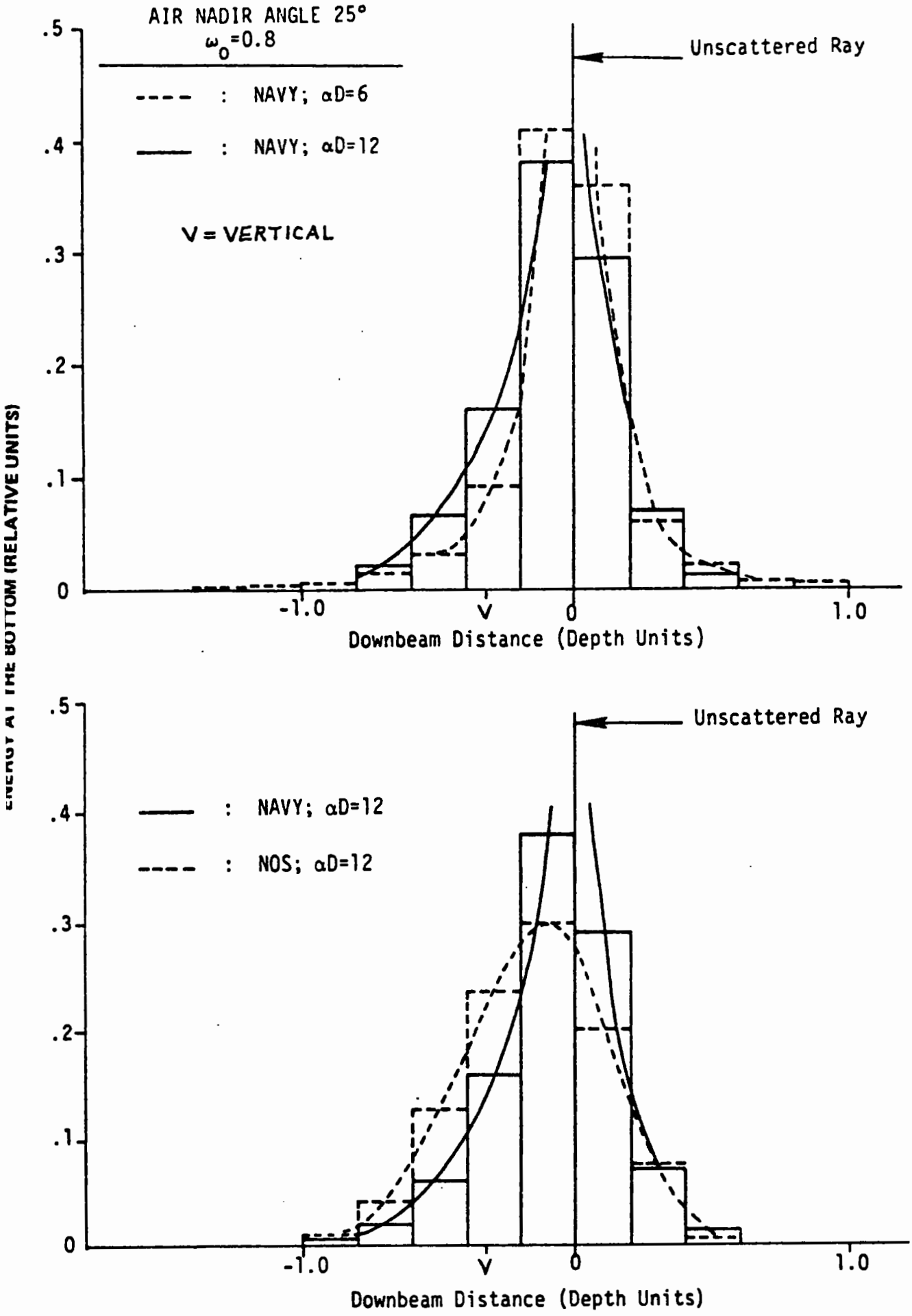

FIGURE 14. SPATIAL DISTRIBUTION OF PULSE ENERGY AT THE BOTTOM

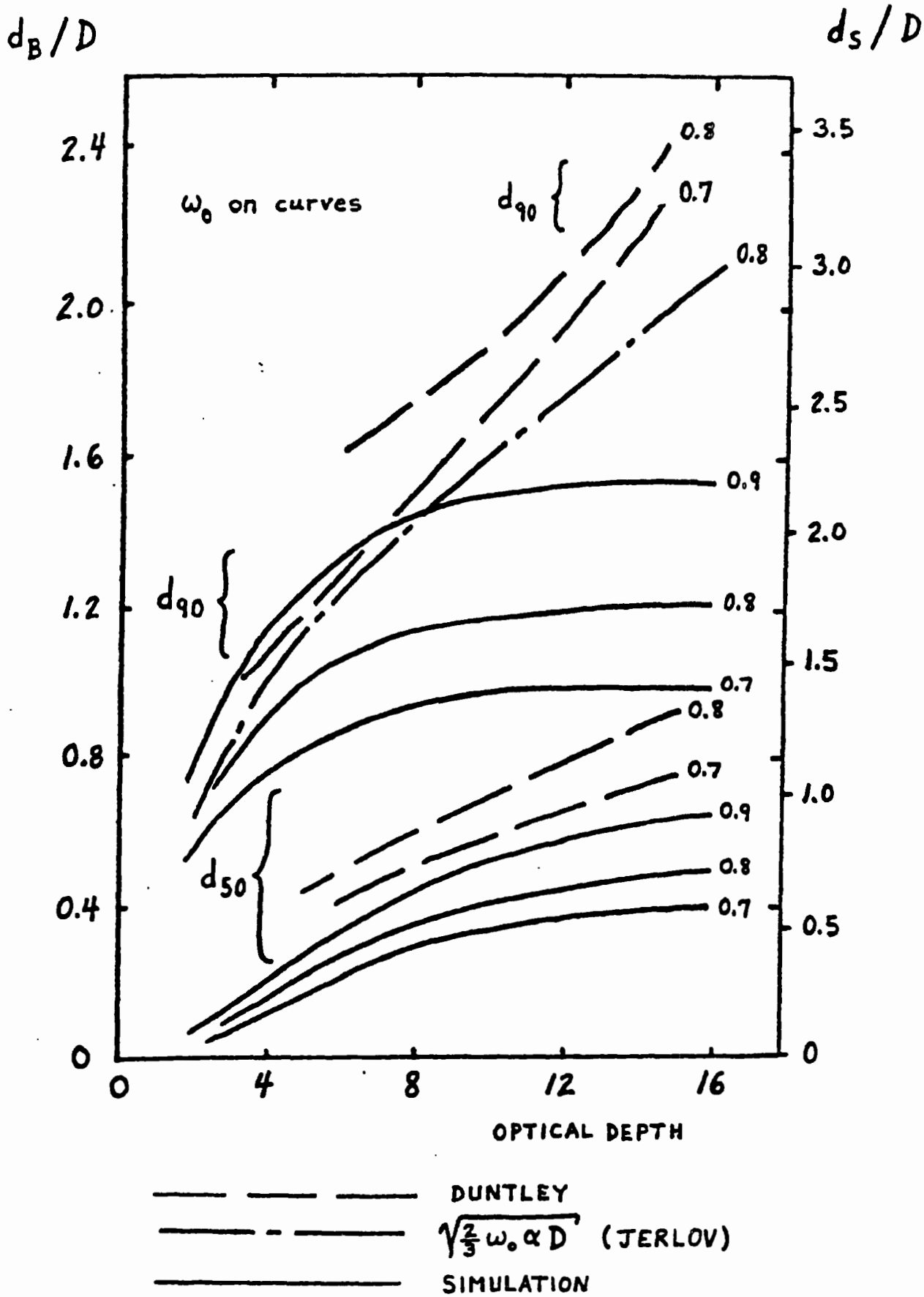

FIGURE 15. BOTTOM AND SURFACE DISTRIBUTION DIAMETERS FOR SELECTED ENERGY FRACTIONS

fall between the two values illustrated. The Duntley curves for 50% and 90% energy fractions are included for comparison. A curve derived from the Jerlov relationship, which yields an RMS diameter, is also included for $\omega_0 = 0.8$.

A fundamental and important functional difference is noted between the Duntley and Jerlov results to a spherical cap and the simulation results to a plane. The Duntley and Jerlov fractional diameters continue to rise with increasing optical depth, while the simulation results saturate. This behavioral difference is attributed to the disparate geometries. In the Duntley experiment, the off-axis radiation traversed the same path length as the on-axis radiation. For a planar target, the added attenuation length for non-axial paths will cause a significant reduction in the signal magnitude received at larger angles. This results in a reduction of the effective "spot" diameter -- particularly for large optical depths. This differential path length effect is much more pronounced for d_{90} than for d_{50} due to the larger net angles, and the Duntley d_{90} results consequently differ from the simulation by more than the d_{50} results. It can be seen that for the large optical depths, the simulation results indicate that the diameter of the 50% energy fraction at the bottom is roughly half the water depth, and the diameter of the 90% energy fraction is somewhat greater than the water depth. Mean and RMS diameters fall between these bounds.

3.2 Horizontal Resolution

Although one thinks of a laser beam as being a highly collimated probe, such is not the case in water. The beam is scattered by entrained particulates into an expanding cone whose size increases as the scattering optical depth of the medium increases. Based on the above results, the effective angular beam width at the bottom for a 50% energy fraction is about $2 \tan^{-1}(0.25) = 28°$. (Half the pulse energy is a suitable criterion for purposes of selecting the receiver field of view (FOV) to sustain penetration potential, as will be seen shortly.) This means that an airborne lidar will not provide detailed profilimetry with a horizontal resolution of several meters at typical operating depths in the 20 m - 40 m range. The soundings, rather, are center-weighted averages over an area with a diameter of roughly half the water depth. This fact is somewhat misleading, however, in that

small but not insubstantial shoal objects such as coral heads or large rocks will nevertheless reduce the measured depth because leading edge pulse location algorithms are sensitive to the early-arriving energy. If somewhat higher resolution were required for some special task, a narrower effective beam width could be obtained by limiting the receiver FOV. The tradeoff is a concomitant loss of peak return power and, hence, penetration capability. In optically shallow waters, this loss might be an acceptable compromise.

3.3 Upwelling Surface Distribution

The principle of reciprocity dictates that the upwelling, bottom reflected energy traverses a set of paths statistically similar to the downwelling paths. This means that the diameter of the surface distribution of reflected bottom energy can be derived from the convolution of the bottom energy density distribution with itself. The resulting surface diameter of upwelling bottom return energy will be somewhere between one and two times the equivalent bottom diameter, depending on the exact shape of the distribution. For a Gaussian distribution, the factor is $\sqrt{2}$. Surface diameters for this approximation are indicated on the right-hand axis of Fig. 15. For an estimated surface diameter, d_s, of the selected bottom-reflected energy fraction for nadir entry, the 50 % energy criterion is $d_s(50) \cong 0.7D$, and for a 90% criterion, $d_s(90)$ is over twice that.

3.4 Receiver Field of View

As seen in Fig. 15, the field-of-view (FOV) requirement depends strongly on which measure of spot "size" is used. The primary effect of the FOV is the determination of the bottom return signal-to-noise ratio (SNR) and, hence, the maximum useable depth or "penetration" capability. If the FOV is too small, the peak bottom return power and associated maximum penetration depth will be reduced. For nighttime operation, a larger than necessary FOV is benign, but in daylight, an excessive FOV will increase the solar noise level and, again, reduce penetration. The FOV "requirement" is thus the FOV which maximizes the SNR or, more simply, that which is just large enough not to significantly reduce the peak bottom return power.

It is important to recognize the distinction that for envisioned pulse location algorithms, the depth penetration potential, and hence receiver FOV, are dictated by the peak power of the bottom return, not the pulse energy. The relationship between these two measures is dependent on the width and shape of the environmental response function (ERF) or bottom return. These, in turn, are determined by the character of the source pulse and of the impulse response function (IRF) of the propagation. In other words, the exact receiver FOV requirement for a given set of circumstances is a function not only of the environment, but also of the source pulse width. In practice, however, it is sufficient to design the optical system to meet the spatial needs of the large optical depth case, as will now be demonstrated.

The receiver FOV requirement can be estimated by observing the behavior of the Monte Carlo spatial and temporal distributions. The Monte Carlo results of Fig. 15 are repeated with an added highlight in Fig. 16. For small physical and optical depths, say two to four, the IRF is short, and the ERF approximates the source pulse. Any loss of energy results directly in a loss of peak power because the ERF cannot become narrower than the source pulse. For this case, therefore, the d_s/D required would derive roughly from the d_{90} curves. For large physical and optical depths, the ERF takes the character of the IRF and is significantly wider than the source pulse. Moderately restricting the FOV will reduce the pulse energy, but not the peak power, by truncating the tail of the IRF, as seen in Fig. 17. This is a beneficial feature because, in deep water where the FOV requirement is the greatest, the pulse stretching is also greatest. A modest fraction of the pulse energy from the trailing edge can be discarded without a significant drop in the peak pulse power -- thus reducing the necessary energy fraction and the actual FOV requirement. By examining the effect of reduced FOV on such IRF shapes, it has been noted that the peak height is not significantly reduced until d_s/D becomes less than about 0.7, which , from Fig. 16 corresponds roughly to a 50% energy fraction.

The heavy band drawn across Fig. 16 is an estimate of the overall d_s/D requirement according to these arguments. The function rises only slightly toward small optical depths because, even though the required energy fraction is larger, the relative expansion of the beam due to scattering is less. For

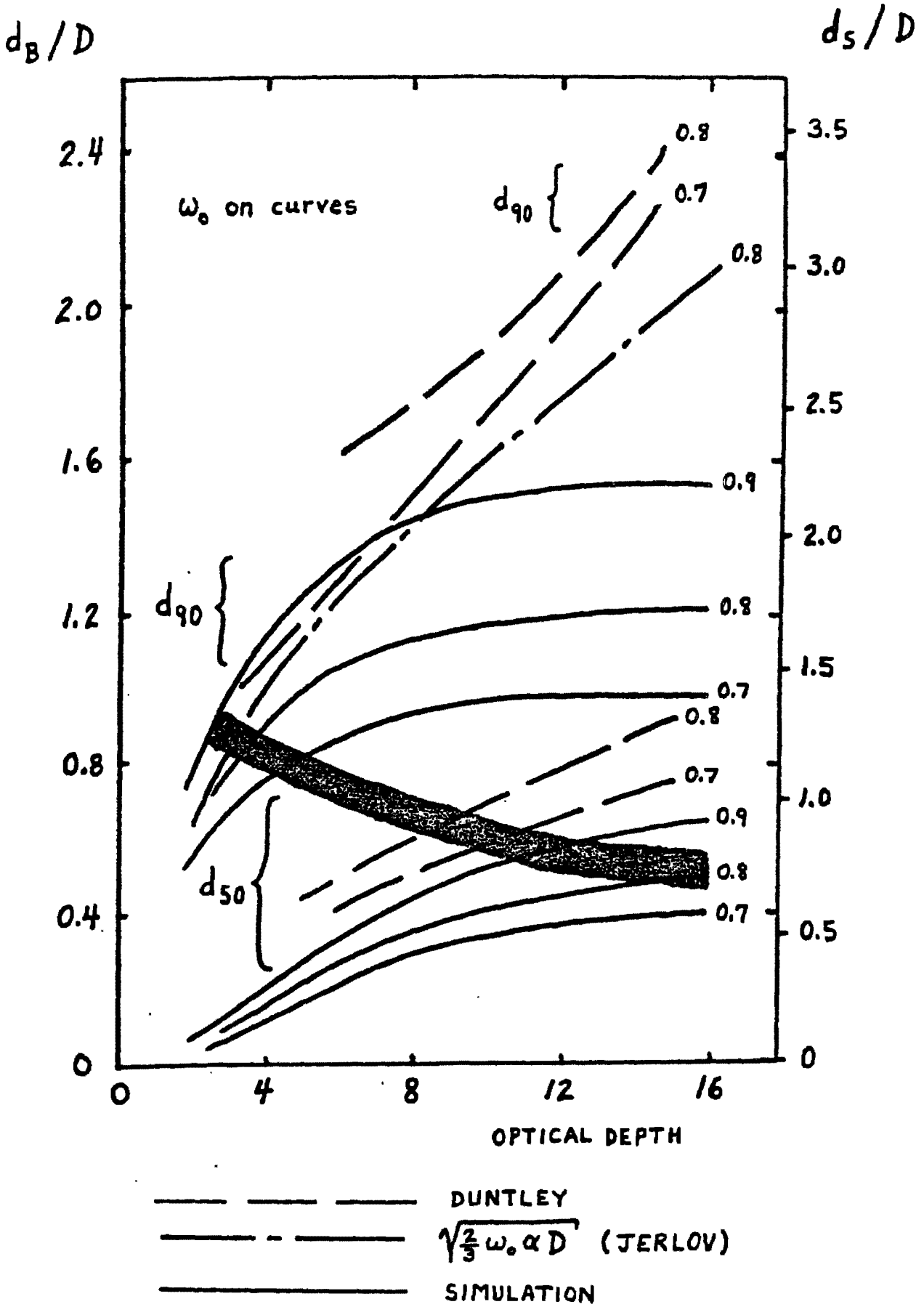

FIGURE 16. RECEIVER FIELD OF VIEW REQUIREMENT

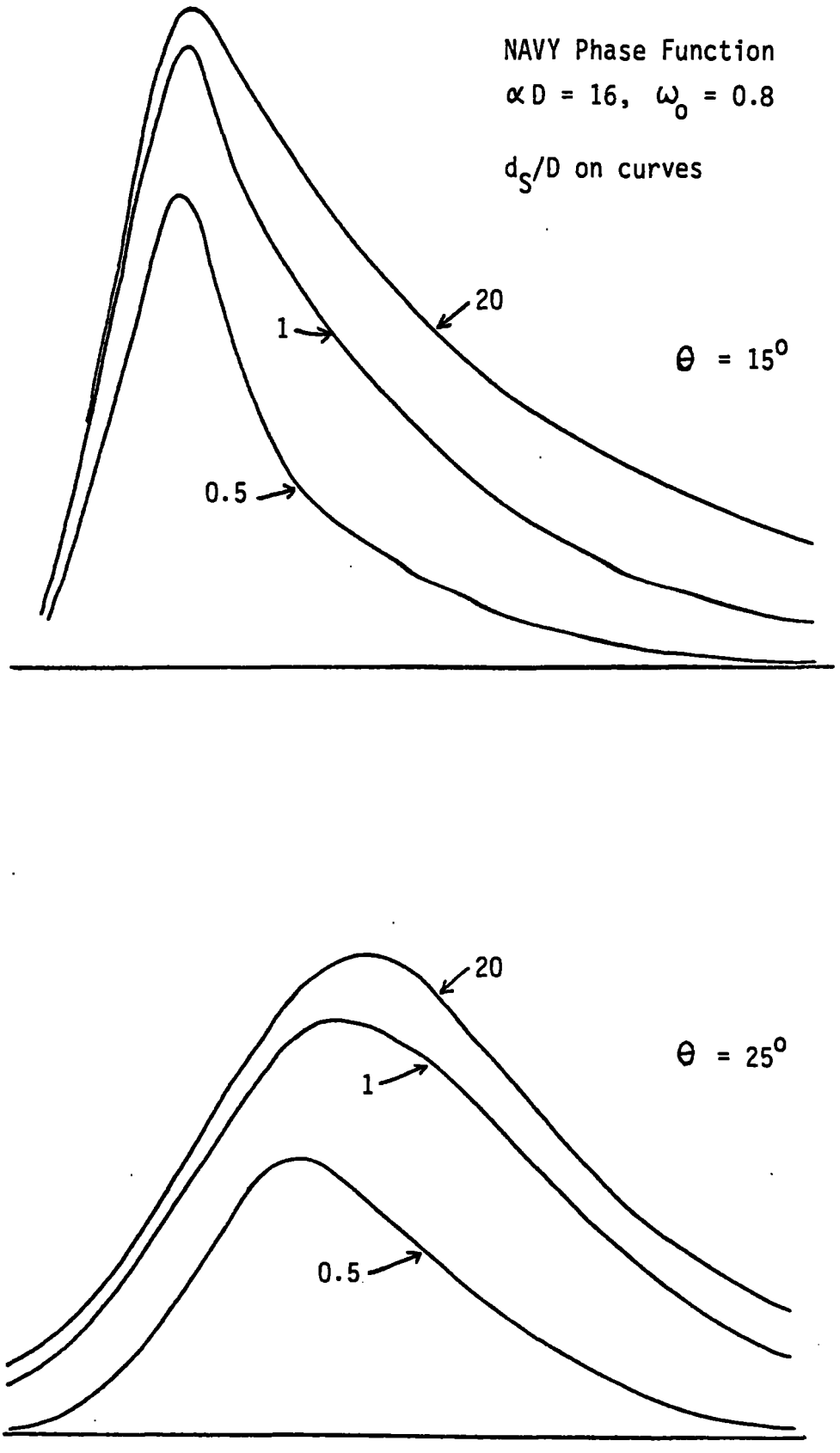

Figure 17. Field of View Effect on High Optical Depth IRFs

a practical system, the receiver FOV can be safely set to the high αD value where d_s/D is smallest, since at smaller optical depths a slight loss of power will not significantly affect performance. The best estimate for a practical FOV requirement is thus a surface spot diameter for the receiver of about 0.7D which corresponds roughly to a 50% energy criterion at large optical depths, as previously noted. For an aircraft altitude, H, the necessary full angle FOV would be $\psi_{FOV} \cong d_s/H \cong 0.7D/H$. The FOV desired for a typical aircraft altitude of 300 m and a depth of 35 m would thus be about 80 mr. A FOV of this size is fairly large for a compact optical system, but nevertheless achievable.

This result is relatively independent of nadir angle. For off-nadir angles, the irradiated bottom dimension is larger roughly by $\sec\phi$ due to the additional slant distance to the bottom, but the FOV needed to encompass the resulting surface spot is smaller by $\cos\theta$ (where the angles are as defined in Fig. 1). For the relatively small angles of interest, these functions effectively cancel.

The effect of FOV on propagation-induced biases will be seen in section 5 to be small. The reason for this is the fact that significant biases would exist even for zero FOV (ignoring, for a moment, the corresponding lack of signal strength), because the leading edges of the IRFs are not greatly affected by FOV. The concept that the IRF has a certain minimum width for zero FOV stems from the fact that photons emerging from the medium at the point of entry may have undergone substantial multiple scattering and consequential pulse stretching on their round trip to the bottom and back. Reciprocity in this case requires that the photons must effectively retrace their downward paths to exit the medium at their entry points in the exact opposite direction. In this special case, the convolution of the downwelling distribution with a cosine-modified version of itself degenerates into a simple product with the times doubled for the round trip. This concept has been used to estimate the zero-FOV IRFs from the downwelling temporal distributions. An example is seen in Fig. 18 plotted along with the infinite-FOV IRF. It is clear that for a leading edge detector, the biases (the detection time compared to the reference time) may be reduced only slightly if at all.

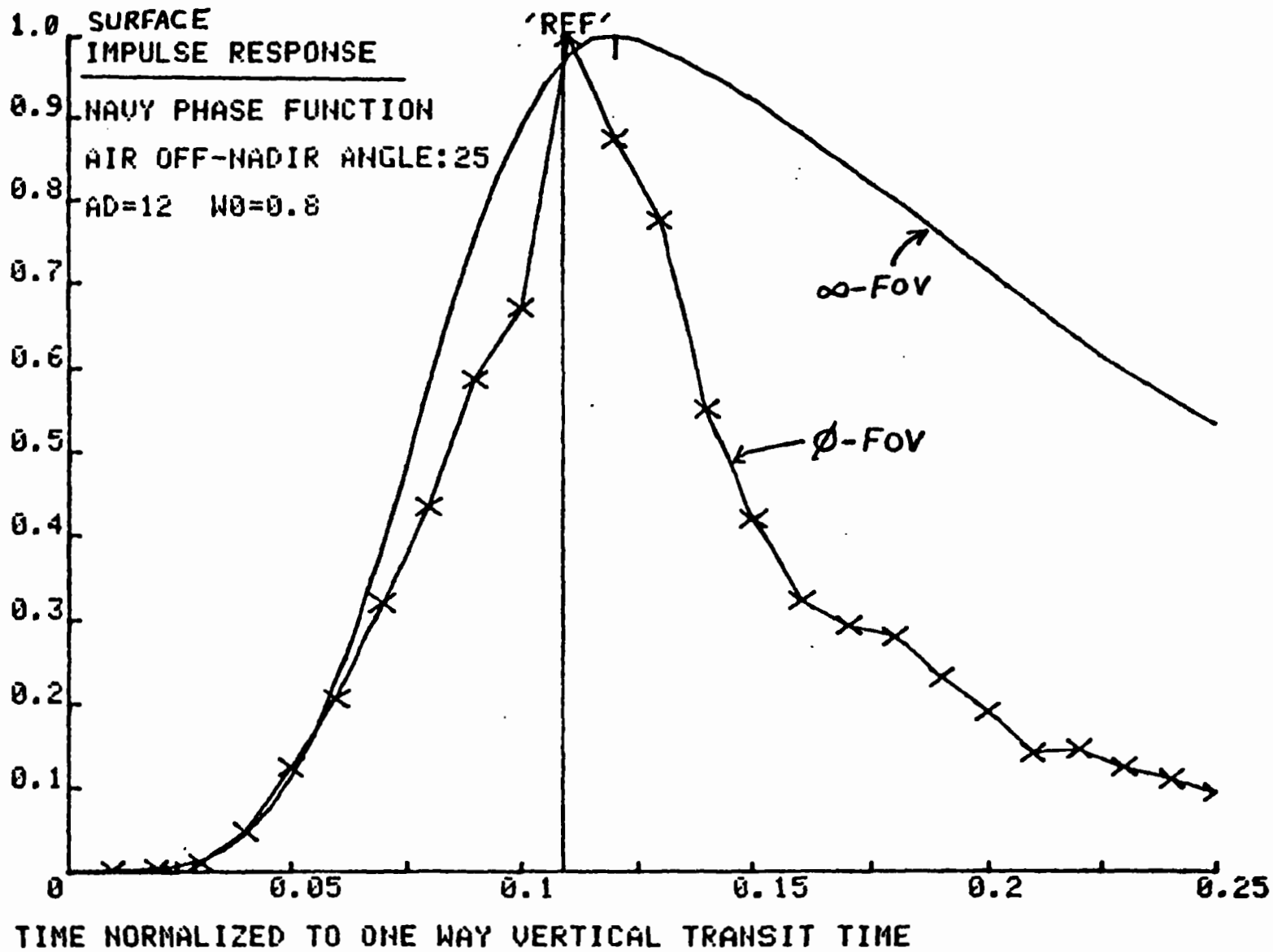

FIGURE 18. ZERO FIELD-OF-VIEW RESPONSE FUNCTION

4.0 ENERGY AND PEAK POWER RELATIONSHIPS

4.1 Introduction

The economic viability of an airborne laser hydrography system depends on the existence of large areas of relatively shallow water from which satisfactory bottom returns can be detected. The basis for determining the performance of a communications system is the received signal (energy or power) equation. The level at which this signal becomes unacceptably noise contaminated determines the maximum range. In the case of airborne lidar bathymetry, a pulsed laser transmitter is communicating with a colocated receiver via a complicated channel which consists of two passes through the atmosphere, two passes through the undulating air/water interface, two passes through a highly scattering and absorbing water column of variable clarity, and a bounce off a poorly reflecting bottom. The shape, duration, and magnitude of laser hydrography bottom returns depend in a complex way on the source pulse, the beam nadir angle, the depth of the water, the optical properties of the water, and the bottom topography.

Over the years, the return power equation has appeared in a wide variety of forms, because the propagation in the water has not been well understood, and some complex effects can only be approximated. Refinements and improvements continue to be made as new data become available. In this section, several factors will be added or altered to account for the effects of propagation-induced pulse stretching. In order to predict penetration limitations for an operational system, energy distributions and impulse response functions parameterized on the aforementioned variables for a flat bottom have been calculated from the Monte Carlo simulation results. Simulated bottom returns (environmental response functions) have been determined by convolving the impulse response functions with a 7-ns FWHM triangular source pulse. Bottom return energy and peak power relationships derived from these results are reported in this section.

4.2 Signal Energy

In its basic form, the so-called "radar" equation for the airborne laser hydrography bottom return energy can be written as

$$E_R = E_T \eta R \frac{\Omega_R}{\Omega_B} F e^{-2kP} , \quad (1)$$

where: E_R is the received pulse energy,

E_T is the transmitted pulse energy,

η is the total optical system loss factor,

R is the bottom reflectivity,

Ω_R is the solid angle subtended by the receiver,

Ω_B is the effective solid angle of the bottom-reflected energy above the air/water interface,

F is a loss factor to account for insufficient receiver FOV,

k is an attenuation coefficient which depends on water clarity, and

P is the effective slant path length in water to the bottom.

Losses in the atmosphere due to absorption and scattering are small (ten to twenty percent) for altitudes of interest in clear air and have been omitted for the sake of simplicity. The two percent losses through the air/water interface have also been neglected. Individual factors in this equation will now be discussed in detail, beginning with the exponential term.

4.2.1 Nadir Entry

The most elementary output from the simulation is the fractional number of incident photons reaching the bottom, i.e., the spatially and temporally integrated energy arriving at the bottom. Those photons not reaching the bottom are lost to either scattering or absorption. If one plots the log of the downwelling energy for nadir entry versus vertical optical depth, αD, for a unit energy impulse, as seen in Fig. 19, the results for both phase functions are families of nearly straight lines with slopes dependent on the single-scattering albedo, ω_0. The regions of joint high αD and low ω_0 are dashed because of larger statistical variances in the results for the extremely weak returns from these high attenuation circumstances. The variances could have been reduced by running the simulation longer, but it was not deemed necessary because such small values of ω_0 are not expected to be found in coastal waters.

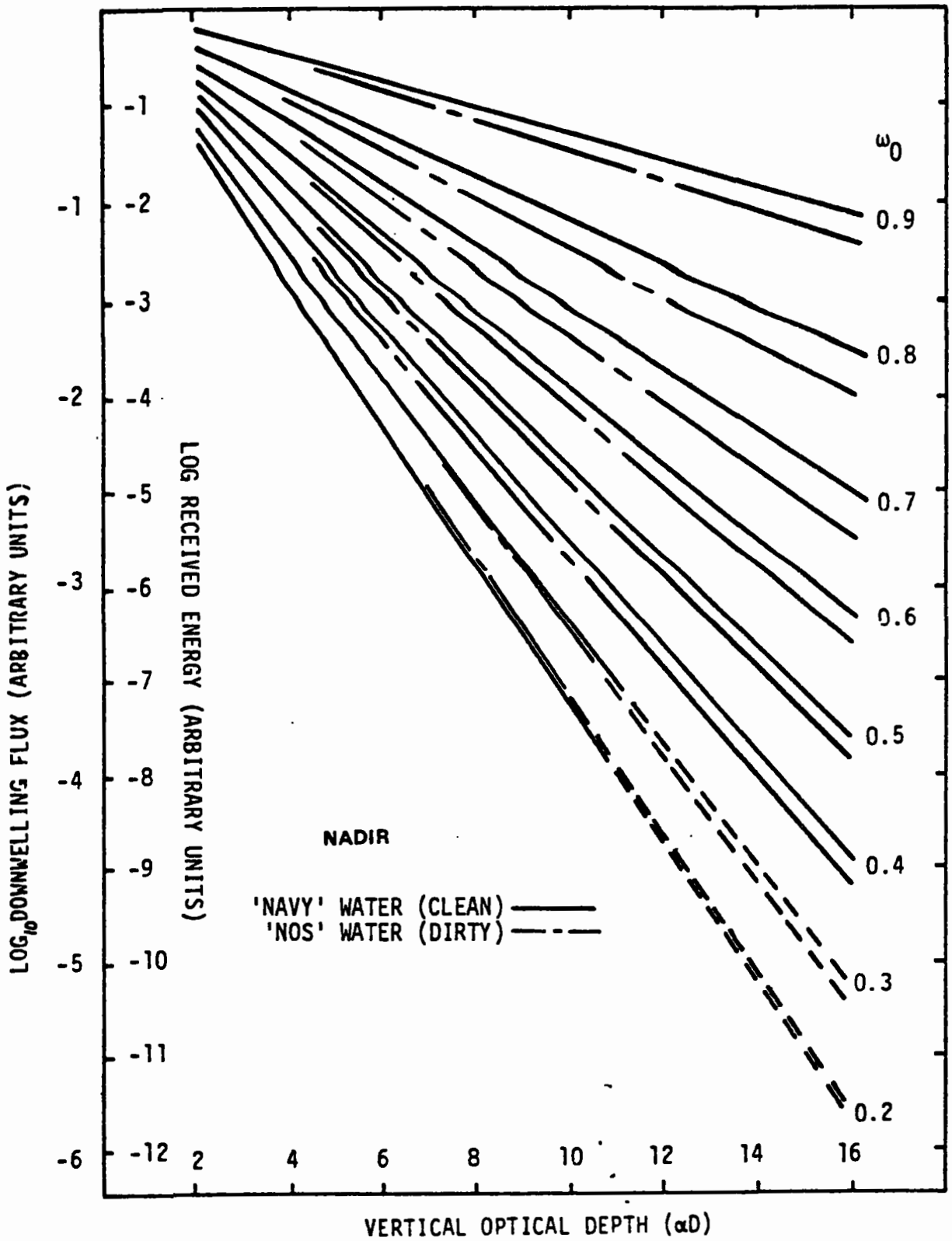

FIGURE 19. DOWNWELLING ENERGY AND RECEIVED ENERGY

Integrating over depth the defining relationship for the diffuse attenuation coefficient, K, for nadir entry into homogeneous water leads to an expression for downwelling energy, E_B, of the form $E_B \propto \exp(-KD)$, where D is the depth. If the asymptotic slopes of the Fig. 19 downwelling energy curves are denoted as $\gamma(\omega_0,\Psi)$, where $\Psi \equiv P(\psi)$ represents the phase function, then for nadir beam entry, $E_B \propto \exp[-\gamma(\omega_0,\Psi)\alpha D]$. It is clear from these equations that the slopes are thus $\gamma(\omega_0,\Psi) = \frac{K}{\alpha}(\omega_0,\Psi)$. The slopes of the simulation results in Fig. 19 actually increase slightly with increasing optical depth, as K itself increases slightly with depth in homogeneous water. This is because K is not an inherent water property and, at shallow optical depths, increases due to a scattering-induced increase in average path length to a given vertical depth. This effect is further demonstrated in Fig. 20, a plot of simulation results for the mean secant of photon arrival angles as a function of optical depth. The largest portion of the increase occurs at relatively small optical depths, and the log energy curves are thus nearly straight at higher optical depths. In this report, the symbol, "K", will be used exclusively for the medium-to-high optical depth or "asymptotic" value of the diffuse attenuation coefficient.

The log energy curves can be seen to extrapolate back to a value slightly above the origin (at zero optical depth) which represents a linear factor of roughly 1.5. Because the curves extrapolate near to the origin, the average slope and the instantaneous slope are nearly equal at all αD, and K/α is thus nearly independent of αD as seen detailed in Fig. 21. This permits a universal plot of K/α versus ω_0 for the two phase functions as seen in Fig. 22. The phase function effect is seen to be relatively small.

This K/α relationship is an extremely important functionality because it clearly demonstrates that the ratio of the two most commonly measured attenuation coefficients is determined solely by a third parameter, the sometimes ignored single-scattering albedo. The relationship is also important because it provides the best opportunity for validation of the simulation outputs, as noted in section 2.2.5. Timofeyeva and Gorobets (1967) derived $K/\alpha(\omega_0)$ experimentally for a number of scattering media. The Timofeyeva curve plotted on Fig. 22 is for milk which was claimed to have scattering properties similar to those of seawater. The simulation results

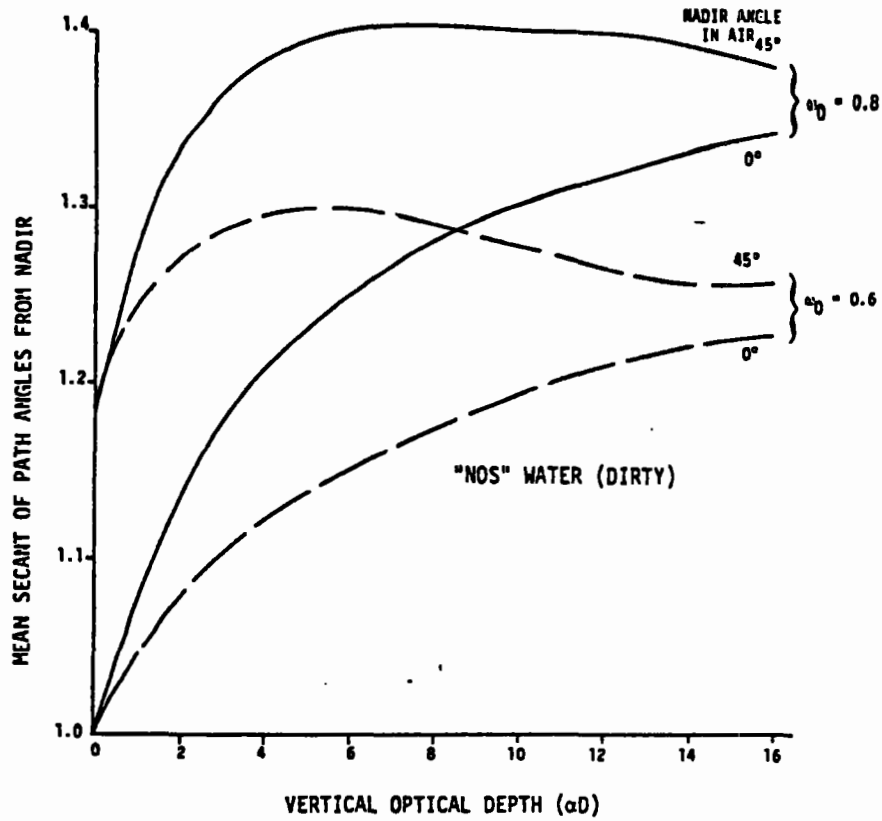

FIGURE 20. MEAN SECANT OF ARRIVAL ANGLES FROM NADIR

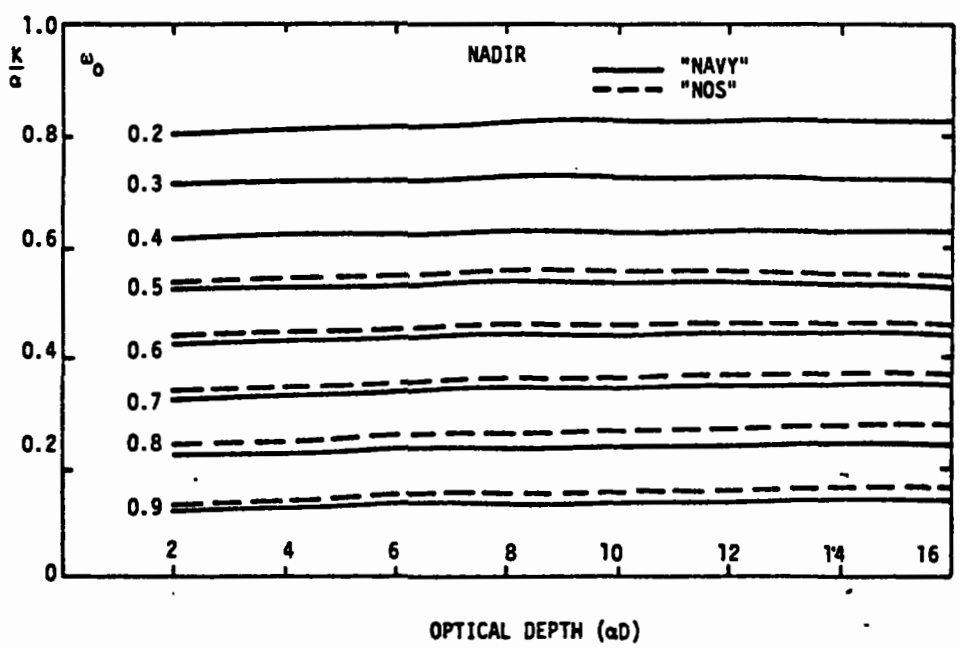

FIGURE 21. AVERAGE K/α RATIOS

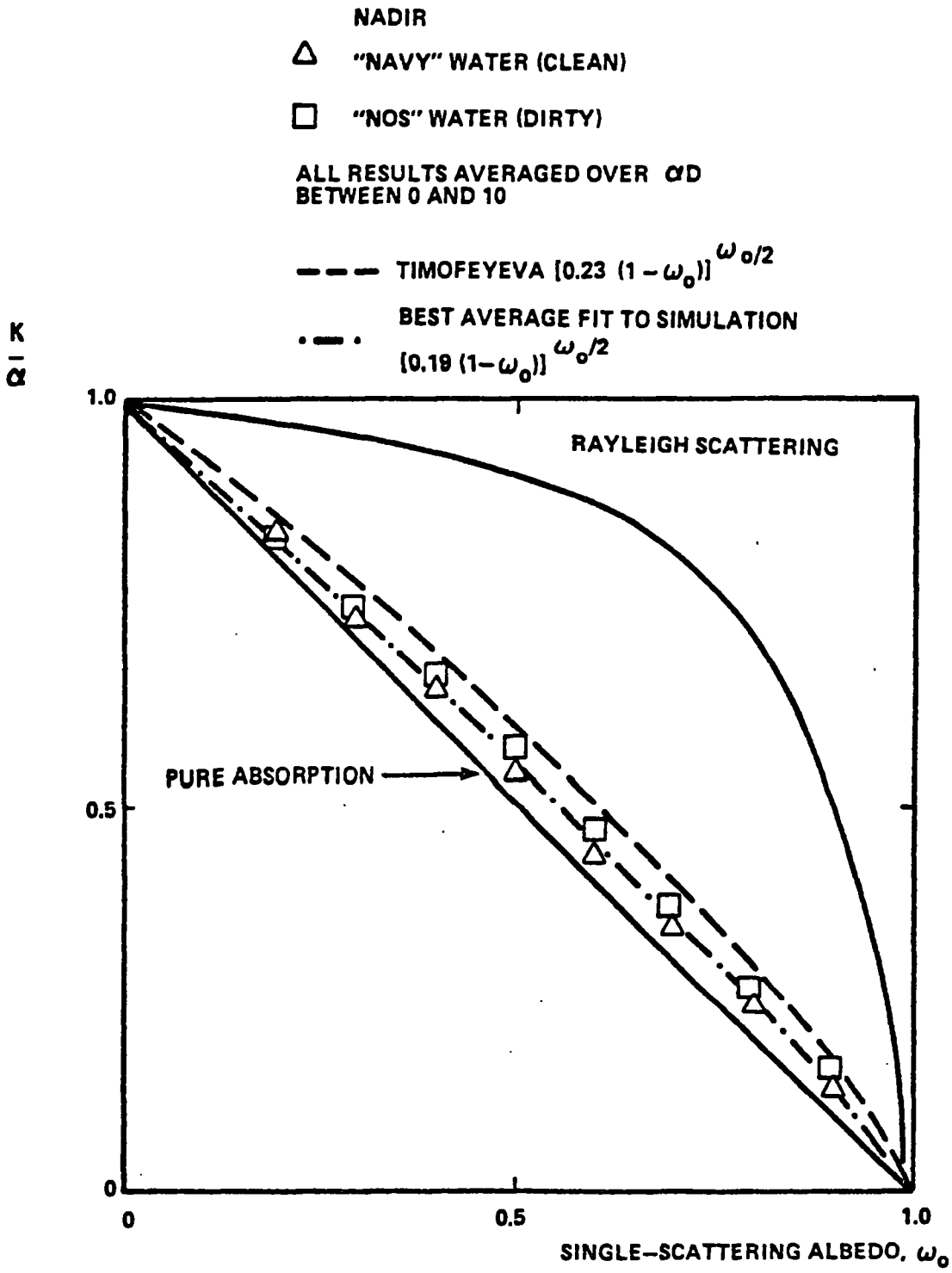

FIGURE 22. SIMULATION RESULTS FOR K/α VS ω_0

are seen to be in good quantitative agreement and demonstrate the correct trend with phase function, assuming that milk has a slightly more widely scattering or "dirtier" phase function than "NOS" water. These curves are also in good agreement with the theoretical results of Prieur and Morel (1971) for "typical oceanic water".

The bottom reflected pulse energy, E_R, returned to a distant, airborne receiver was calculated by temporally integrating the round-trip impulse response functions derived from the simulation for an assumed Lambertian bottom reflection. For a large receiver FOV, the plots of E_R versus αD, as indicated on the "inside" axis of Fig. 19, are virtually identical to the E_B versus αD plots with D replaced by 2D to account for the round-trip distance. The received pulse energy can thus be represented as $E_R \propto E_B{}^2 \propto \exp(-2KD)$.

It is interesting to note that this relationship implies that the effective attenuation coefficient is K in both upwelling and downwelling directions, even though the incident downwelling beam is highly collimated, while the bottom reflection was assumed to be diffuse. The reason is that the only photons of interest are those which leave the water in the exact opposite direction from which they entered, in order to reach the distant colocated receiver. The scattering of photons in the water is independent of direction, and the paths are, in effect, reversible. Reciprocity states that the ensemble of allowed scattering paths through the water for upwelling radiation is thus identical to that for downwelling radiation. The utilization of the downwelling paths by upwelling radiation is determined by the bottom reflection weighting function. The result $E_R \propto \exp(-2KD)$ is indicative of the fact that the Lambertian weighting function for the bottom reflected upwelling distribution is similar to the downwelling arrival angular distribution.

It is clear from Fig. 19 and from the above equation that for nadir entry the large FOV "system" attenuation coefficient for received energy is K, the diffuse attenuation coefficient of the water. This familiar expression has often been used in signal equations for describing the return "strength" for airborne lidar systems. We shall now see how this must be modified to take off-nadir operation into consideration.

4.2.2 Off-Nadir Entry

The effect of off-nadir beam entry angles (θ in air refracted to ϕ in the water) is complex and depends on the depth and water optical properties. At low optical depths, an off-nadir input beam undergoes little scattering, and the loss per unit vertical optical depth is greater than at nadir due simply to the geometrical increase in the physical path length by a factor of $\sec\phi$. As the optical depth increases, scattering causes the beam to spread into a cone of increasing angle about the mean path. Photons on longer paths diverted from the central "core" tend to be eventually absorbed, while those on shorter paths in the "undercutting" region undergo less average absorption which increases their chances of survival.

The center of the core thus curves toward the vertical with increasing optical depth because that is the shortest distance and least lossy path. (This effect is seen underwater by scuba divers who note that, regardless of the time of day, the sunlight always appears to come from directly overhead in all but the shallowest water.) The effect is also seen in Fig. 20 where the mean secant for off-nadir entry begins at $\sec\phi$ but, at high optical depth, saturates at a value equivalent to that for nadir entry. For small entry angles, the core axis can become (nearly) vertical at moderate optical depths, while for large entry angles, very large optical depths are required. As seen in Fig. 20, the center of the core tends toward the vertical more quickly for small ω_0 due to greater absorption of the longer paths. The net result is that the effective distance to the bottom for off-nadir entry lies between $D\sec\phi$ and D and can be described as $D\sec\phi_{eff}$, where $\phi_{eff}(\theta,\alpha D,\omega_0,\Psi)$ is the "effective" water nadir angle which, as noted, depends on the entry nadir angle, the vertical optical depth, the single-scattering albedo, and the phase function.

The effect of off-nadir beam entry angles on the bottom energy and on the energy returned to a distant, large field-of-view receiver is seen in Fig. 23 for the NOS phase function. The curves for a very large 45° incident nadir angle are seen to be nearly straight and exhibit slightly higher slopes than for nadir entry but lower slopes than would be expected for the unscattered ray. They can thus be represented as $E_R \propto \exp(-2KD\sec\phi_{eff})$. From Fig. 23, at

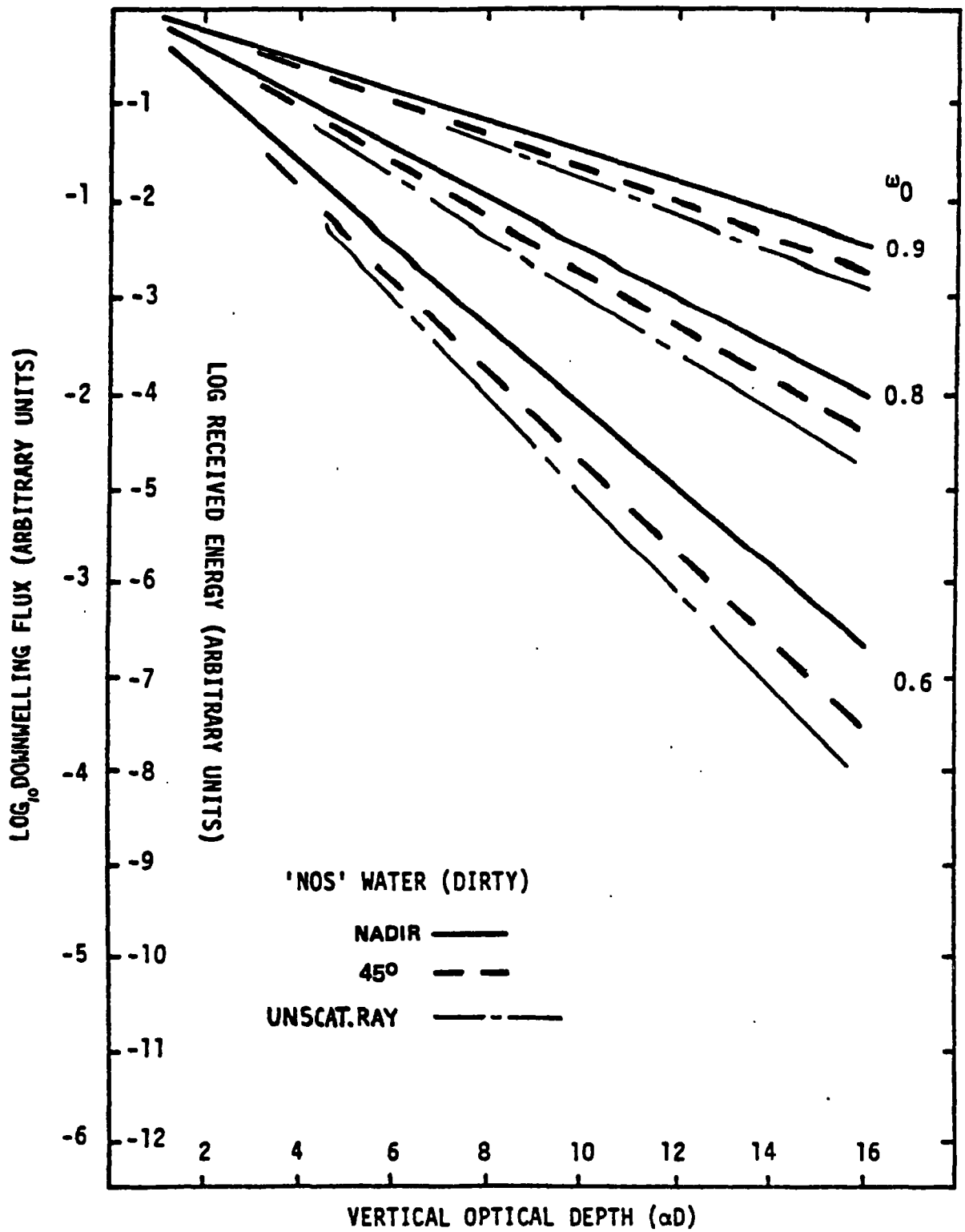

FIGURE 23. NADIR ANGLE EFFECT ON ENERGY

$\omega_0 = 0.8$, for example, it can be calculated that $\sec\phi_{eff} = 1.10$ ($\phi_{eff} = 24.8°$). For smaller incident nadir angles typical of airborne laser hydrography operations (θ=15°-25°), the value of $\sec\phi_{eff}$ approaches 1.0 for all but the shallowest of optical depths. (The secant of 10°, for example, is 1.015.) For practical cases, the pulse energy returned to a distant airborne receiver can thus be expressed simply as $E_R \cong \exp(-2KD)$, independent of incident nadir angle.

Scattering spreads the beam out spatially to a great extent and dictates a not insubstantial receiver field-of-view requirement in order to maintain the F factor near unity, as seen in section 3.4. An insufficient FOV which spatially excludes a portion of the returning energy reduces F below unity in a highly complex way which depends on the FOV, aircraft altitude, nadir angle, water optical parameters, and depth. This effect could alternately be viewed as an increase in the effective system attenuation coefficient (Gordon 1982) dependent on the same variables.

The solid angle subtended by the airborne receiver from a nadir angle, θ, and an altitude, H, is $\Omega'_R = A_R\cos^2\theta / H^2$. For an assumed Lambertian bottom reflection, the effective solid angle in the water is $\Omega_w = \pi$. Upon refraction through the air/water interface this angle increases by a factor n_w^2, where n_w is the index of refraction of water, so that $\Omega'_B = n_w^2\ \Omega_w = n_w^2\pi$. In the limiting case of high altitude and shallow water depth, the solid angle ratio would then be $\Omega'_R/\Omega'_B = A_R \cos^2\theta / \pi\ n_w^2\ H^2$. For the general case where the water depth is not necessarily much smaller than the altitude, it has been shown (Levis et al. 1974) that the exact expression can be written as $\Omega_R/\Omega_B = A_R/\pi(n_w\ H \sec\theta + D \sec\phi)^2$. This can be approximated by the simpler expression $\Omega_R/\Omega_B \cong A_R\cos^2\theta / \pi\ (n_w\ H + D)^2$, which gives virtually the same results for typical parameter values. For practical nadir angles, depths, and water clarity, the received energy equation thus takes the form

$$E_R \cong \frac{E_T\ \eta\ R\ F\ A_R\ \cos^2\theta}{\pi\ (n_w\ H + D)^2}\ e^{-2KD}\ . \qquad (2)$$

Energy-based pulse location algorithms such as correlators or centroids are not appropriate for precisely timing underwater light propagation because pulse stretching strongly affects the shape and duration of the pulses.

Typical leading-edge power detectors such as a fractional threshold are also affected by pulse stretching, but to a much lesser degree. A not insignificant fraction of the return energy is not "useful" because it occurs in the elongated tail of the return pulse. It is important, therefore, to investigate the effect of pulse stretching on the peak power of the return pulses as a function of depth and water optical properties.

4.3 Signal Power

Since pulse detections are based on the instantaneous pulse power, not the integrated pulse energy, the received energy equation must be converted to one which describes the peak pulse power. It is clear that peak power and pulse energy are proportional, i.e., obey the same functionalities, as long as the pulse shape remains unchanged. Pulse stretching removes that proportionality. Although the pulse may contain the same total energy, the fact that it is distributed over a longer time interval causes its peak power to be reduced. Furthermore, for a fixed αD, the absolute amount of stretching, i.e., the actual pulse length, is, from simple geometry, linearly proportional to the physical depth, D. For this reason, underwater propagation causes not only a loss of energy as a function of optical depth, but the associated pulse stretching causes a further loss of peak power with respect to the pulse energy, which varies both as a function of the physical depth and the inherent optical parameters.

For a finite transmitted source pulse, the return pulse at the receiver is the convolution of the source pulse with the impulse response function (IRF) of the target geometry. The result of this convolution, which has been termed the environmental response function (ERF), is the theoretical input to the airborne receiver. The energy equation is the bounding case for little relative pulse stretching, where the ERF is nearly identical to the source pulse. For small optical depths where pulse stretching is minimal, the impulse response will be very short compared to practical source pulses of interest in the 5-10 ns FWHM range. For this case, and for the case of very long source pulses, the ERF is nearly identical to the incident source pulse, and the return energy equation could be used as a power equation with E's replaced by P's. For the other bounding case of large optical and physical

depths, the IRF can become significantly longer than the source pulse, and the ERF will be similar to the IRF. A new power equation can be developed for this case, as will now be seen. The general result for practical source pulses, which falls between these extreme bounds, will be described thereafter.

4.3.1 Impulse Response Results

Relative IRF peak power plots for the two phase functions at nadir entry are illustrated in Fig. 24 for constant physical depth. Several features are apparent if one compares these results with Fig. 19. First, the phase function effect is somewhat larger than for energy. Second, for high ω_0, these semi-log plots tend to curve upwards at high αD; their slopes are initially steeper than for the corresponding received pulse energy curves, but at high αD the corresponding slopes become more nearly equal. For low ω_0, the plots are nearly straight and only slightly steeper than the corresponding energy curves. This behavior can be understood by examining the following model.

Because most of the semi-log plots of IRF peak power versus optical depth for constant physical depth are relatively straight, one can again choose to describe the behavior as exponential and define an average system attenuation coefficient, $k_p(\alpha D)$ for received power, P_R, at an optical depth αD from the slopes as follows:

$$P_R\big|_{D=\text{const}} \quad e^{-2k_p' \alpha D} = e^{-2 \frac{k_p}{\alpha} \alpha D} = e^{-2 \frac{k_p}{K} \frac{K}{\alpha} \alpha D} = e^{-2 \frac{k_p}{K} KD} . \qquad (3)$$

Note that the latter form is similar to the energy equation with the addition of the k_p/K factor which expresses the additional attenuation of peak power due to pulse stretching for a fixed depth. To the extent that several of the high ω_0 plots are slightly curved, the normalized average power attenuation coefficient to a given optical depth will be a weak function of optical depth as seen in Fig. 25. These values of k_p/α as a function of αD can be combined with K/α values for the appropriate ω_0 from Fig. 22 to yield k_p/K curves as seen in Fig. 26.

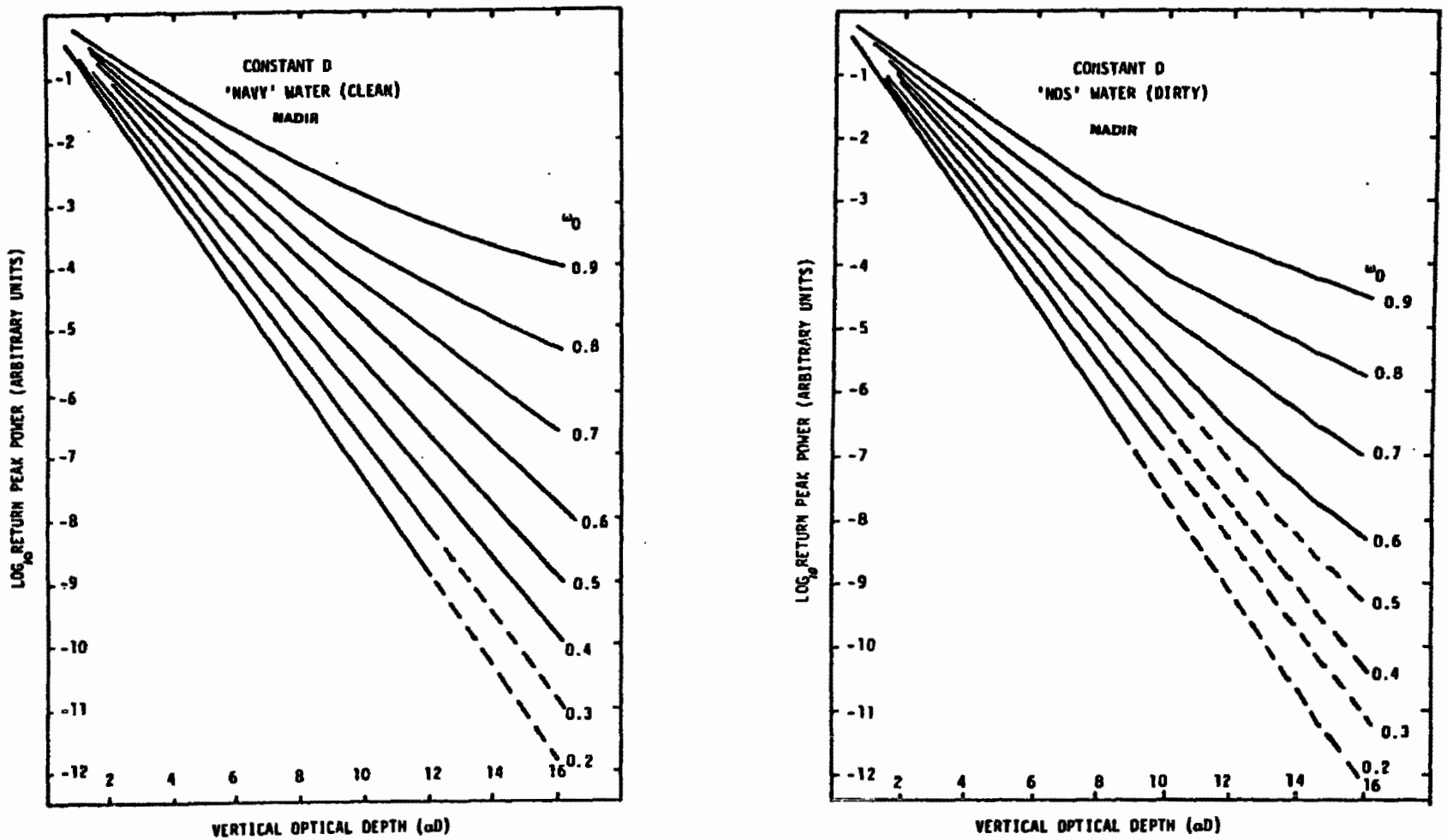

FIGURE 24. IRF PEAK POWER DECAY WITH OPTICAL DEPTH

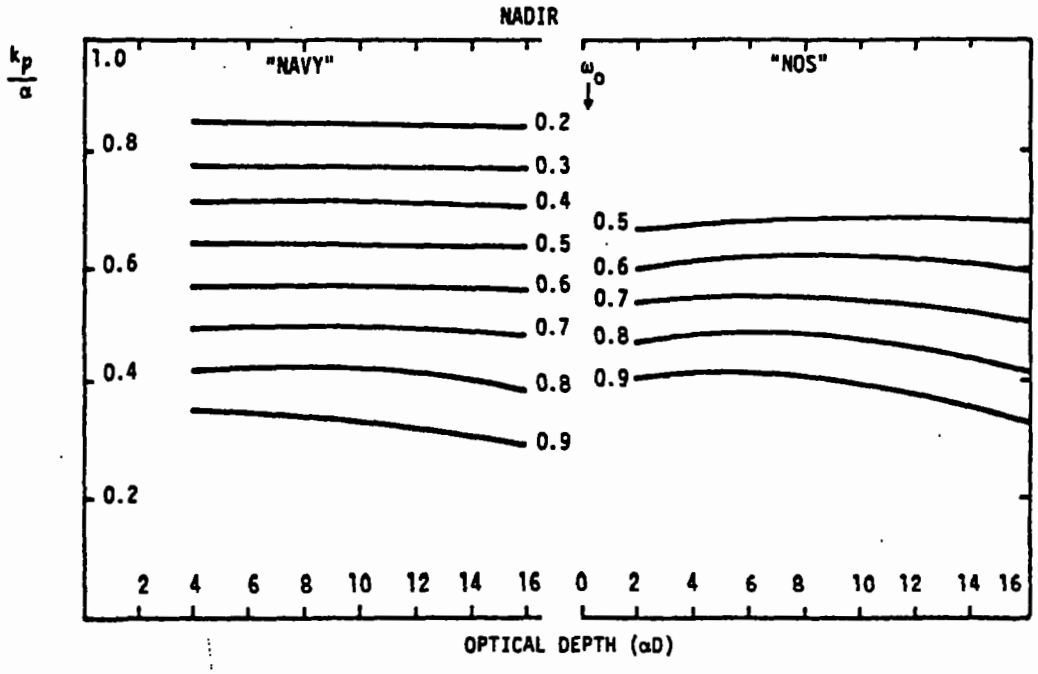

FIGURE 25. IRF k_p/α DEPENDENCE

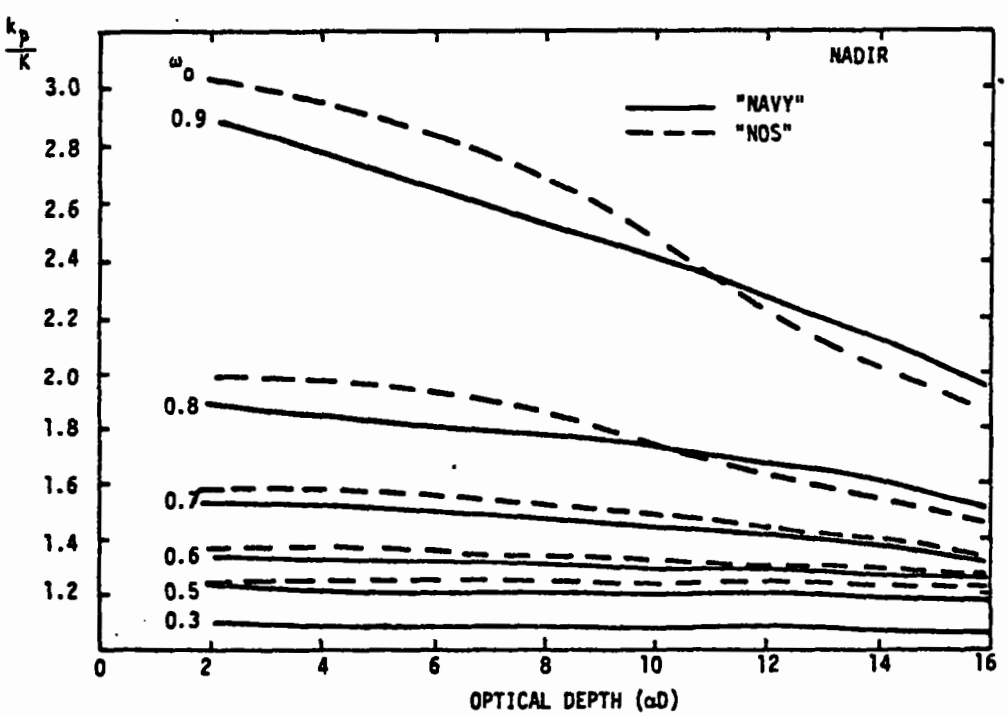

FIGURE 26. IRF k_p/K DEPENDENCE

This plot clearly demonstrates the dramatic extent to which the IRF power attenuation coefficient for fixed depth can exceed the diffuse oceanographic attenuation coefficient which is the system energy attenuation coefficient. Note that, depending on the inherent water optical parameters, the ratio ranges between 1.0 and 3.0 (and could be even higher if ω_0 were permitted to range as high as 0.95 for very dirty "Chesapeake Bay-type" water). The effect of ω_0 in the 0.7 to 0.9 range is very strong. The largest values occur for high ω_0 which involve the greatest scattering to absorption ratio, and hence the greatest pulse stretching. The optical depth effect is greater for higher ω_0. The phase function effect is seen to be comparatively small for all cases. Analytic expressions for k_p/K for this limiting IRF case were reported in Guenther and Thomas (1981a).

The off-nadir IRF peak power curves for the NAVY phase function are seen in Fig. 27 for constant D. At low αD the incremental power loss (slope) is greater for larger nadir angles due to the added physical path length to a given vertical optical depth. At high αD, where the mean flux approaches the vertical, the slopes approach the nadir case.

The above results have been derived for the IRFs scaled to a fixed depth. For a given αD, the IRF pulse stretching scales linearly with depth due to the geometric dependence of the time delays for returning photons. The received peak power for an impulse input to a water column of arbitrary depth can thus be written as $P_R \propto P_T \exp(-2k_p D)/D = P_T \exp[-2(k_p/K)KD - \ln D]$. The form on the right-hand side expresses the fact that the general IRF power equation is the energy equation modified by the addition of two terms in the exponent, k_p/K and $-\ln D$. Both of these reduce the peak power to pulse energy ratio since $k_p/K>1$.

This functionality can be rewritten algebraically as

$$\exp[-\alpha D(2\frac{K}{\alpha}\frac{k_p}{K} + \frac{\ln D}{\alpha D})]; \qquad (4)$$

and the absolute log-slope of the IRF power expression is thus the parenthetical quantity. For fixed depth plots such as Fig. 24, since K/α is constant for fixed ω_0, the upturn of the high ω_0 curves at high αD comes from

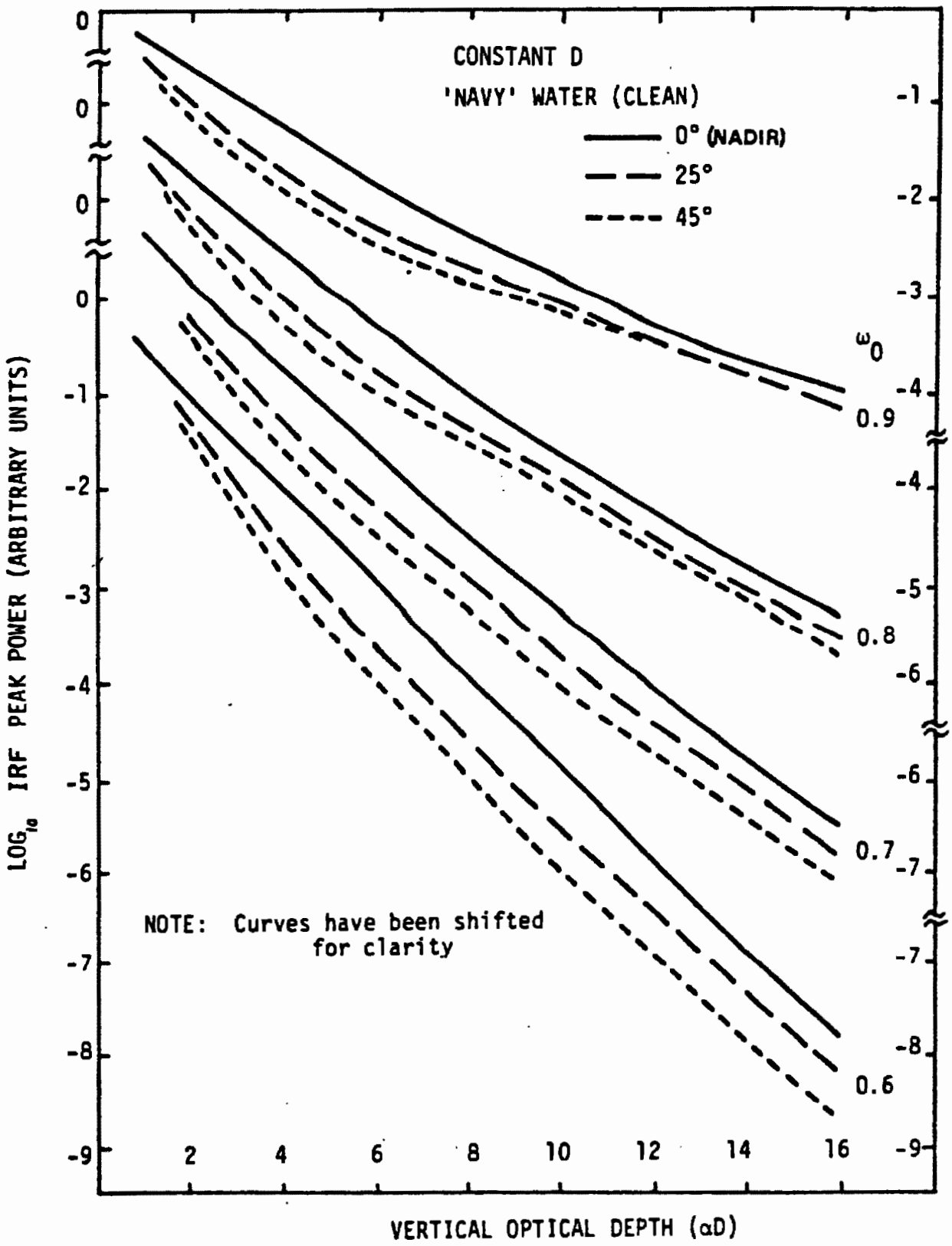

FIGURE 27. NADIR ANGLE EFFECT ON PEAK RECEIVED POWER

the $1/\alpha$ factor in the second term which is of significant magnitude compared to the first. For lower ω_0, the second term is relatively smaller compared to the first, due primarily to a higher K/α ratio, and the overall effect of this functionality is thus minimized. Similarly, if the IRF peak power versus αD curves are plotted for constant α, it can be seen from the slope expression that the high ω_0 curves will also turn up in a similar fashion as $\ln D/D$ decreases with increasing D. This bounding situation is depicted schematically in Fig. 28 along with the energy curve which represents the opposite bounding case of very long source pulse.

4.3.2 Environmental Response Results

For a practical system with a 5-10 ns source pulse, the peak power curve will lie between these two extremes: as pictured in Fig. 28, for low optical depths it will approximate the energy case, and for high optical depths it will converge to the IRF case. The rate of transition between these extremes depends on the incident laser pulse width. Pulse stretching and the associated loss of power compared to energy will not be evident until the duration of the impulse response becomes significant compared to the width of the incident pulse. This will begin to occur as both the physical depth and the optical depth increase. At large physical and/or optical depths, the impulse response will become broad, and the actual loss curve will tend toward the impulse response loss curve.

Specific peak power results have been generated for ERFs obtained by convolving the Monte Carlo-derived IRFs with a 7-ns (FWHM) triangular source pulse. As seen in Fig. 29 for $\theta=15°$, for $\alpha D < 16$ and to depths of at least 40 m, the peak power results can be described simply by exponentials with an effective increase in the system attenuation coefficient. This can be represented by the form $P_R \propto \exp(-2nKD\sec\phi)$, where, in general, $n=n(s,\omega_0,\theta)$ and ϕ is the nadir angle of the unscattered ray in the water. This is an understandable result based on the schematic representation in Fig. 28. The values of $n(s,\omega_0,\theta)$ are derived from semi-log plots of peak power versus optical depth for various fixed values of θ, ω_0, and α as seen in Fig. 29. The slopes of these lines are quite constant except at very low αD, and the nadir angle effect is quite small as noted by the dashed curves for 0° and 25°

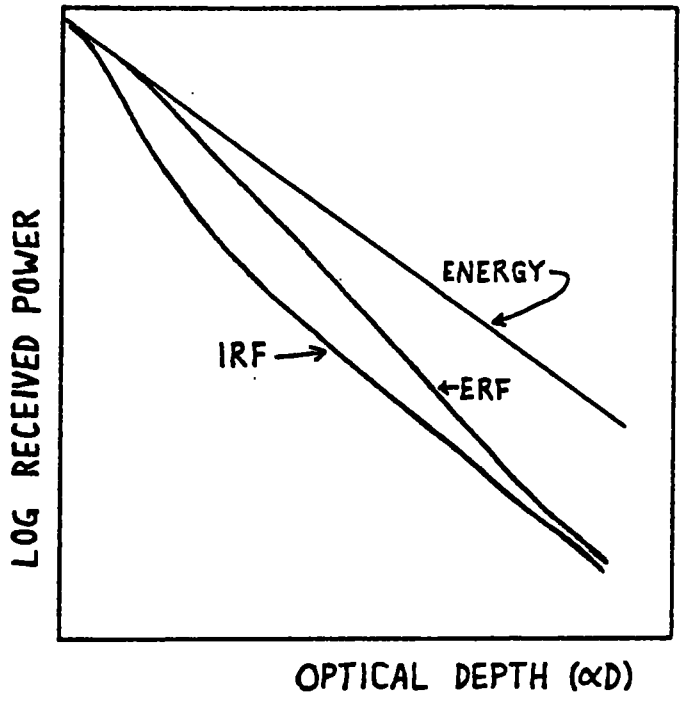

FIGURE 28. SCHEMATIC REPRESENTATION OF ERF PEAK POWER FUNCTIONALITY

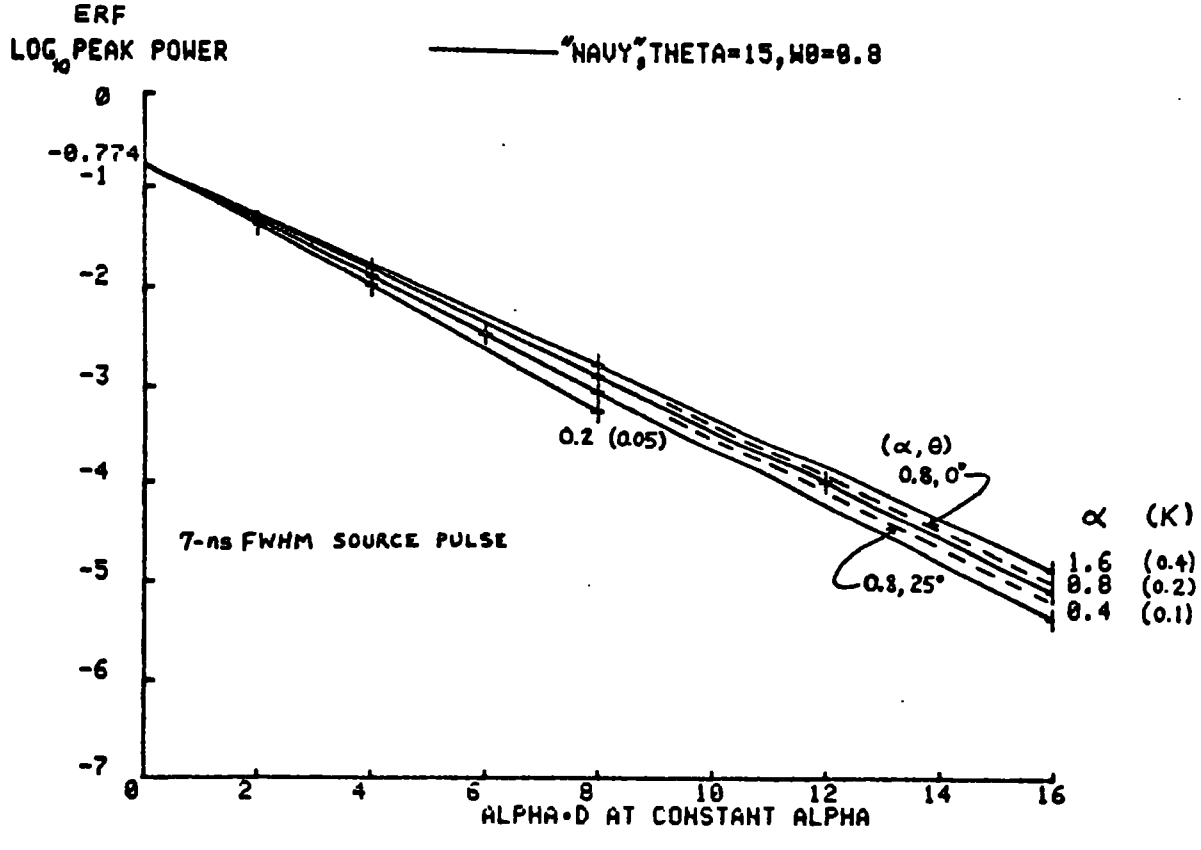

FIGURE 29. ERF PEAK POWER DECAY

at α=0.8 m^{-1}. The slopes are modeled as $-2nK\alpha^{-1}\sec\phi$; by measuring the slope and knowing K/α from ω_0, one can determine the values of n. In this way, the $\sec\phi_{eff}$ effects (as opposed to $\sec\phi$) are automatically included in the calculated values of n.

The calculated values of n are plotted in Fig. 30 for nadir incidence as a function of α and parameterized on ω_0. The dependence on the scattering phase function is small except at ω_0=0.9, which is separately noted on the figure. The residual nadir angle effect is quite small, as seen by the dotted line for 25° at ω_0=0.8. A plot such as Fig. 30 can be slightly misleading, because it represents exhaustive combinations of all possible parameter values, many of which are highly unlikely in natural waters. The ranges of ω_0 values typically associated with given α's in the environment are denoted in Fig. 31 as heavy lines. This changes the apparent behavior of n considerably, from one which decreases from large values for increasing α to one which rises gradually from small values with increasing α.

Various levels of approximation may be used for describing n depending on the estimation accuracy desired. A decent first-order approximation for natural waters is $n \cong 1.25$ for all cases. A slightly better fit, good to ±0.1, is provided by the expression $n \cong 1 + 0.27\ \alpha^{0.24}$, valid for all θ and ω_0 but limited to $\alpha \lesssim 2\ m^{-1}$. A more detailed fit can be obtained, if desired, in the forms $n = A\ \alpha^{-B}$ or $n = A\ s^{-B}$. The latter is more rigorous phenomenologically and was adopted. The most straightforward fits are obtained with the A's and B's expressed not directly in terms of ω_0, but rather in s/a which is equal to $\omega_0/(\omega_0 - 1)$. The selected model is thus

$$n(s,\omega_0,\theta) = A(s/a,\theta)\ s^{-B(s/a,\theta)}. \qquad (5)$$

The coefficients A and B can be expressed in the forms $A=c_1+c_2(s/a)$ and $B=c_3(s/a)^{c_4}$. The fits for various ranges of beam entry nadir angle are found in Table 1.

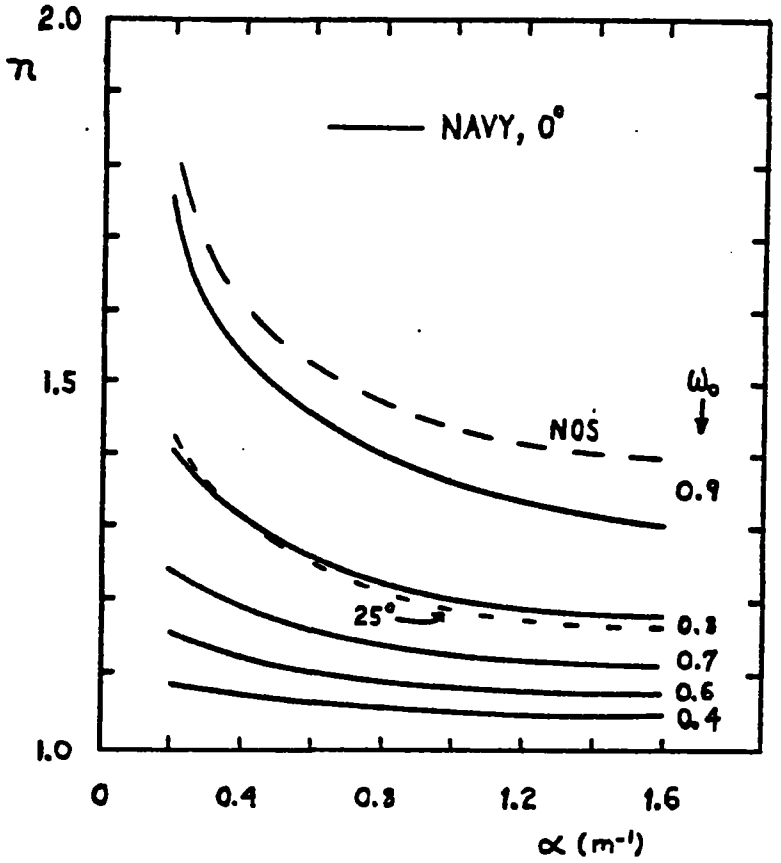

FIGURE 30. FULL EXPONENTIAL POWER DECAY FACTOR FUNCTIONALITY

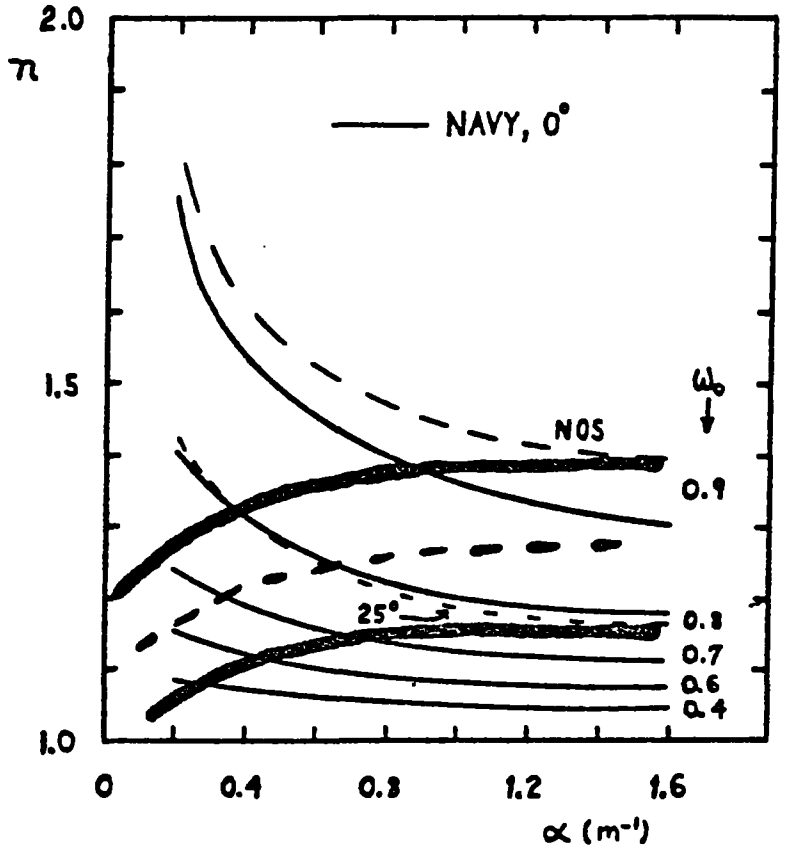

FIGURE 31. PRACTICAL EXPONENTIAL POWER DECAY FACTOR

Table 1. Regression coefficients for exponential power decay factor.

θ	c_1	c_2	c_3	c_4
0° - 15°	1.02	0.032	0.032	0.79
15° - 25°	1.03	0.035	0.042	0.69
25°	1.05	0.036	0.050	0.60
35°	1.11	0.024	0.072	0.54

One minor added refinement is possible. The curves of P_R versus αD for fixed α are slightly flatter at small αD's where they approximate the energy case. The extrapolated slopes from higher αD thus intersect the P_R axis ($\alpha D=0$) slightly above the actual value of P_T. An equation of the form $P_R \propto P_T \exp(-2nKD\sec\phi)$ consequently underestimates P_R slightly. To correct for this effect, the ratios of the extrapolated slope intercepts, P_T', to P_T have been calculated and denoted as "m" such that $P_R \propto m\, P_T \exp(-2nKD\sec\phi)$. A plot of m versus α for a range of nadir angles and $\omega_0 = 0.8$ is seen in Fig. 32. The m values are not as well-behaved as the n's, but they need not be, since they are linear rather than exponential factors. To a first order, one might simply select $m \cong 1.25$. For typical operational circumstances of $0.7 < \omega_0 < 0.9$, $0.2 < \alpha < 2\ m^{-1}$, and $15° < \theta < 25°$, an estimate good to about ±0.1 for either phase function is $m \cong 1.1 + 0.19\,\alpha$. In reality, the magnitude of this effect compensates for ignoring the air path losses and a little practical system detuning. It can consequently be ignored, as well, except for special cases where high accuracy is required, such as the estimation of water parameters.

For a practical case with a 7-ns source pulse, the peak power received from the bottom return, obtained by converting the received energy equation, may thus be described effectively as

$$P_R = \frac{P_T\ n\ R\ F_P\ A_R \cos^2\theta}{\pi\,(n_W\ H + D)^2}\, e^{-2\ n(s,\omega_0,\theta)\ K\ D\ \sec\phi}, \qquad (6)$$

where the n's are as reported previously.

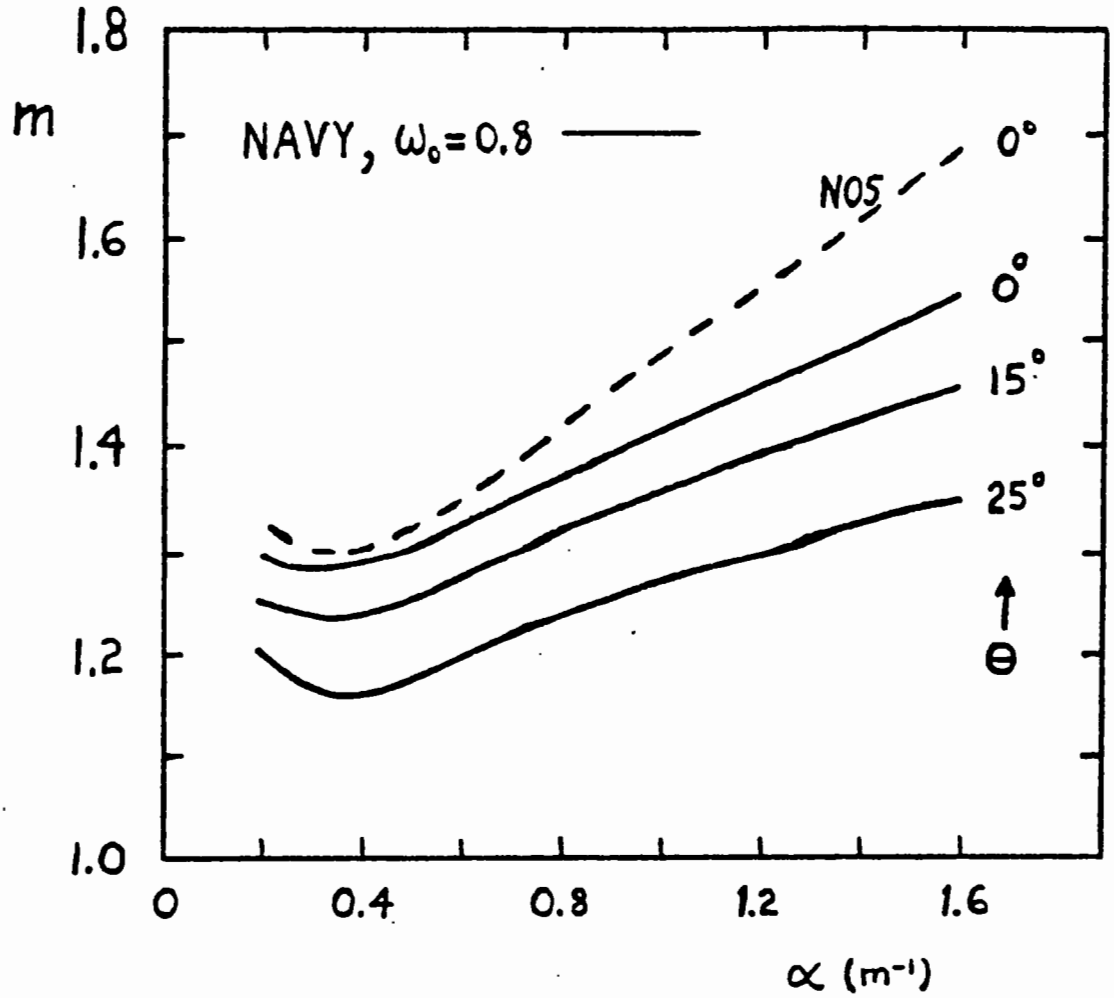

FIGURE 32. LINEAR POWER FACTOR

This signal rides atop the volume backscatter signal which decays roughly as exp(-2KD) with increasing depth. From the above form, it can be seen that a so-called "extinction coefficient", ξ_m, expected to be fairly constant for all water conditions (for a given system with specified altitude, nadir angle, etc.) can be defined in the form $\xi_m = nKD$. Since pulse stretching causes the peak bottom return power to decay at a rate which seems to be slightly faster with increasing depth than the volume backscatter signal, the latter appears to be a limiting noise source for nighttime operation.

The field-of-view factor, F_p, is different than that for the energy equation, because, as described in section 3.4, a loss of energy does not necessarily lead to a significant loss in peak power. An insufficient FOV which spatially excludes a portion of the returning signal reduces the F_p factor below unity in a highly complex way which depends on the FOV, water parameters, depth, altitude, and the duration of the incident source pulse. No detailed relationships have been derived for F_p other than to note the FOV required to maintain a value near unity.

It is important to reiterate here (because of confusion and expediencies in the past) that neither the bottom return energy nor the peak power depend unambiguously on the optical depth, αD. The optical depth alone cannot be used to predict maximum penetration depths because these are seen to depend explicitly on KD, and the relationship between K and α is a very strong function of ω_0. Furthermore, pulse stretching adds additional losses which have been characterized as an increased exponential loss factor.

5.0 BIAS PREDICTION

5.1 Methodology

In utilizing the forthcoming results, it is important to recall their origins and the bounds of their validity.

1) The impulse response functions (IRFs) are qualitatively depth independent and can be scaled to any water depth.

2) The so-called "environmental" response functions (ERFs) were generated by convolving depth-scaled IRFs with a triangle-shaped source function of 7-ns half-width. The ERFs are thus depth specific, and resulting biases are valid only for source pulse widths not significantly different from 7 ns.

3) Biases depend strongly on signal processing techniques and pulse location algorithms. Depth measurement biases have been calculated from the ERFs for two significantly different signal processing algorithms: linear fractional thresholds and HALS' log/difference/CFD. Other procedures will yield different biases.

4) The simulation is for a homogeneous water column and flat, horizontal surface and bottom. It was demonstrated, however, (Guenther and Thomas 1981c) that even unrealistically large inhomogeneities in water optical properties result in errors in bias estimation of less than ±10 cm. Reported biases include no surface return stretching effects such as geometry, waves, etc. Errors due to waves must be handled separately.

5) Simulations were conducted for what is considered to be bounding ranges of key water optical parameters: phase function, optical depth, and single-scattering albedo. Appropriate volume backscatter signals were appended to the leading edges of the ERFs for HALS-type processing because of the significant effect of backscatter decay slope on pulse location for such algorithms.

6) The simulation error in reported biases is estimated to be generally under ±5 cm.

5.2 Bias Computation

For a given set of depth-specific, simulated bottom returns (ERFs) parameterized on beam nadir angle and water optical properties, the first step

in calculating depth measurement bias predictions is the modeling of the various signal processing and pulse location estimation procedures. After the appropriate transfer functions have operated on the input signals, the apparent depth is calculated from the time interval between the detection locations of the surface return and bottom return pulses. For the reported biases, the source pulse was used directly as the surface return pulse (a mirror-like reflection from a flat surface), and a common pulse location algorithm was applied to each. It is conceivable that separate optimization of the surface and bottom return detection algorithms might be desirable. If so, locating the two pulses at different thresholds, for example, would cause an additional bias which depends only on the shape of the interface return and which could be removed with a pre-calculated corrector.

Depth measurement biases were calulated from the ERFs for two diverse types of pulse location algorithms: a straightforward amplitude threshold proportional to the peak height applied to the linear input (the so-called linear fractional threshold or LFT), and the complex HALS protocol which involves logarithmic amplification for amplitude compression, a time-delayed difference operation to remove the volume backscatter signal, and pulse location by a specialized constant fraction discriminator (CFD) algorithm as implemented on an available hardware chip. Further details of the HALS processing procedures can be found in Guenther (1982). Each basic algorithm is represented by multiple sets of biases corresponding to selected values of imbedded parameters.

Linear fractional threshold detections are obtained directly from the ERFs. Because the HALS processing involves two time-delayed differences, however, the resulting pulse detection time depends not only on the shape of the ERF, but also on the log slope of the volume backscatter signal which precedes it. The effect can be quite significant in "dirty" waters where the backscatter slope is steep. In order to provide accurate bias predictors for the case of HALS processing, the specific volume backscatter signal associated with each ERF has been appended to the start of that ERF.

For a given ERF, the parameters αD, D, and ω_0 are specified. The value of α is thus known, and given ω_0, the K/α ratio can be derived from the "best

fit" relationship shown in Fig. 22. K is thus uniquely defined for each ERF. The decay of the volume backscatter power is exponential in time with a log slope roughly equal to -cK (see section 6), where c is the speed of light in water. For HALS processing, the volume backscatter signal for each ERF is constructed in log space by extrapolating a line of appropriate slope backward from the first point of the logged ERF. This composite signal is then further processed, as follows.

Three waveforms associated with the log/difference/CFD process are seen in Fig. 33. At the top is the logged ERF input with associated volume backscatter tail; in the middle is the output of the delayed difference operation; and at the bottom is an internal CFD signal for which the positive-going zero crossing is the detection point. The delayed difference operation applied to the decaying volume backscatter signal produces a constant negative level into the CFD which violates one of the assumptions associated with performance of the CFD circuit. The negative input level, whose magnitude increases with decreasing water clarity, causes delayed detections and leads to added positive biases which depend on the delay times, water clarity, signal-to-background ratio, etc. These perturbations of the propagation-induced biases by the processing protocol automatically become part of the final results, however, and need not be separately handled.

The bias calculation for any signal processing and pulse location algorithm is based on the timing diagram shown in Fig. 34, where t_D is the time associated with the "true" slant range, and t_A is the time associated with the "apparent" slant range measure at the detection point. The "measured" bottom pulse location time, t_M, for a given algorithm and the "reference" time, t_R, for the unscattered ray can be measured from any consistent starting time, as long as it is the same for both, because only their difference is important. The time base origin in Figs. 12 and 13 conforms to the arbitrary notation of Fig. 34 in which the source pulse is assumed to start at the time of the impulse. The surface pulse half-width (FWHM) is $t_{W/2}$, and the surface pulse location time, t_S, is measured from the start of that pulse. It can be seen in Fig. 34 that t_D and t_A are related by the expression

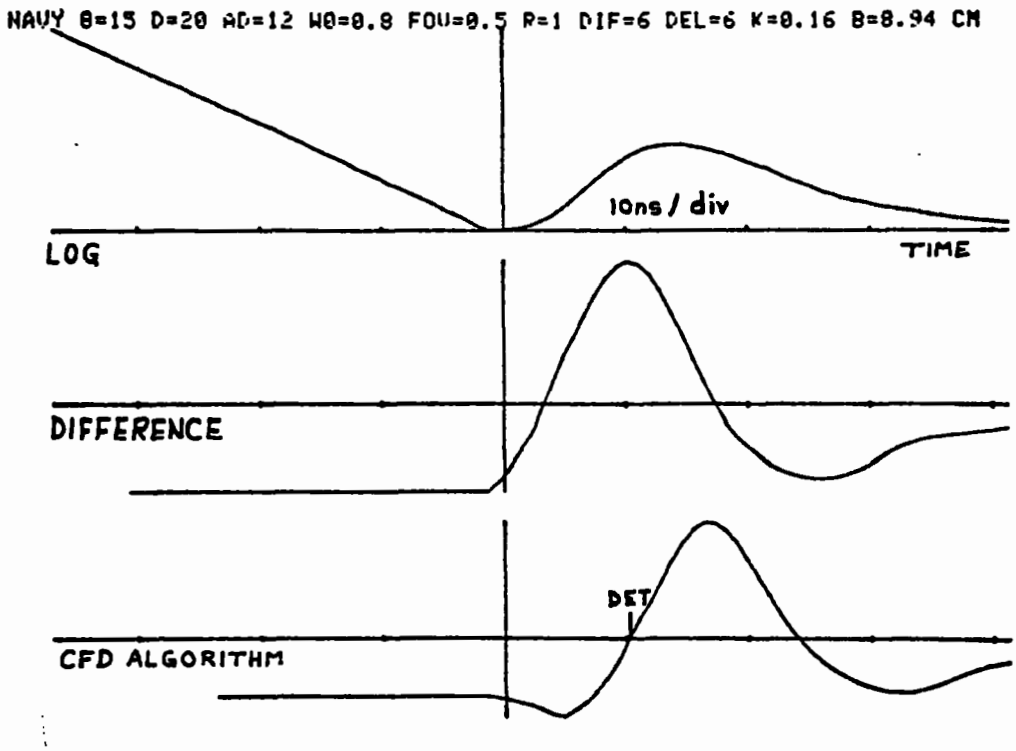

FIGURE 33. TYPICAL CFD WAVEFORMS

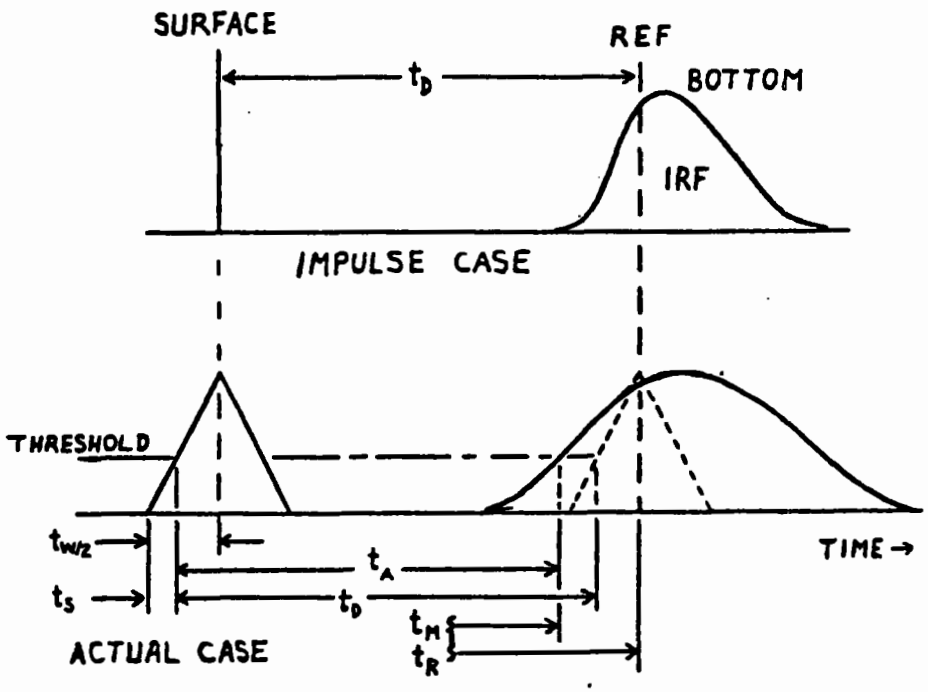

FIGURE 34. BIAS CALCULATION TIMING DIAGRAM

$$t_D = t_S + t_A + t_R - t_M - t_{w/2}. \tag{7}$$

The slant range bias time, t_B, is then

$$t_B \equiv t_A - t_D = t_M - t_R - t_S + t_{w/2}, \tag{8}$$

and the associated depth measurement bias will be $B = (c\ t_B \cos\phi)/2$, where B is positive for "deep" biases and negative for shallow biases. To calculate the bias time, t_B, one obtains $t_M - t_R$ from the processed bottom return pulse and t_S from the processed surface return pulse. As was noted in Guenther (1982) for HALS processing, the detection time, t_S, on a high signal-to-background ratio (P_m/B) triangular pulse is equal to the CFD delay. The CFD delay has thus been used for t_S in calculating HALS biases. This relationship becomes less exact for $P_m/B \lesssim 10$ and for significantly different pulse shapes. If extremely weak or highly distorted surface returns were encountered, a set of correctors (parameterized on P_m/B) would be necessary. HALS biases are small but non-zero at $\alpha D=0$ due to the P_m/B effect.

Biases were calculated for all combinations of physical depth, receiver parameters, pulse location algorithms, and relevant water optical properties (phase function, optical depth, and single-scattering albedo). It can be noted that the changes in bias predictors from the old sets in which the air path was ignored are all negative (in the shallow direction), as expected, and that the magnitudes of the differences increase with increasing nadir angle, with increasing optical depth, and with earlier detection times. For large optical depths, the bias changes at a 25° nadir angle due to inclusion of the air-path effect vary from about 20 cm for the 50% threshold to about 90 cm for the HALS algorithm with 6-ns delays. The nadir results, which were expected to be relatively unaffected, agree to within about ± 1 cm RMS.

The biases and their functionalities are discussed in the following sections, and a complete set of biases is tabulated in Appendix A for future reference. Earlier biases reported in tables and plots in NOAA Technical Report OTES 3 (Guenther and Thomas 1981b) are outdated, as are the references to a bias correction procedure using water optical parameters estimated from the air. This new report supercedes and replaces the results and conclusions in OTES 3 as well as expanding significantly upon its content.

5.3 Bias Sensitivities

Because the depths are measured with leading edge pulse location algorithms, the biases are based primarily on the photons which traverse the shortest, and hence least attenuated paths. The shape of the leading edge is thus largely determined by the scattering, rather than the absorption characteristics of the water. It makes sense, therefore, to consider the scattering optical depth, $sD=\omega_0 \alpha D$, the mean number of scattering events to the bottom, as a likely candidate for the major functional bias dependence, regardless of separate values of ω_0 and αD. Wilson (1979) showed similar functionalities for the radiance and irradiance distributions.

This relationship is demonstrated with the NAVY phase function in Figs. 35 - 37 for LFT and Figs. 38 - 40 for HALS. Note for all figures: under ALG for "algorithm", the description block in the figures lists an "L" for LFT followed by the threshold fraction in parentheses and a "C" for CFD followed by values for P_m/B and the CFD delay in nanoseconds, respectively. All HALS examples shown are for a difference operation with a 6-ns delay. The three curves in each family are for ω_0 values of 0.9, 0.8, and 0.6. The groupings are relatively tight regardless of nadir angle, depth, or processing protocol, although the groups exhibit less variation for LFT processing than for the more complex and non-linear CFD processing. Similar groupings occur for the NOS phase function but at somewhat different bias values.

This is a useful result because it reduces the number of bias-driving parameters whose values are not known a priori from three (phase function, αD, and ω_0) to two (phase function and $\omega_0 \alpha D$). The potential utility of this relationship is discussed in section 6. The figures supporting the text are plotted with either optical depth or scattering optical depth as the independent variable. Optical depth has been used at times for clarity or convenience, often where a single "average" value such as $\omega_0=0.8$ is plotted. In such cases the results may be easily generalized by multiplying the abscissa values by the appropriate ω_0.

The sD dependence is by no means "perfect" because of the effects of signal processing. For example, with HALS-type processing, the effect of the

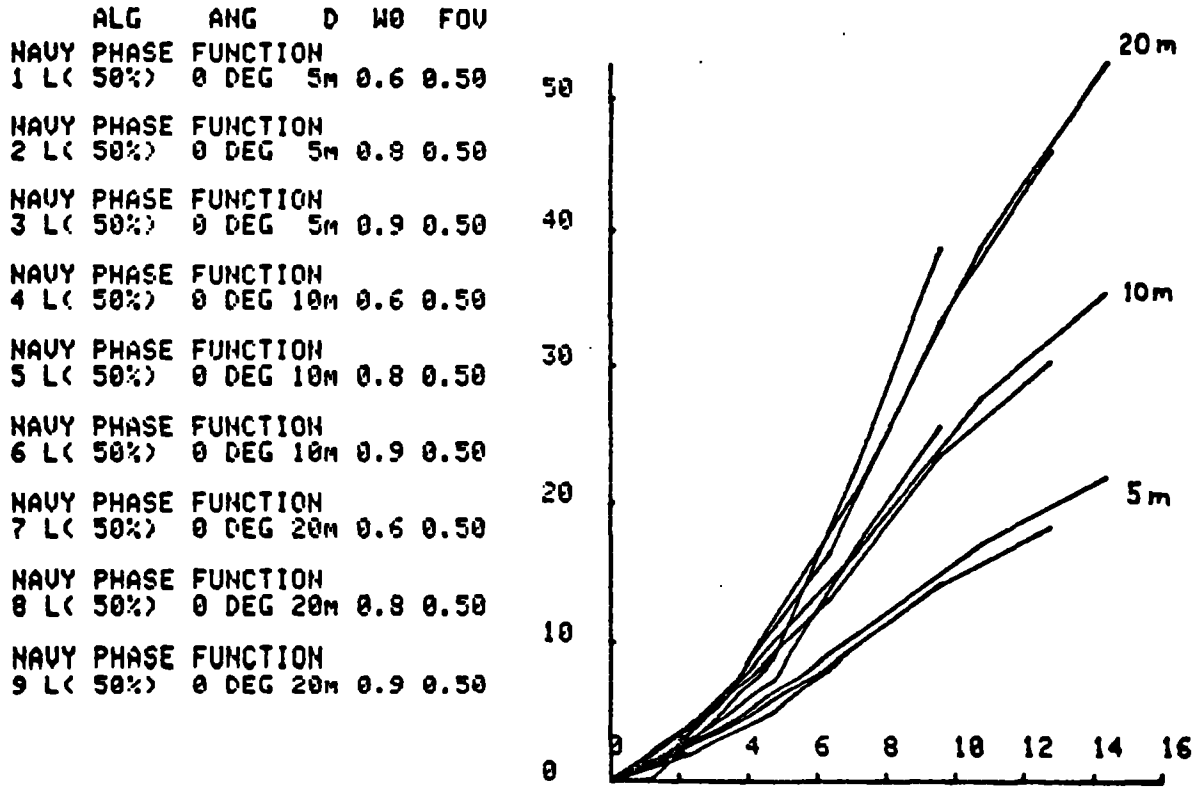

FIGURE 35. DEPTH MEASUREMENT BIAS (CM) VS SCATTERING OPTICAL DEPTH

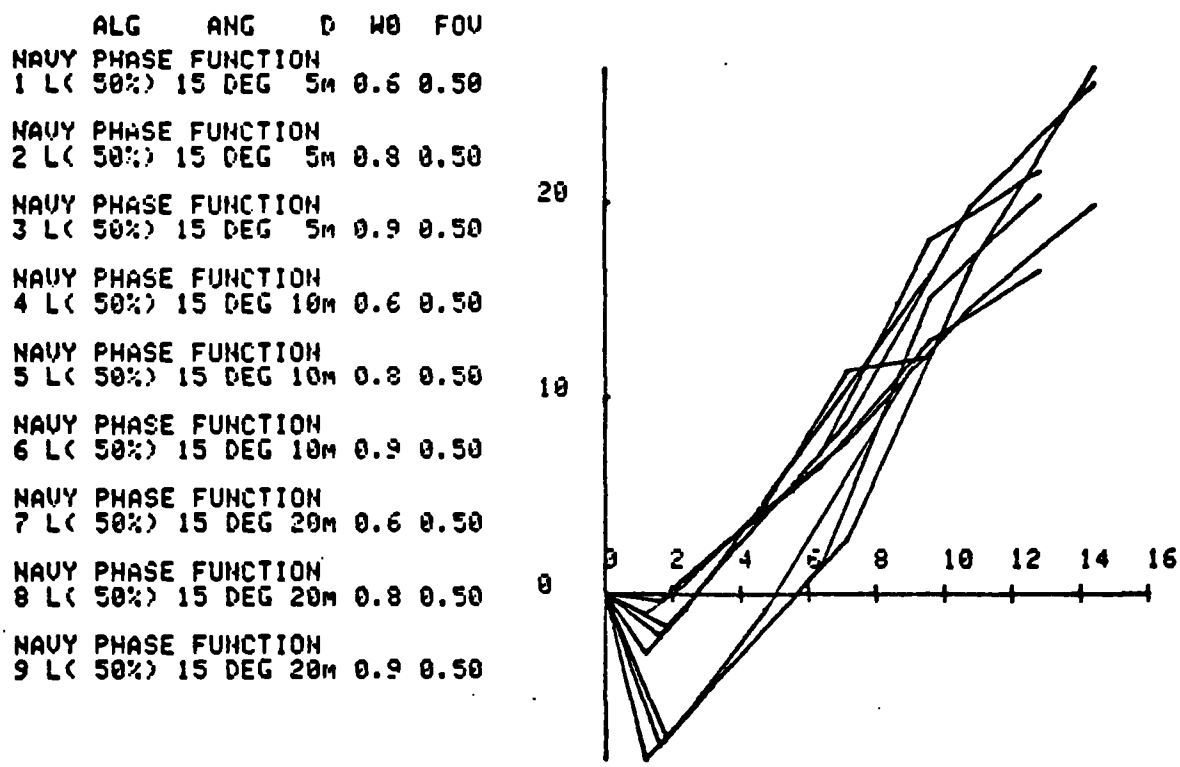

FIGURE 36. DEPTH MEASUREMENT BIAS (CM) VS SCATTERING OPTICAL DEPTH

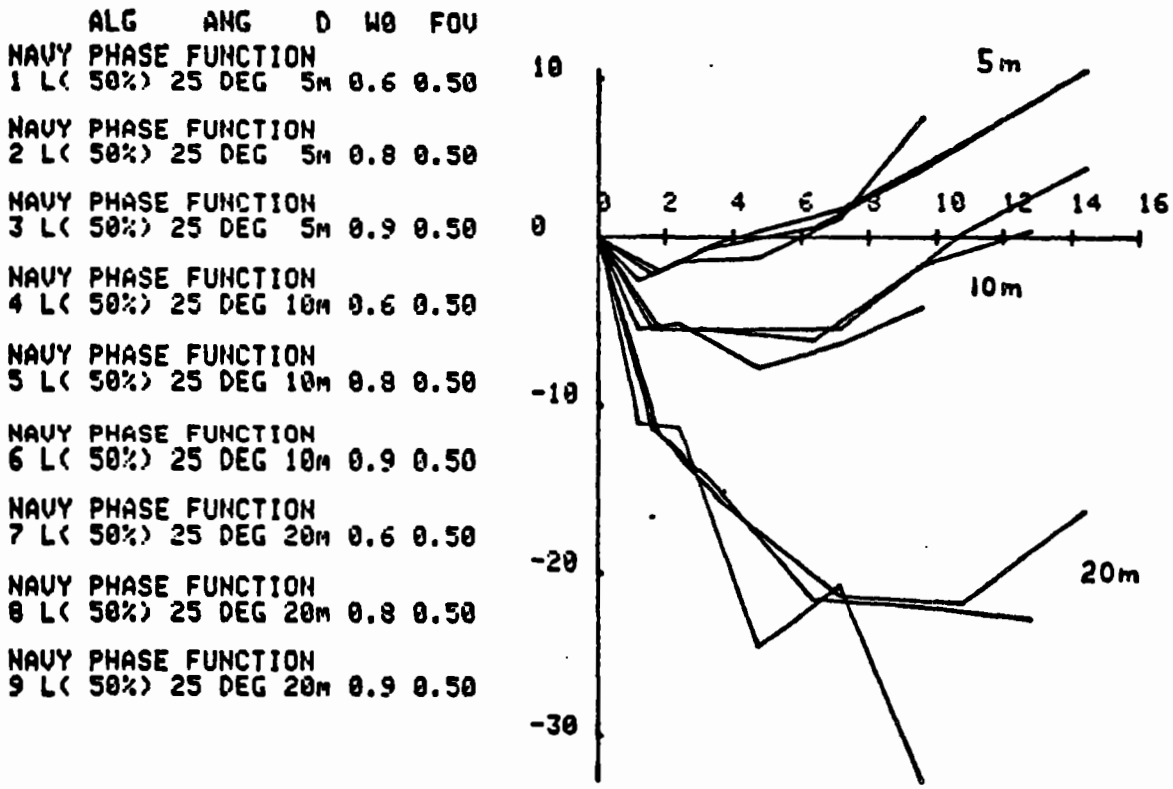

FIGURE 37. DEPTH MEASUREMENT BIAS (CM) VS SCATTERING OPTICAL DEPTH

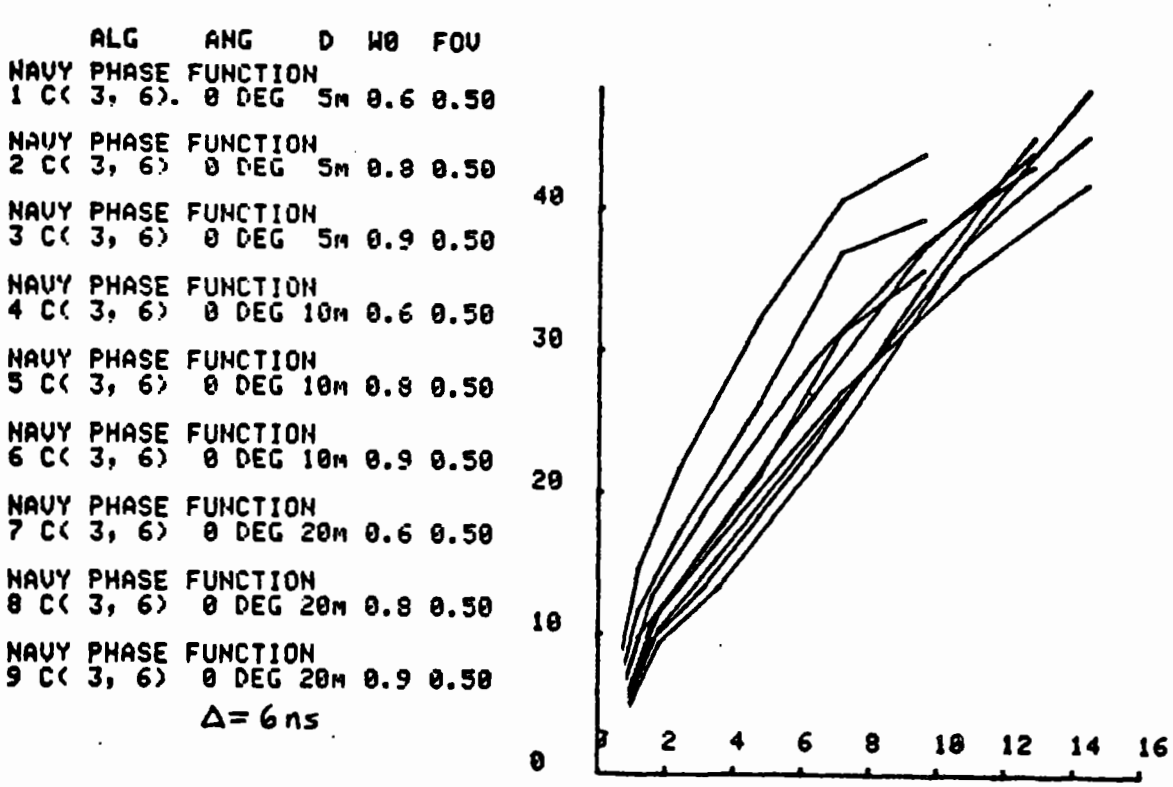

FIGURE 38. DEPTH MEASUREMENT BIAS (CM) VS SCATTERING OPTICAL DEPTH

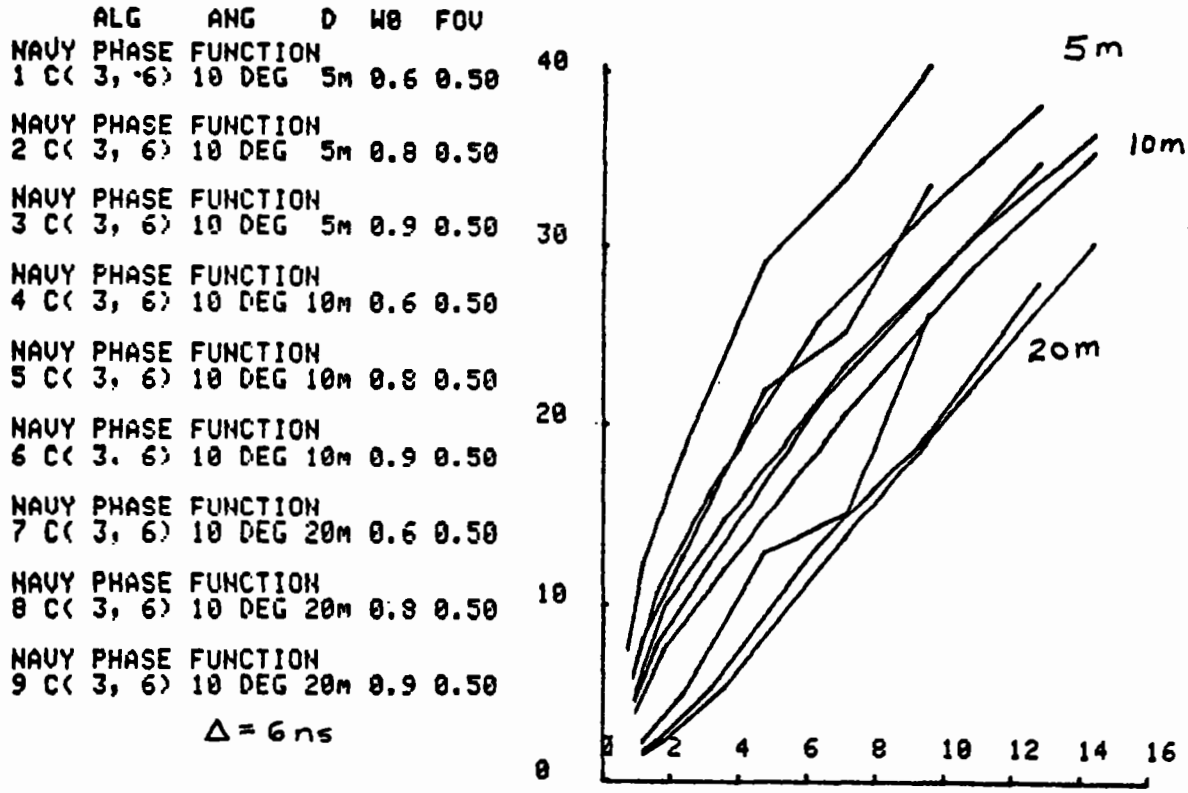

FIGURE 39. DEPTH MEASUREMENT BIAS (CM) VS SCATTERING OPTICAL DEPTH

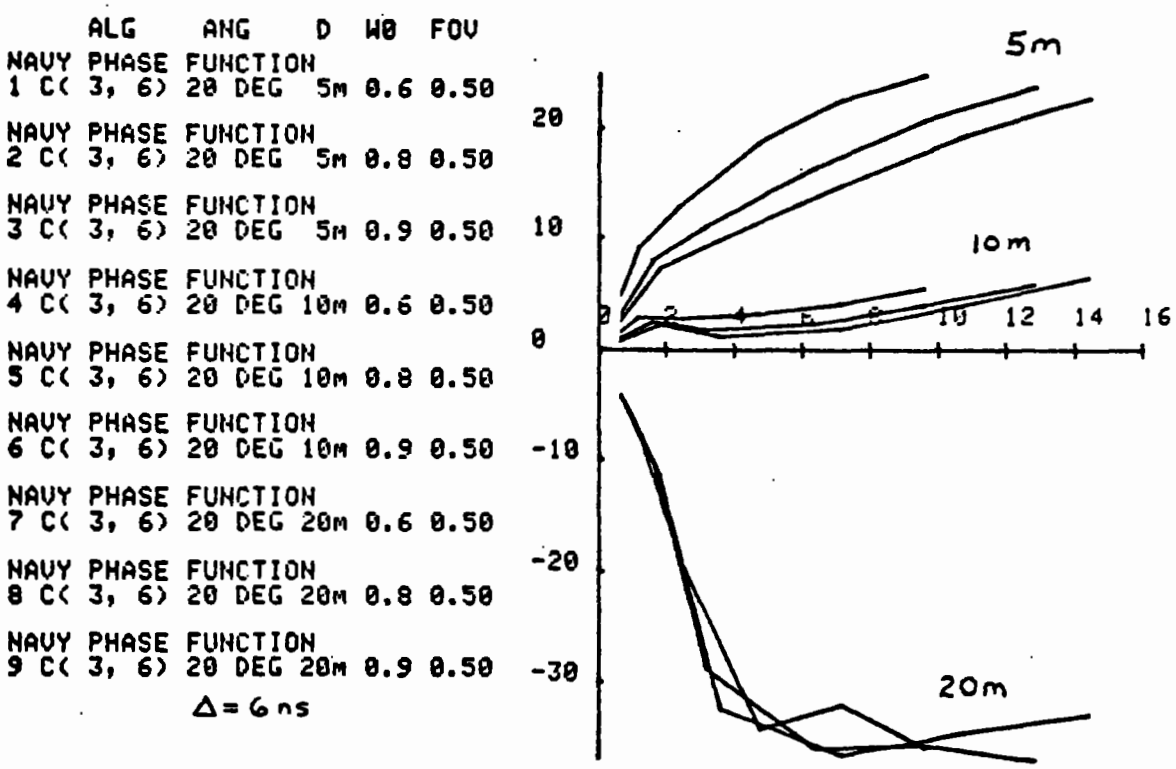

FIGURE 40. DEPTH MEASUREMENT BIAS (CM) VS SCATTERING OPTICAL DEPTH

volume backscatter signal competes with the ω_0 effect. By itself, small ω_0 leads to more negative biases due to higher absorption and an emphasis on the shortest path -- which is in the undercutting region. On the other hand, for a given α, lower ω_0 leads to higher values of K and larger negative input levels to the CFD from the backscatter signal. This, in turn, leads to delayed detections and subsequently more positive biases, particularly at shallow depths and low P_m/B. This is strikingly evident in the 5-m curves in Figs. 35 - 40. The net results of this competition are depth and ω_0 effects which are somewhat different for HALS processing than for LFT.

The phase function effect is demonstrated in Figs. 41 and 42. For nadir angles of 10° or more, the differences are typically under 10 cm between the "NAVY" and "NOS" phase functions which are considered to be more or less bounding for expected coastal waters. The bias differences are considered to be small enough that an average value between the two can be used for bias prediction. For that reason, much of the following demonstration of bias sensitivities will highlight only one, the "NAVY" phase function.

The effects of the air nadir angle for depths of 5 m, 10 m, 20 m, and 40 m are seen in Figs. 43 - 46 and 47 - 50 for LFT and HALS respectively. Note in each case the orderly progression toward more negative (shallow) biases as the nadir angle increases. This is due to the proportionately larger effect of "undercutting" at larger incident angles. It can be seen that there is tremendous variation in both the bias trends and magnitudes for the two different processing and pulse location protocols. The HALS log/difference/CFD biases are consistently more negative due mostly to later detection on the surface return but also partly to earlier detection on the leading edge of propagation-stretched bottom returns. Note also the tendency toward larger biases (both positive and negative) at larger physical depths due to the fact that the depth acts as a scaling factor for the normalized time delays. The effect of physical depth for constant nadir angles is illustrated directly in Figs. 51 and 52.

It may be noted in Figs. 49, 50, and 52 that the HALS biases for large nadir angles and moderate-to-large depths become very large and negative for optical depths as small as 2. By analyzing the waveforms, it can be seen that these biases are real but an artifact of the processing. The algorithm

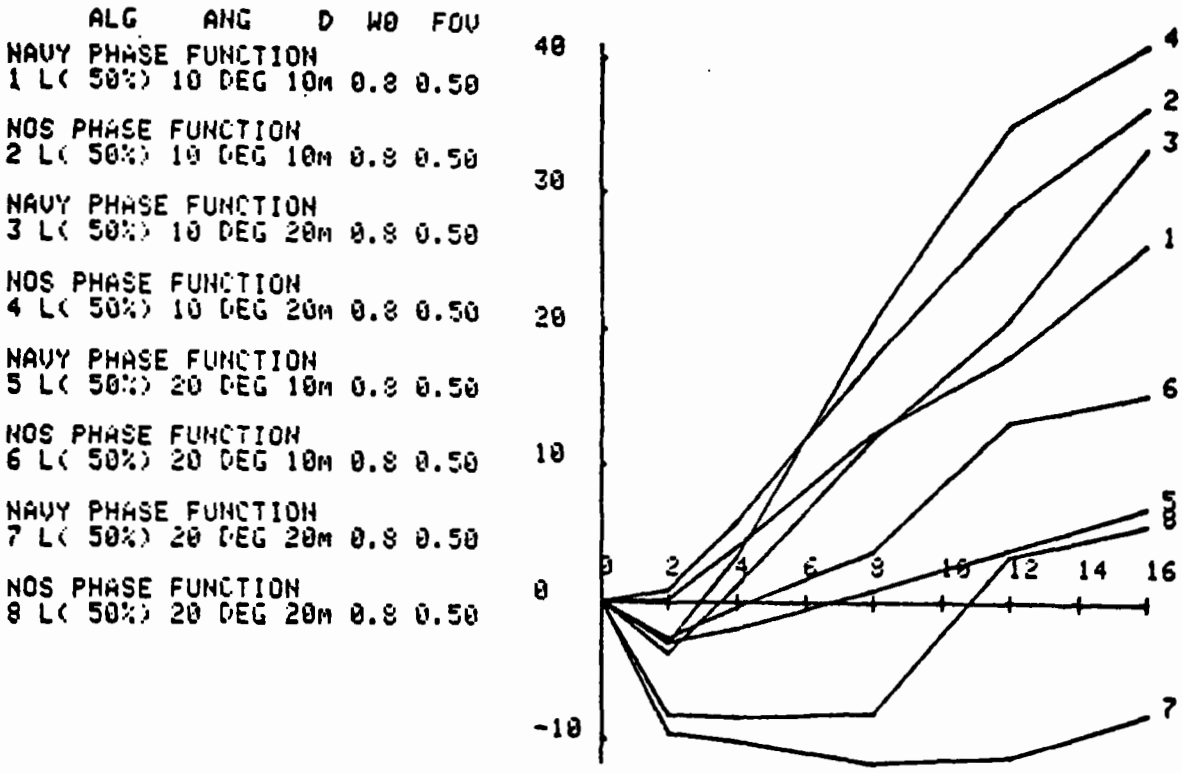

FIGURE 41. DEPTH MEASUREMENT BIAS (CM) VS OPTICAL DEPTH

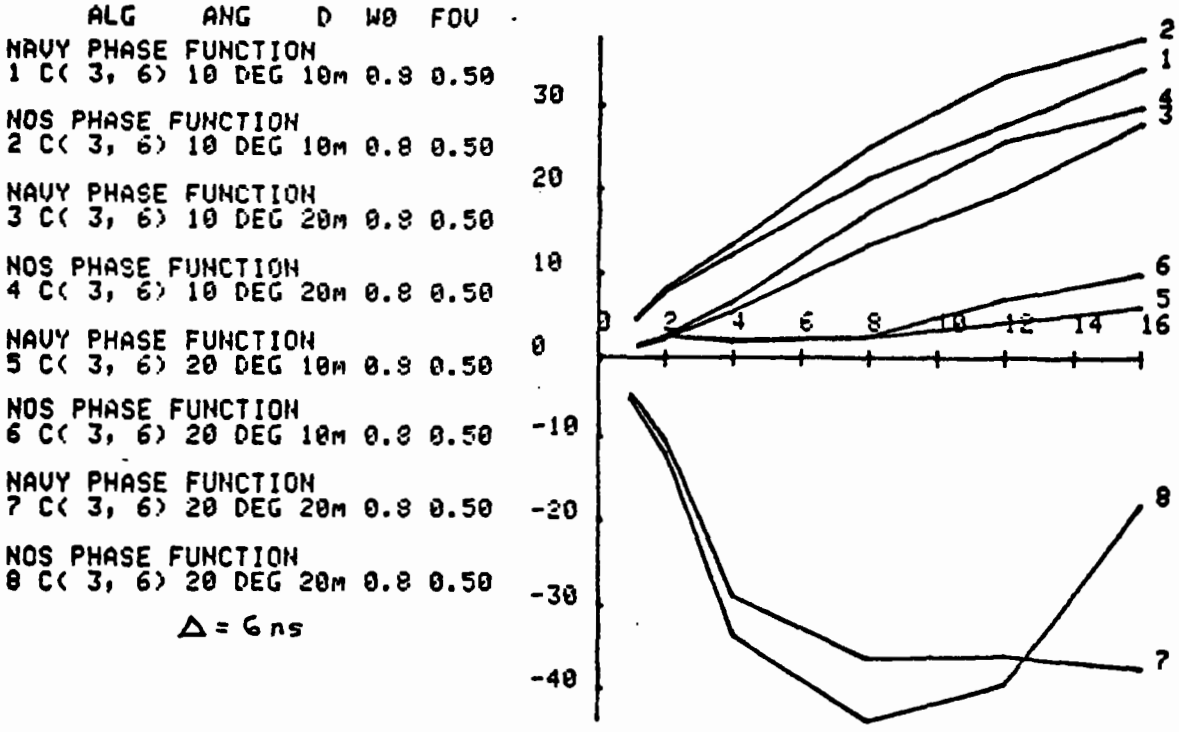

FIGURE 42. DEPTH MEASUREMENT BIAS (CM) VS OPTICAL DEPTH

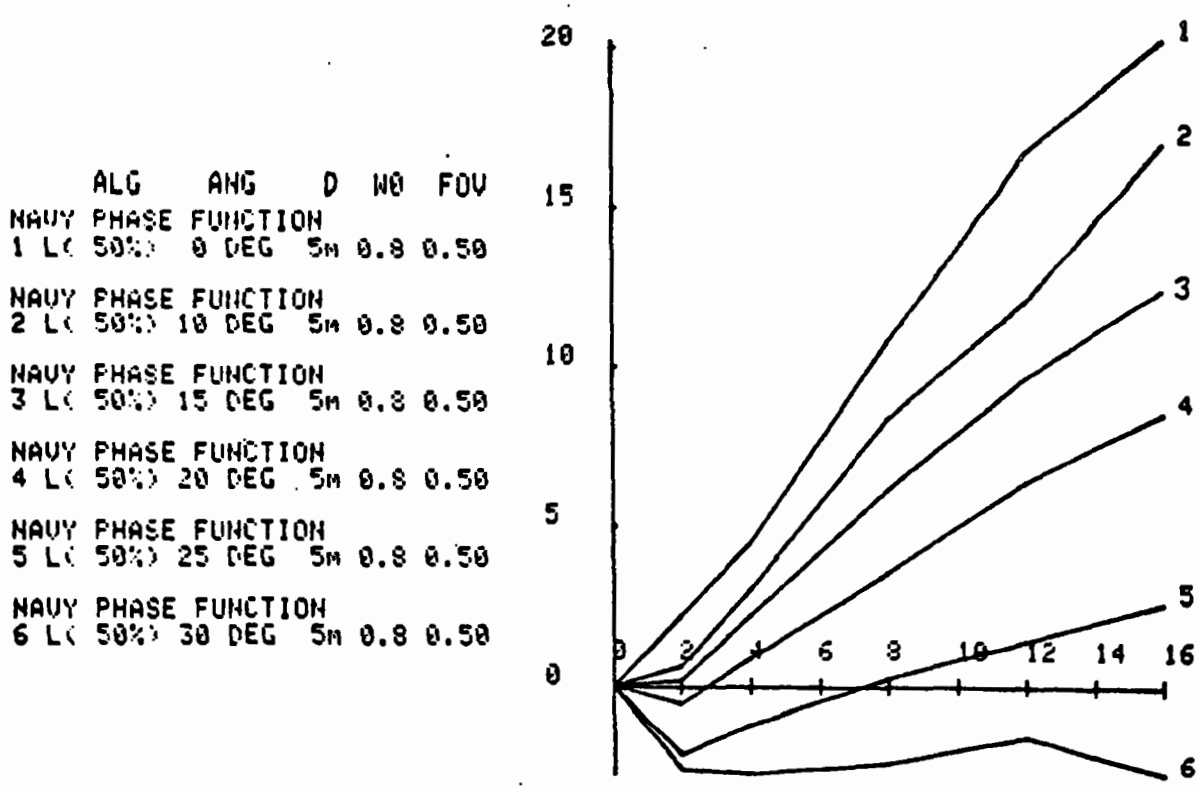

FIGURE 43. DEPTH MEASUREMENT BIAS (CM) VS OPTICAL DEPTH

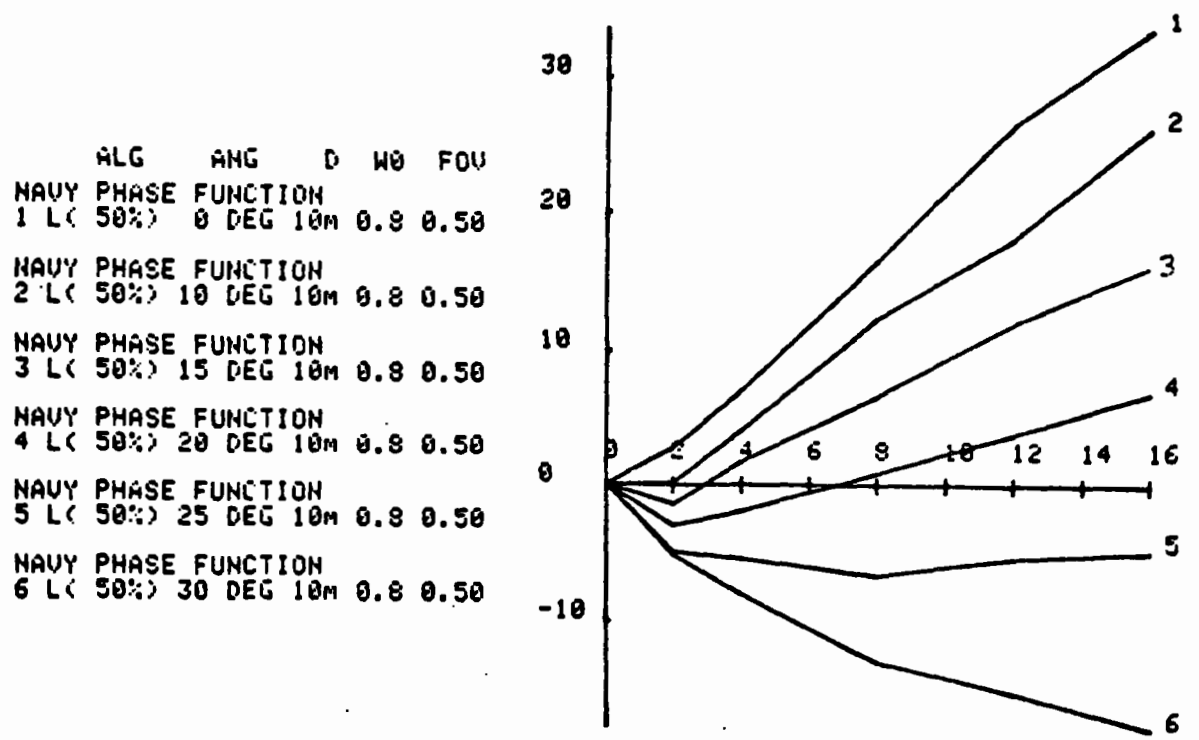

FIGURE 44. DEPTH MEASUREMENT BIAS (CM) VS OPTICAL DEPTH

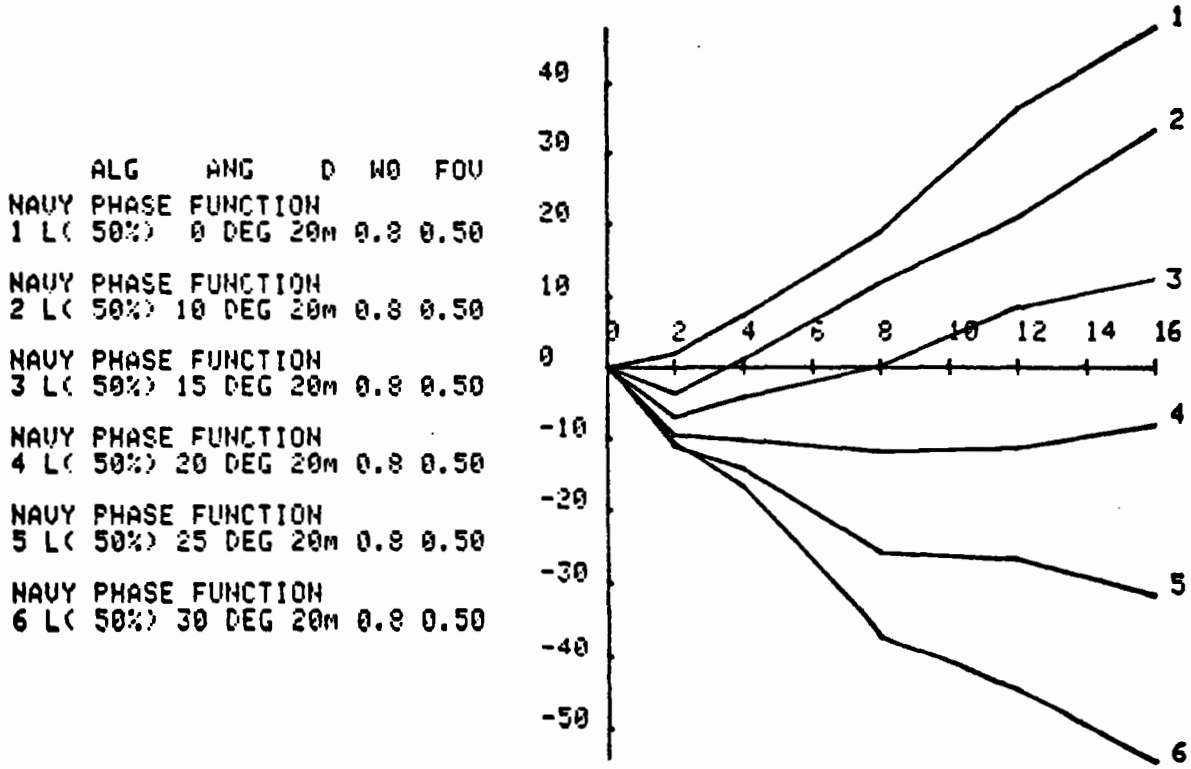

FIGURE 45. DEPTH MEASUREMENT BIAS (CM) VS OPTICAL DEPTH

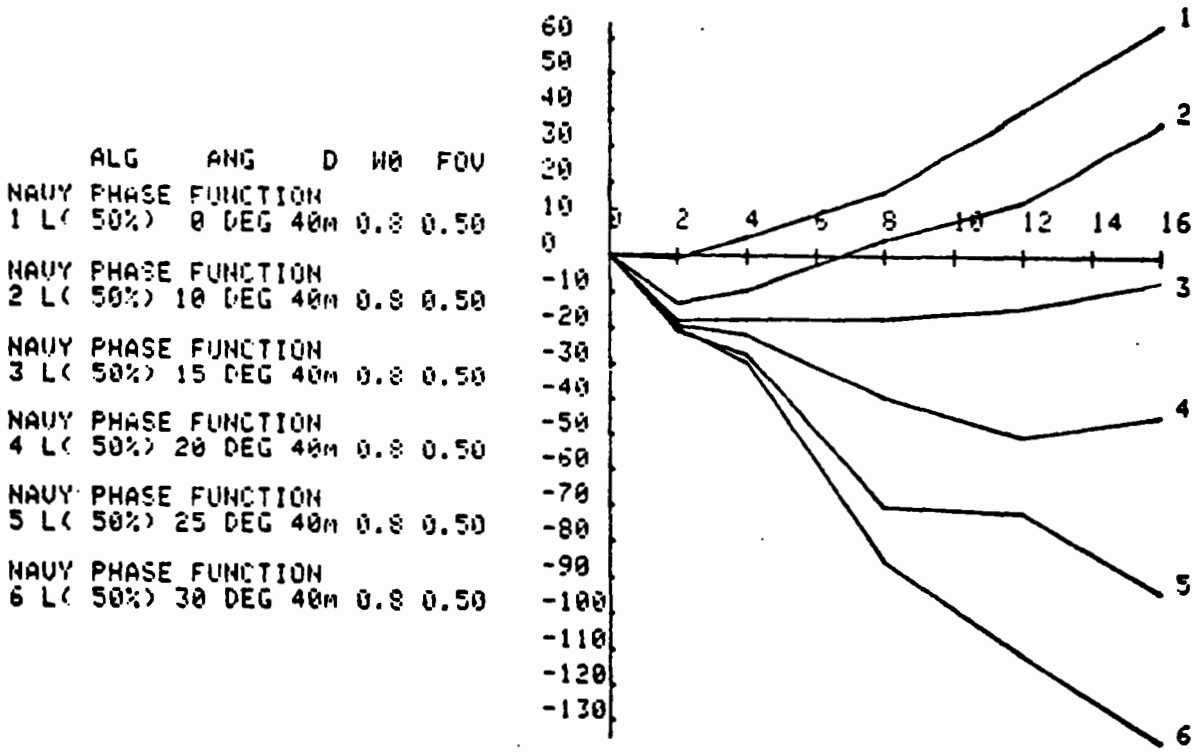

FIGURE 46. DEPTH MEASUREMENT BIAS (CM) VS OPTICAL DEPTH

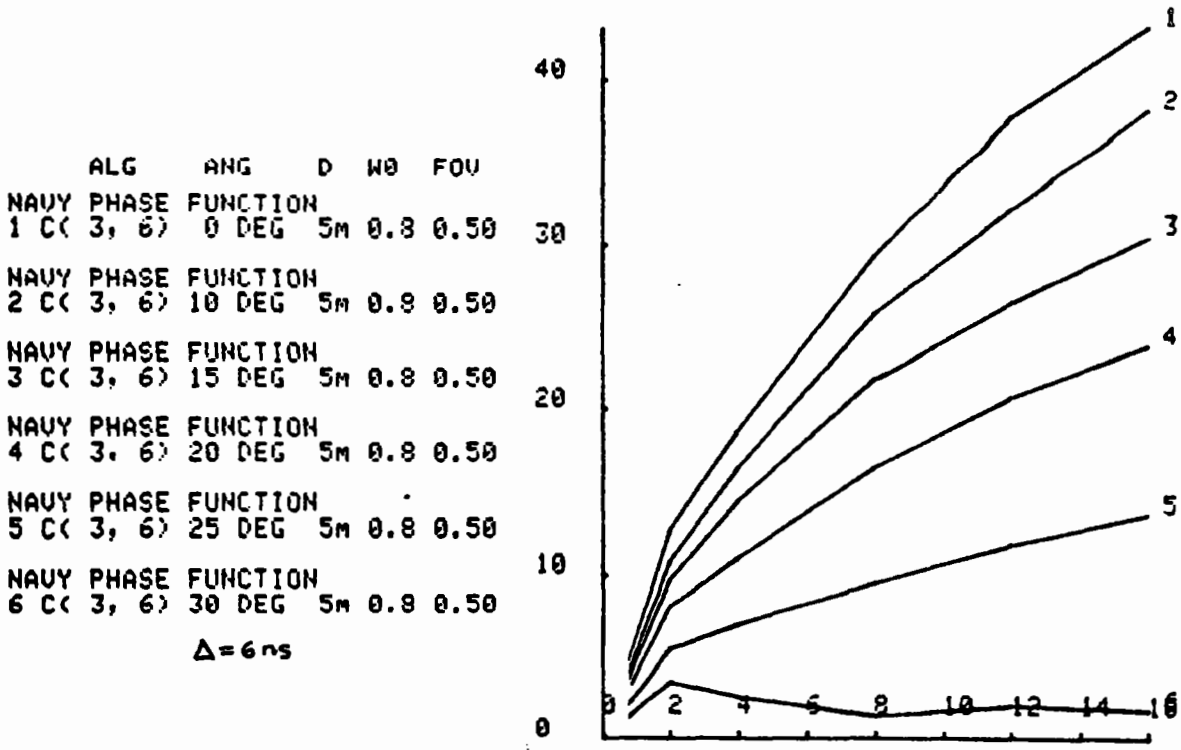

FIGURE 47. DEPTH MEASUREMENT BIAS (CM) VS OPTICAL DEPTH

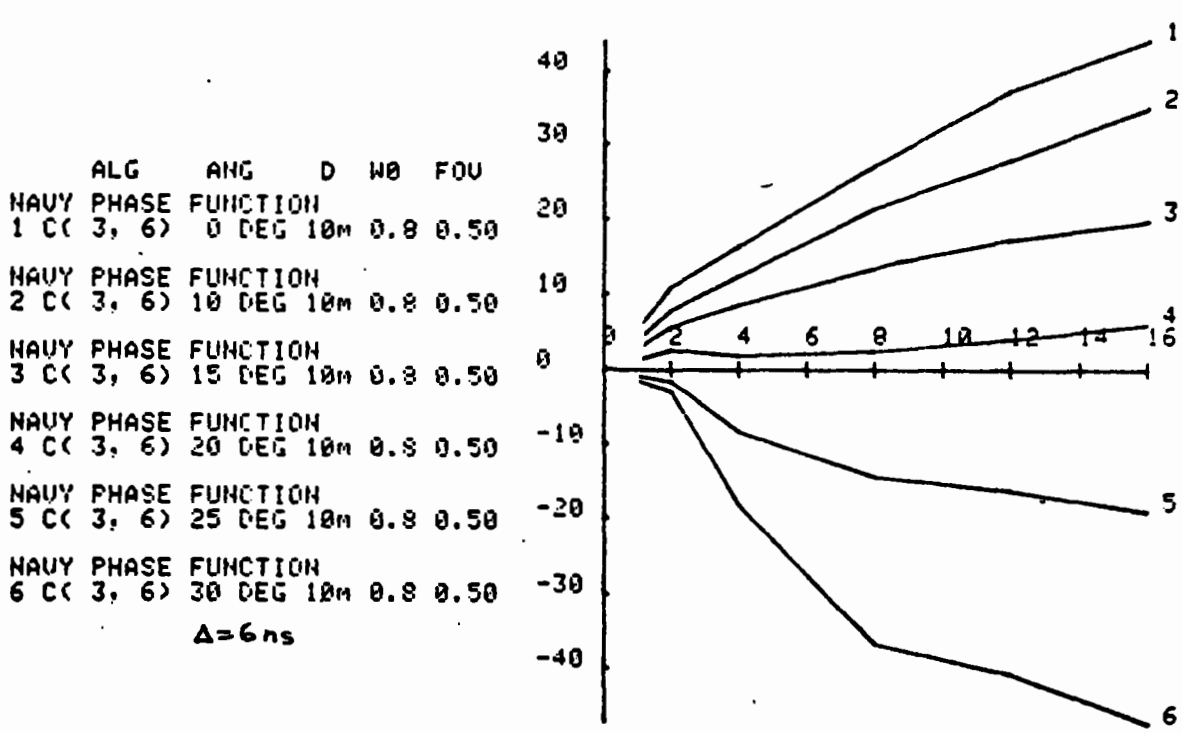

FIGURE 48. DEPTH MEASUREMENT BIAS (CM) VS OPTICAL DEPTH

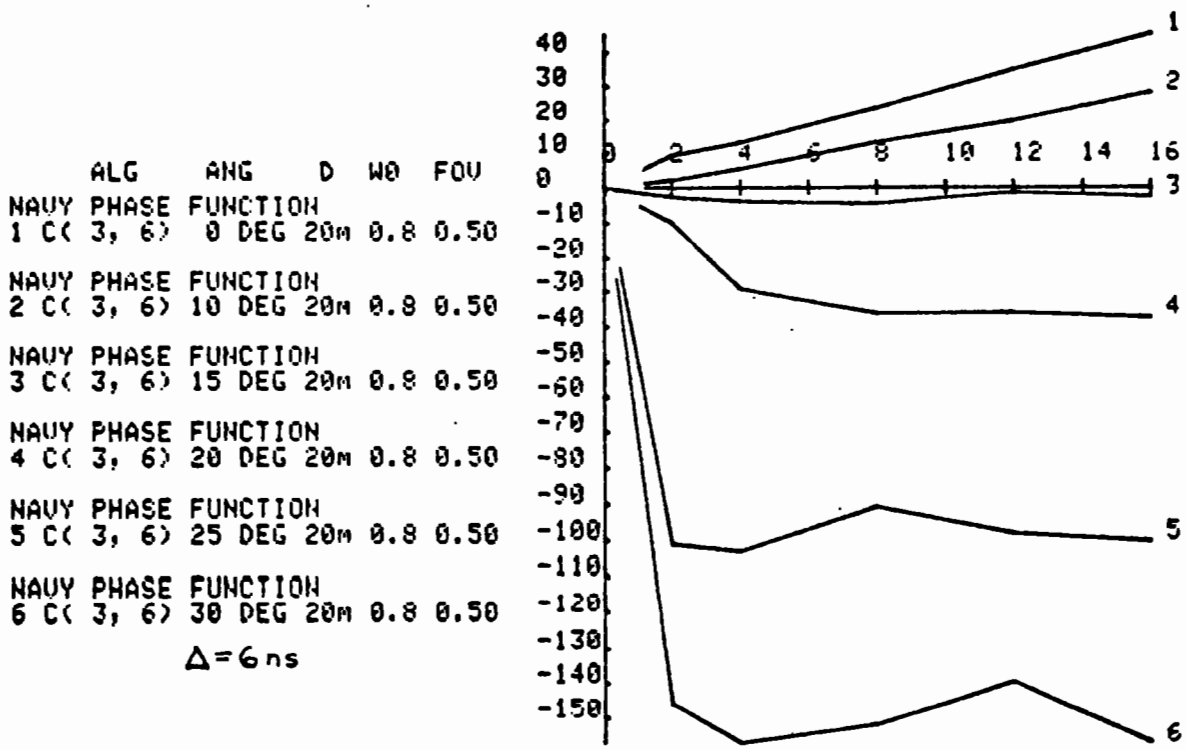

FIGURE 49. DEPTH MEASUREMENT BIAS (CM) VS OPTICAL DEPTH

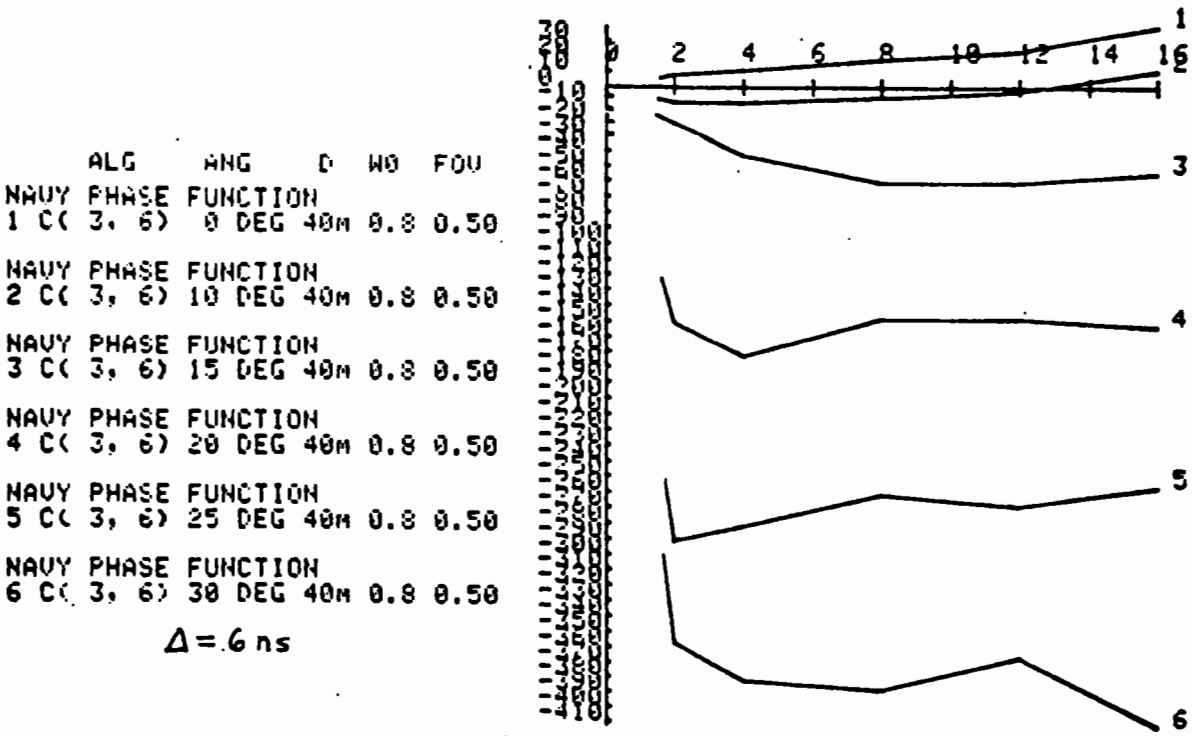

FIGURE 50. DEPTH MEASUREMENT BIAS (CM) VS OPTICAL DEPTH

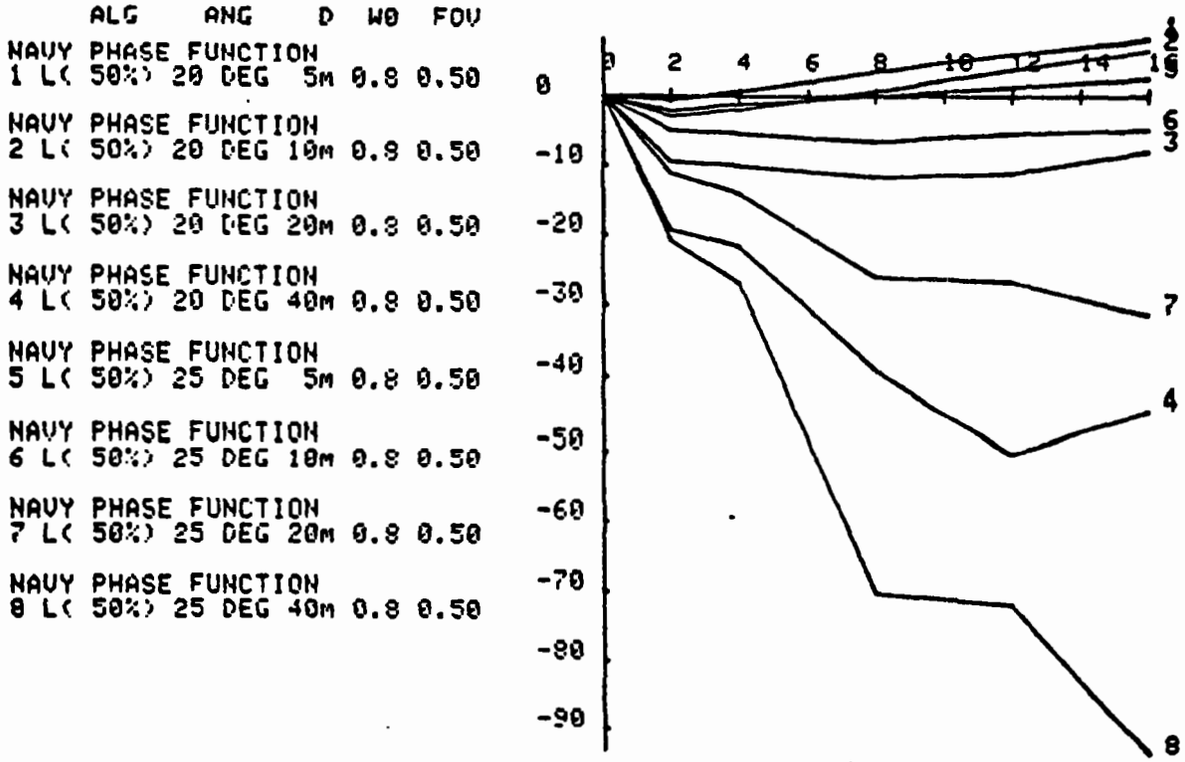

FIGURE 51. DEPTH MEASUREMENT BIAS (CM) VS OPTICAL DEPTH

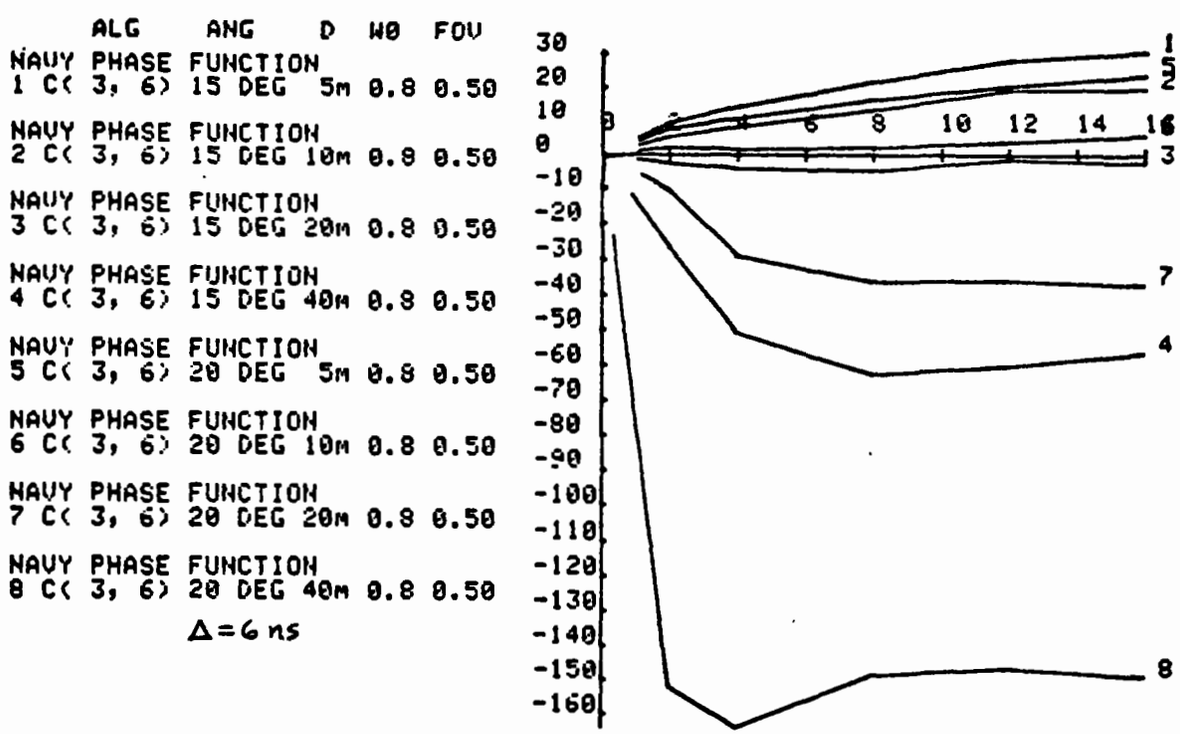

FIGURE 52. DEPTH MEASUREMENT BIAS (CM) VS OPTICAL DEPTH

detects prior to the desired time because of the existence in these cases of a plateau very close to the zero level in the internal CFD signal on which positive-going zero crossings are detected. This effect is undesirable because a small variation in return shape, receiver field of view, or a small amount of noise can cause a huge variation (and hence error) in the measured depths. This is a serious problem which would have to be dealt with if the HALS protocol were used operationally.

Since neither phase function, ω_0, nor α can be practically measured from the air, operational variables such as nadir angle must be purposefully selected to minimize the resulting bias uncertainties. This fact is illustrated in Figs. 53 and 54 for the nadir case at a depth of 20 m. The biases are large and a strong function of $\omega_0 \alpha D$. For LFTs, the uncertainty in phase function alone results in bias uncertainties of 20 cm at high optical depths. For these reasons, operation near nadir is undesirable.

The effect of receiver field of view (FOV) is seen in Figs. 55 and 56. The parameter used to define FOV in all bias plots is the radius of the spot viewed on the surface by the telescope scaled to the depth of the water (r_s/D). Previous plots have all been for $r_s/D=0.5$ ($d_s/D = 1$), which, as noted earlier, is a value that has been determined to be both appropriate and realizable. Reducing that by a factor of two is seen to have an effect on the biases of typically less than 10 cm. Larger FOVs have slightly larger biases.

The effect of the pulse location threshold fraction at a 20-m depth is demonstrated in Fig. 57. The 20% threshold yields more negative biases than the 50% threshold because detection occurs relatively earlier on the stretched bottom return pulse. The reverse is true for the 80% threshold. The variation in bias magnitude with nadir angle is larger for lower thresholds; the higher thresholds are thus preferred. They are also superior from the point of view of precision (Guenther and Thomas 1981d) because low thresholds are inherently noisier. Similar relationships apply for other depths.

For the HALS processing algorithm, the duration of the difference delay must be roughly equal to the risetime of the source pulse. Shorter values reduce the available signal amplitudes, and longer values lead to large, deep biases and large bias variation (see next section) at low depths or optical

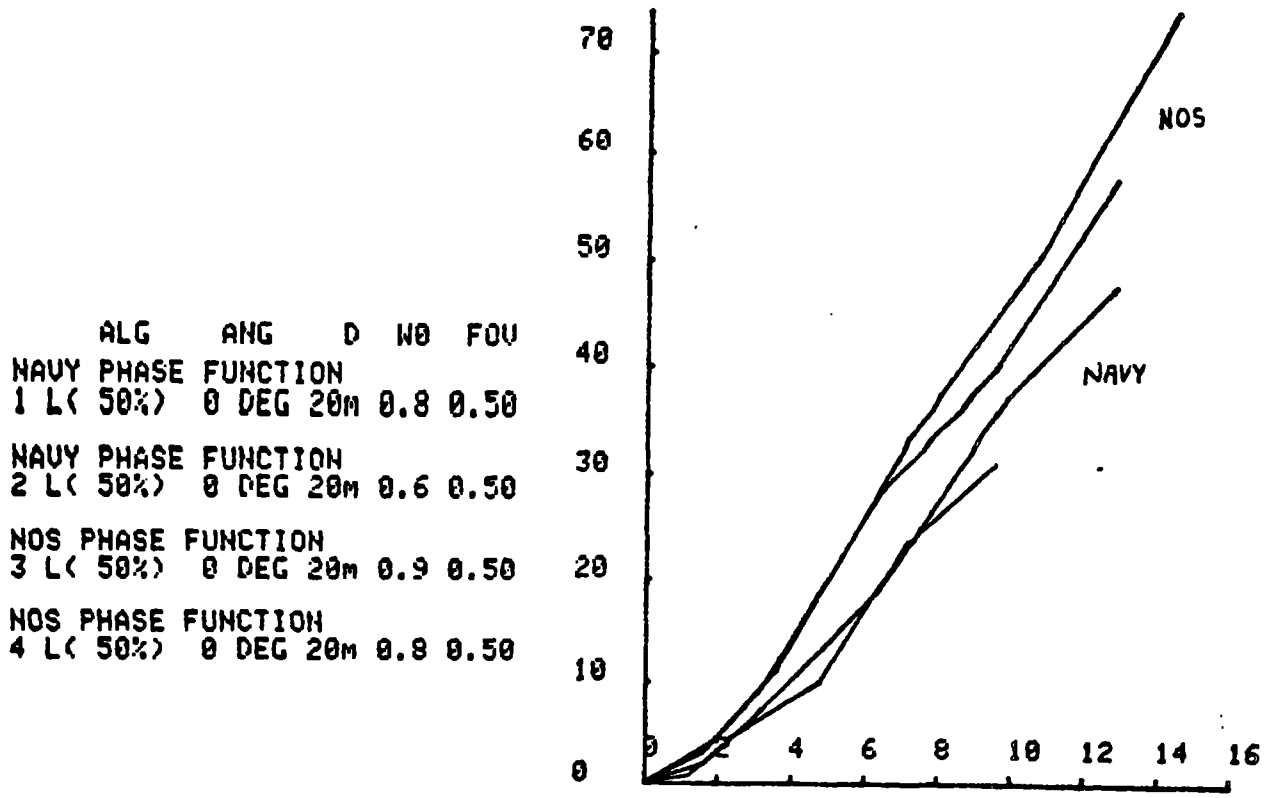

FIGURE 53. DEPTH MEASUREMENT BIAS (CM) VS SCATTERING OPTICAL DEPTH

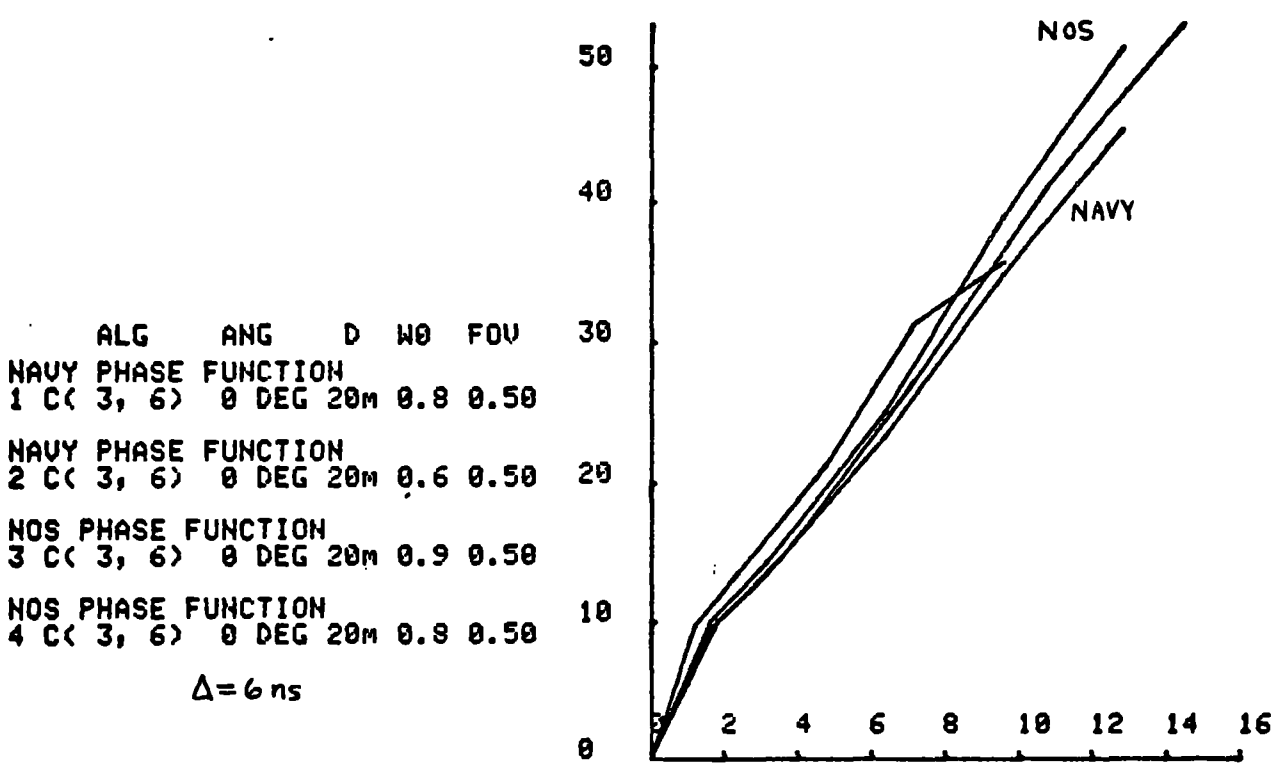

FIGURE 54. DEPTH MEASUREMENT BIAS (CM) VS SCATTERING OPTICAL DEPTH

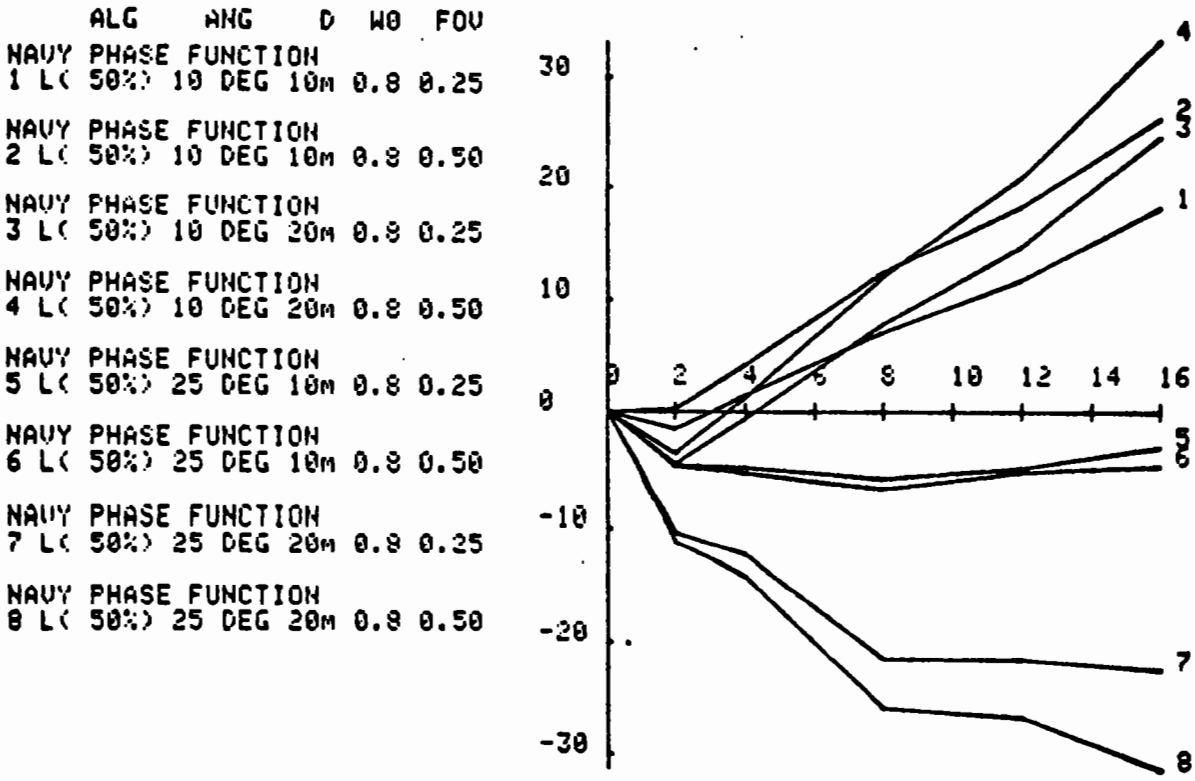

FIGURE 55. DEPTH MEASUREMENT BIAS (CM) VS OPTICAL DEPTH

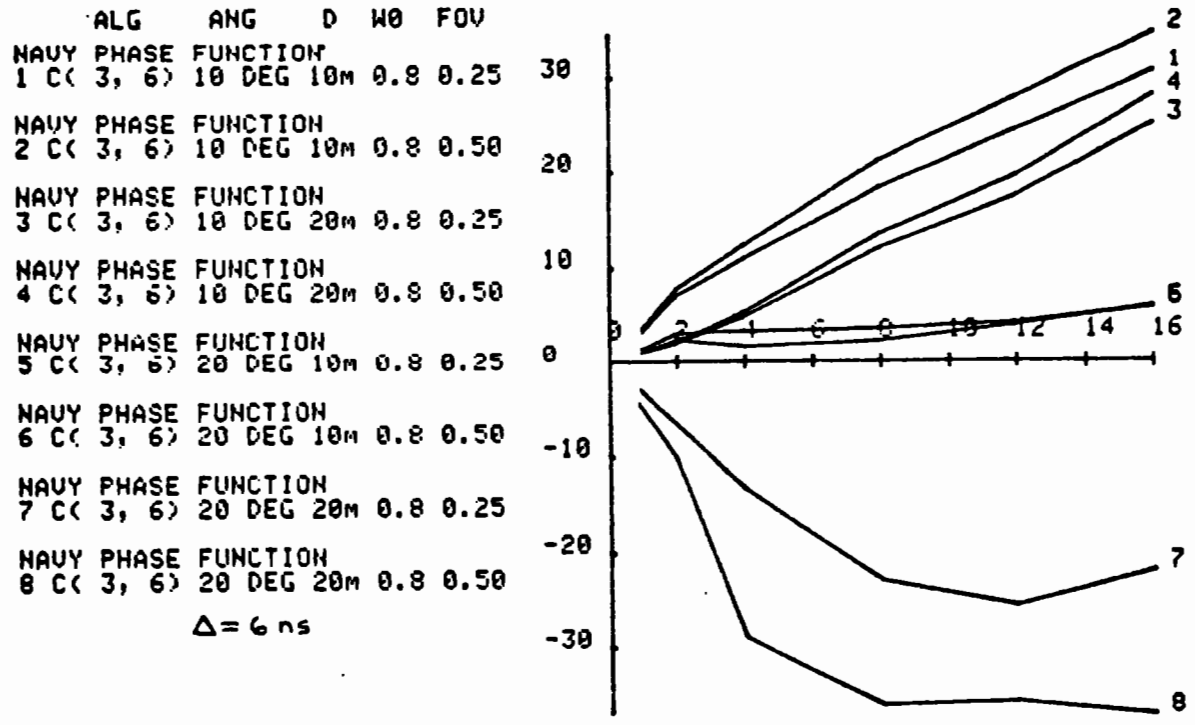

FIGURE 56. DEPTH MEASUREMENT BIAS (CM) VS OPTICAL DEPTH

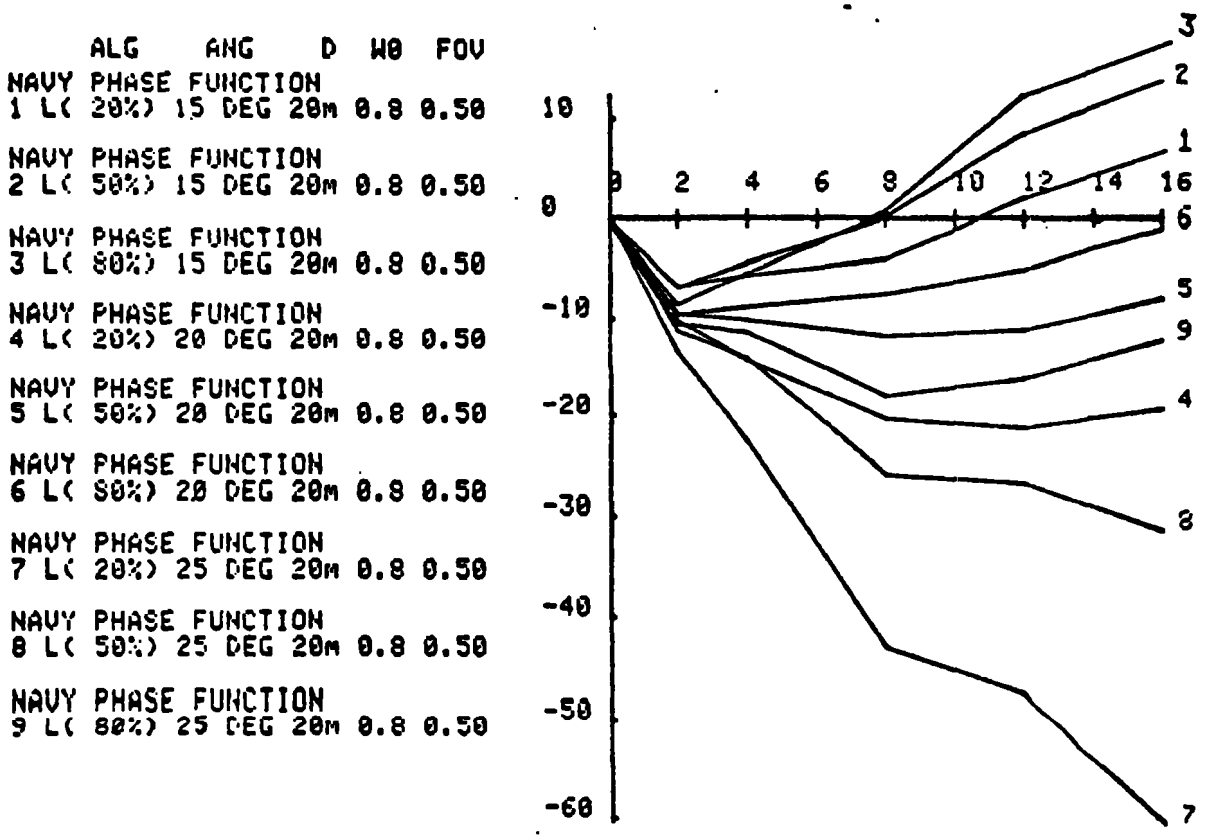

FIGURE 57. DEPTH MEASUREMENT BIAS (CM) VS OPTICAL DEPTH

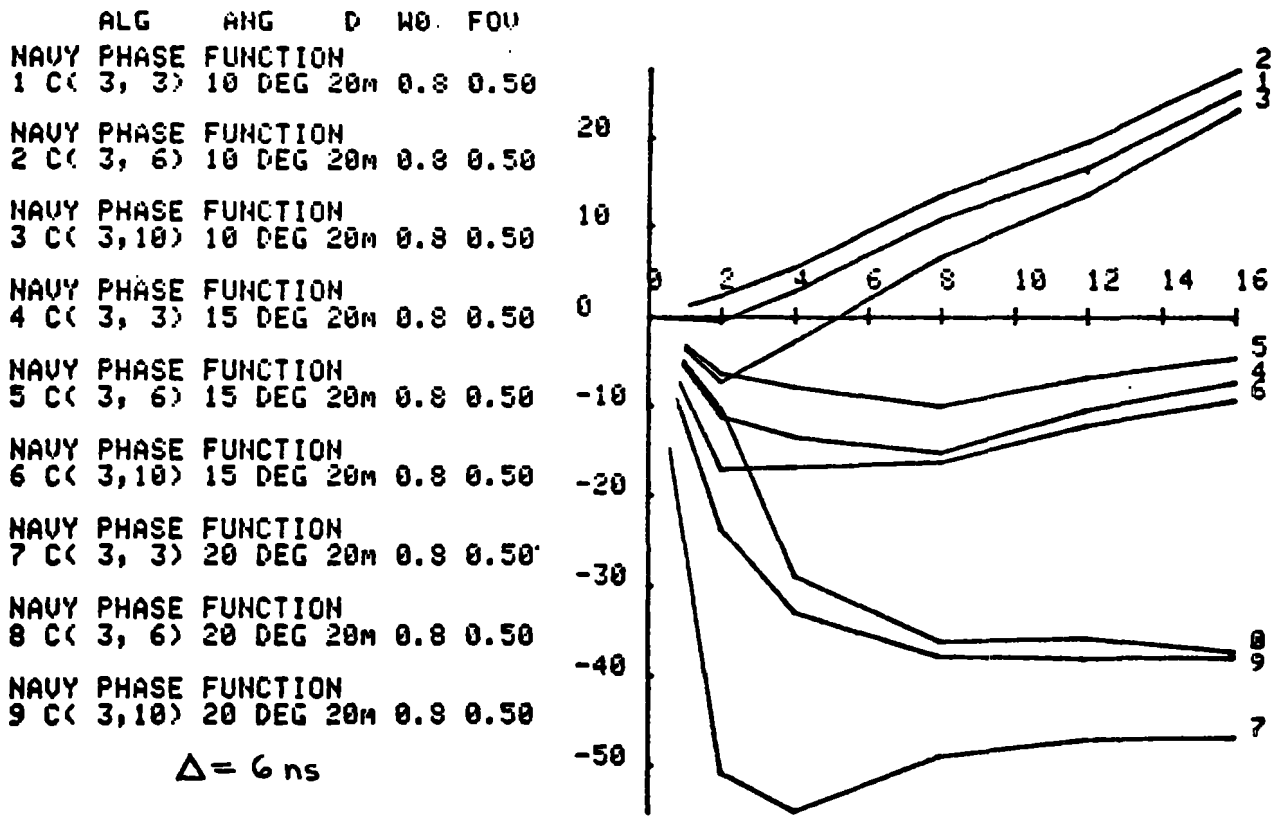

FIGURE 58. DEPTH MEASUREMENT BIAS (CM) VS OPTICAL DEPTH

depths. This is due to distortion of the resulting waveform caused by the influence of the volume backscatter signal which precedes the bottom return. All results presented here are for a difference delay of $\Delta = 6$ ns which nicely matches the 7-ns source risetime used for generating the ERFs.

The analog of LFT fraction for CFDs is the CFD time delay. It has been shown (Guenther 1982) that the ratio of the delay to the pulse risetime for log/difference/CFD processing is roughly equivalent to the threshold fraction for an LFT. The detection points are determined mainly by the delay times, however, and are not as sensitive to pulse shape as those for fractional thresholds. As seen in Fig. 58, the effect of the CFD delay on the biases is small, because the detection points shift on the bottom returns by an amount nearly equal to those on the surface returns. The effect of the delay on biases could have been larger, however, were it not for competing effects associated with the volume backscatter slope and the difference operation.

Log/difference/CFD processing has a disadvantage in that there is an additional degree of freedom in the bias dependency -- the so-called Pm/B ratio which is a measure (in linear space) of the peak signal-to-background ratio. Figure 59 details the effect of P_m/B on biases for difference and CFD delays of 6 ns and typical P_m/B values of 1, 3, and 10. Note that if P_m/B is not specified in the bias correction procedure, an additional ±10 cm uncertainty will result. This effect is generally larger than the effect of varying CFD delays. It will be seen shortly that this added error component is unacceptably large if the total bias uncertainty is to be limited to ±15 cm, and that for this type of processing, P_m/B will need to be estimated for each return.

Bias curves for "typical" operating parameters for a 50% LFT are seen in Figs. 60 - 62. It can be seen in comparison with earlier figures that selection of the appropriate range of nadir angles (20° - 25° in this case) can significantly reduce the bias variation with optical and physical depth. To depths of 20 m, the residual variations are primarily due to phase function and single-scattering albedo. In the 20° - 25° range, the 5 - 20-m biases are seen to be limited to ±20 cm. Biases for greater depths become increasingly shallow.

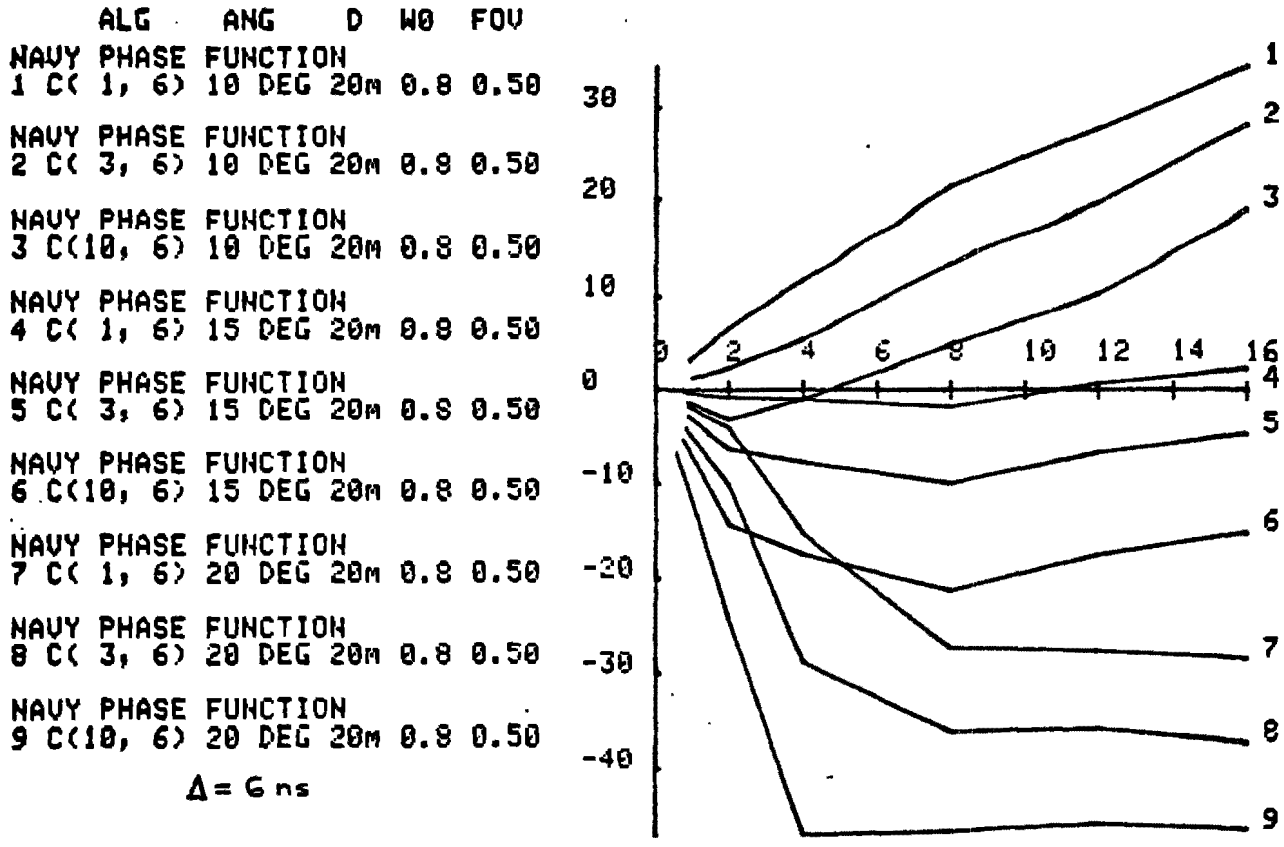

FIGURE 59. DEPTH MEASUREMENT BIAS (CM) VS OPTICAL DEPTH

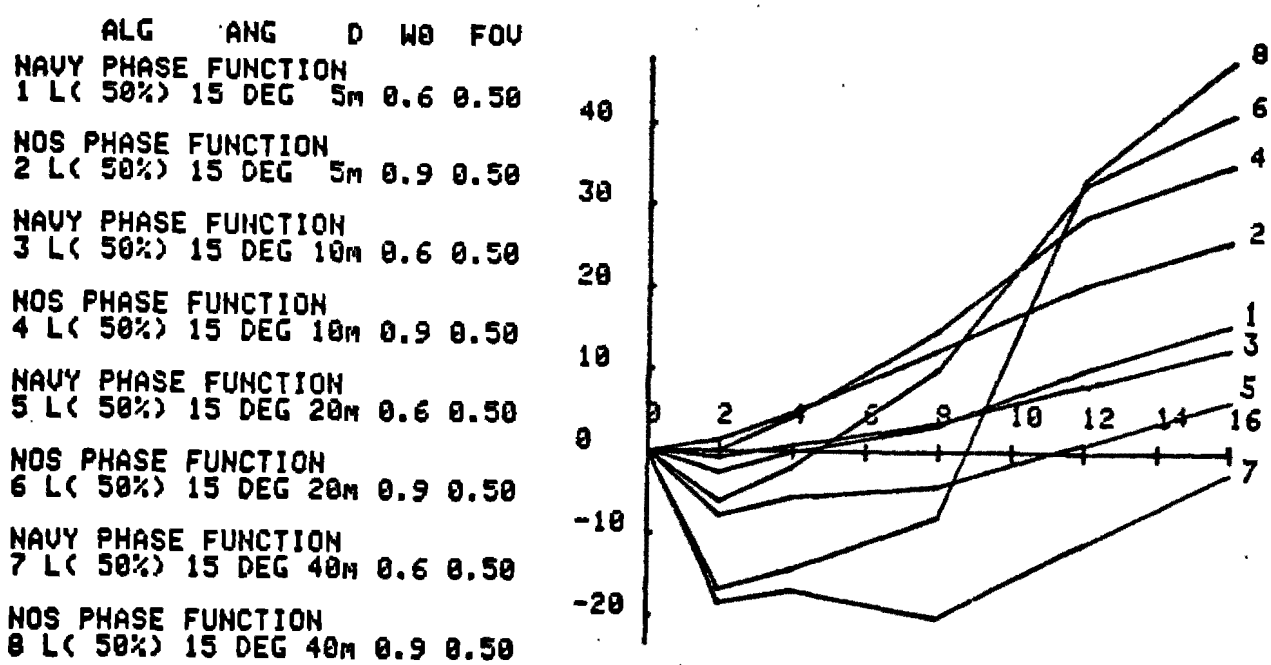

FIGURE 60. DEPTH MEASUREMENT BIAS (CM) VS OPTICAL DEPTH

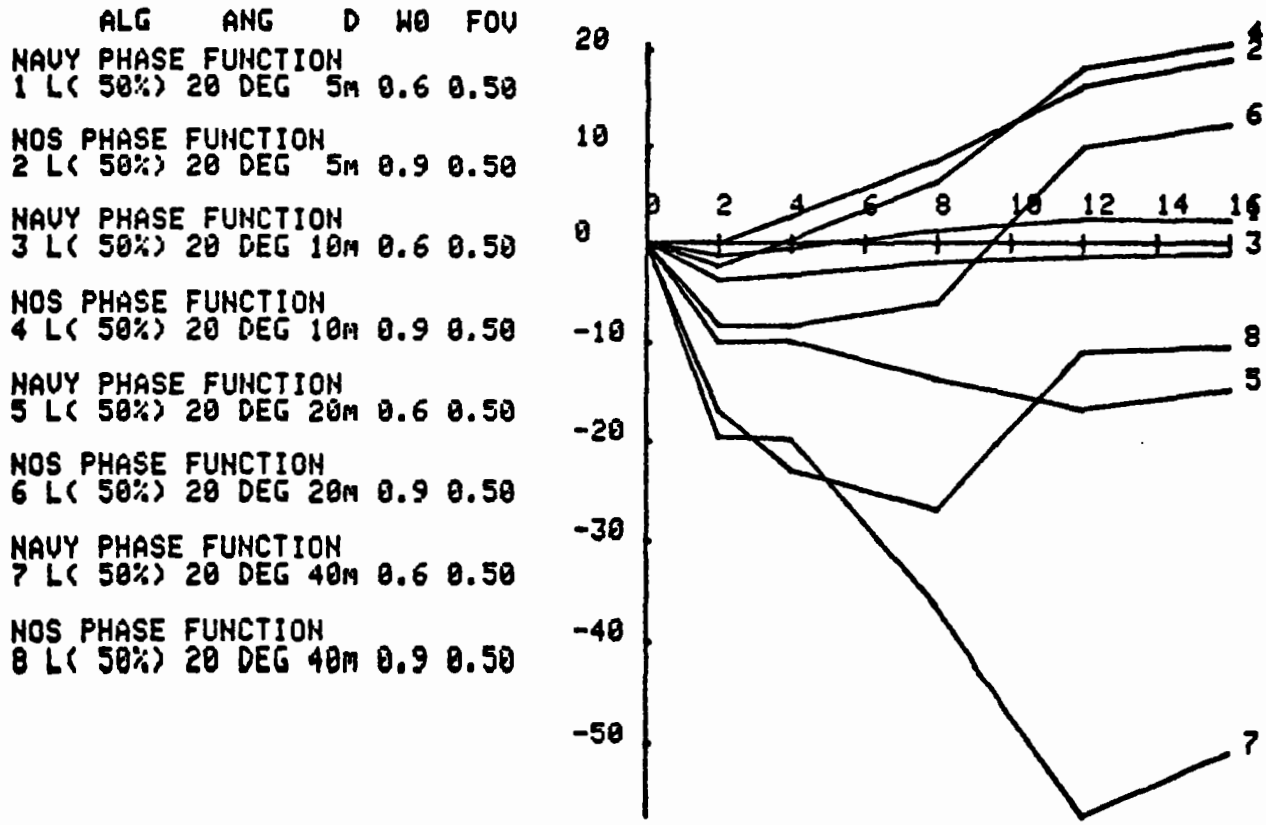

FIGURE 61. DEPTH MEASUREMENT BIAS (CM) VS OPTICAL DEPTH

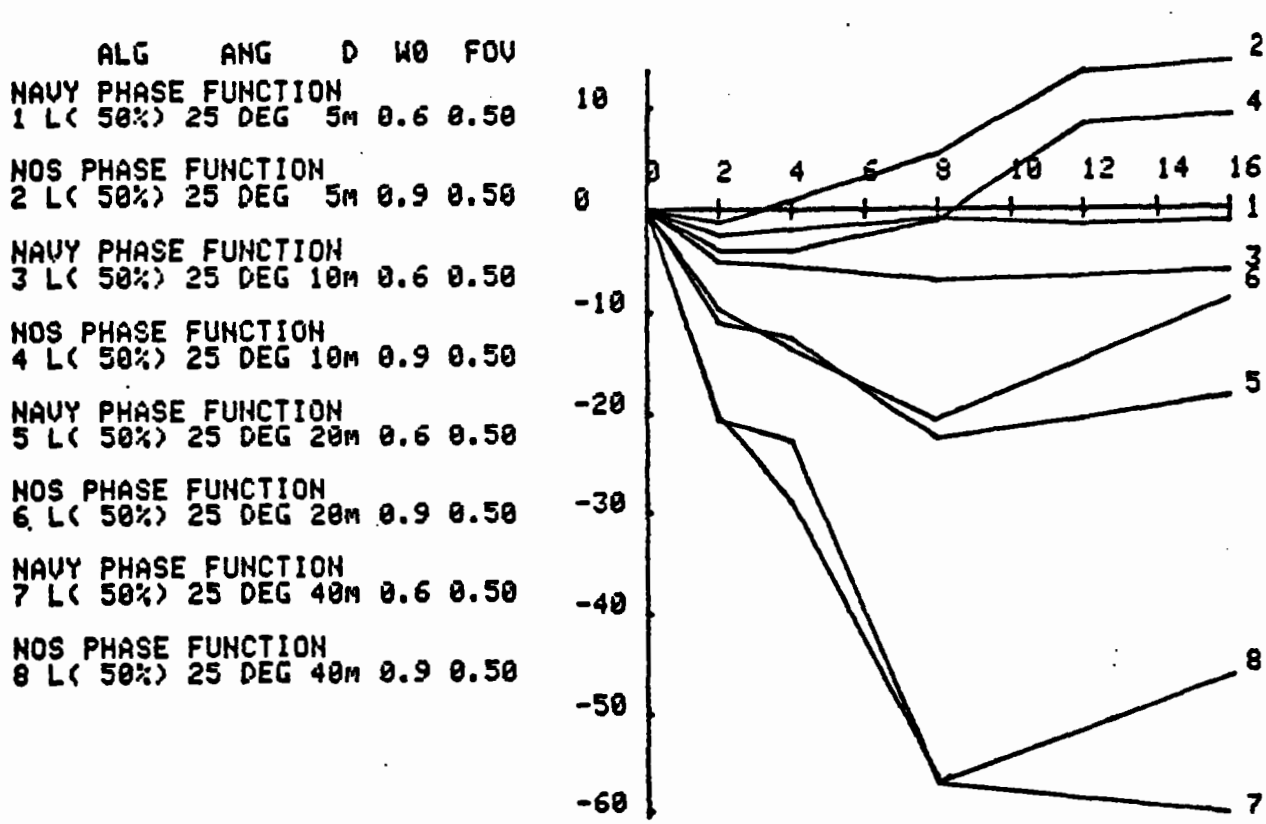

FIGURE 62. DEPTH MEASUREMENT BIAS (CM) VS OPTICAL DEPTH

Biases for a range of "typical" operating conditions for HALS log/difference/CFD processing are seen in Figs. 63 and 64 for the two phase functions. The overall ranges of biases are larger than for a 50% LFT, and are larger even for single P_m/B values. The 15° nadir angle which balances the bias range about zero is significantly smaller than that for LFTs (20° - 25°).

5.4 Bias Variation

For bias correction purposes, predicted biases can be utilized only to the extent that the driving independent parameters are known. During flight operations, those parameters which are known or can be reasonably estimated are nadir angle, water depth, processing protocol, receiver field of view, and, if necessary, peak signal-to-background ratio. Water optical parameters which are unknown and difficult to estimate in real time from lidar returns are phase function and scattering optical depth. The critical question is to what accuracy the biases can be predicted without the latter information. As will now be seen, detailed knowledge of water optical properties is not necessary for satisfactory bias correction accuracy if the scanner nadir angle is appropriately limited to a value which produces minimum bias variation for unknown conditions.

For various combinations of known parameters, the <u>bounding</u> bias predictions, based on total uncertainty in phase function and scattering optical depth, have been extracted from the data base. For this procedure, ω_0 values of 0.6 and 0.8 were associated with the NAVY phase function, and 0.8 and 0.9 with the NOS. The optical depth was considered unknown over the range from 2 to 16. For fixed values of nadir angle and depth, the mean values of the bounding bias pairs and the variations from these means to the bounding values have been calculated.

The means of the bounding bias pairs or "mean extrema" biases are the optimum bias predictors from the point of view that they minimize the worst-case bias prediction errors over all unknown water clarity conditions. They are neither the average nor the most probable biases. The variations from the

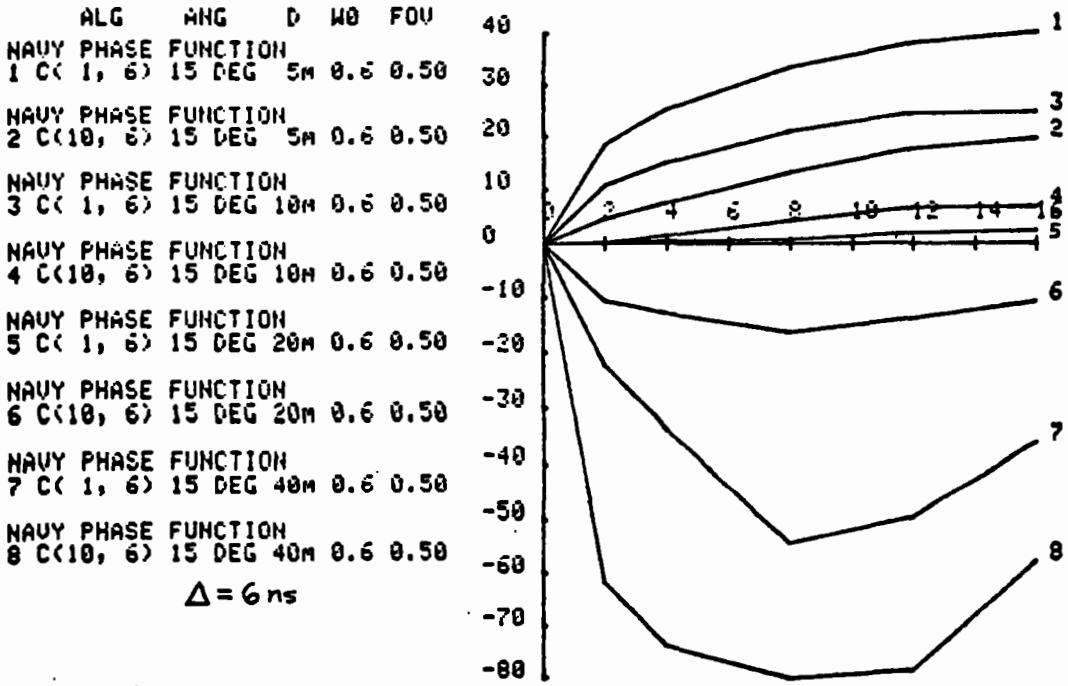

FIGURE 63. DEPTH MEASUREMENT BIAS (CM) VS OPTICAL DEPTH

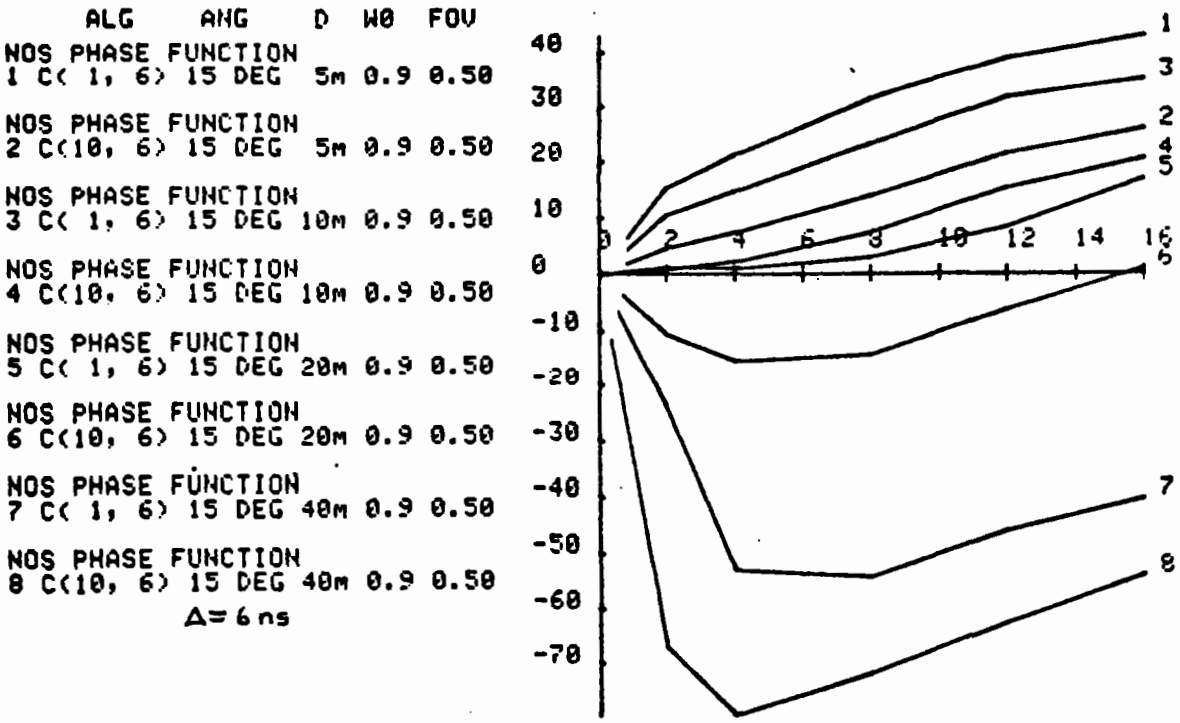

FIGURE 64. DEPTH MEASUREMENT BIAS (CM) VS OPTICAL DEPTH

extrema means to the extrema, the so-called "half-ranges," are those worst-case errors. In other words, if the reported mean of the bounding biases for a given nadir angle and depth is used as a "passive" bias corrector, the error in the resulting depth estimate due to the effect of unknown water clarity parameters should never be larger than the reported variation or half-range. If these bias variations can be constrained to acceptable bounds by the selection of appropriate ranges of operating variables, then precalculated mean biases can be applied to measured depths as correctors, and water clarity parameters need not be estimated from field data. If the bias variations are too large, however, "active" bias correctors calculated from real-time, pulse-to-pulse estimates of water optical properties will be necessary. It would be beneficial to avoid this considerably more taxing procedure, if possible.

The magnitudes and functionalities of the bias extrema means and half-ranges about the means for various LFT and CFD cases are presented in Figs. 65 - 76. The bias variations or half-ranges for a 50% LFT are plotted as a function of nadir angle in Fig. 65 for depths from 5 to 40 m and for a FOV (R/D) of 0.5. The main feature of this data is the existense of minima in the bias variation curves. These minima occur as the bias trends switch from being lengthened by multiple scattering to being shortened by undercutting. The resulting mean biases for these bias variation minima are thus generally fairly small. At a 20-m depth the minimum for this case is at a nadir angle of 23°, while at 40 m the minimum is at 20°. For depths of 5 m and 10 m the minima are beyond 30°.

The critical issue is the magnitude of the bias variation with unknown water parameters. In a total error budget of ± 30 cm, only about 15 cm can be allotted to this error source. This is noted on the figures by a dashed line. It can be seen in Fig. 65 that bias variations for the old 20-m depth requirement are less than 15 cm for nadir angles between 20° and 26°. For 5-m and 10-m depths, bias variations are under 15 cm beyond angles of 13° and 19°, respectively. At 40 m, the minimum variation is 21 cm, and, by interpolation, the 30-m minimum variation at 22° is about 17 cm, which slightly exceeds the desired (but somewhat arbitrarily selected) value. For this processing scheme, 22° is thus the desired operating angle. Uncontrolled aircraft roll and pitch will cause larger errors which would best be suppressed by using a

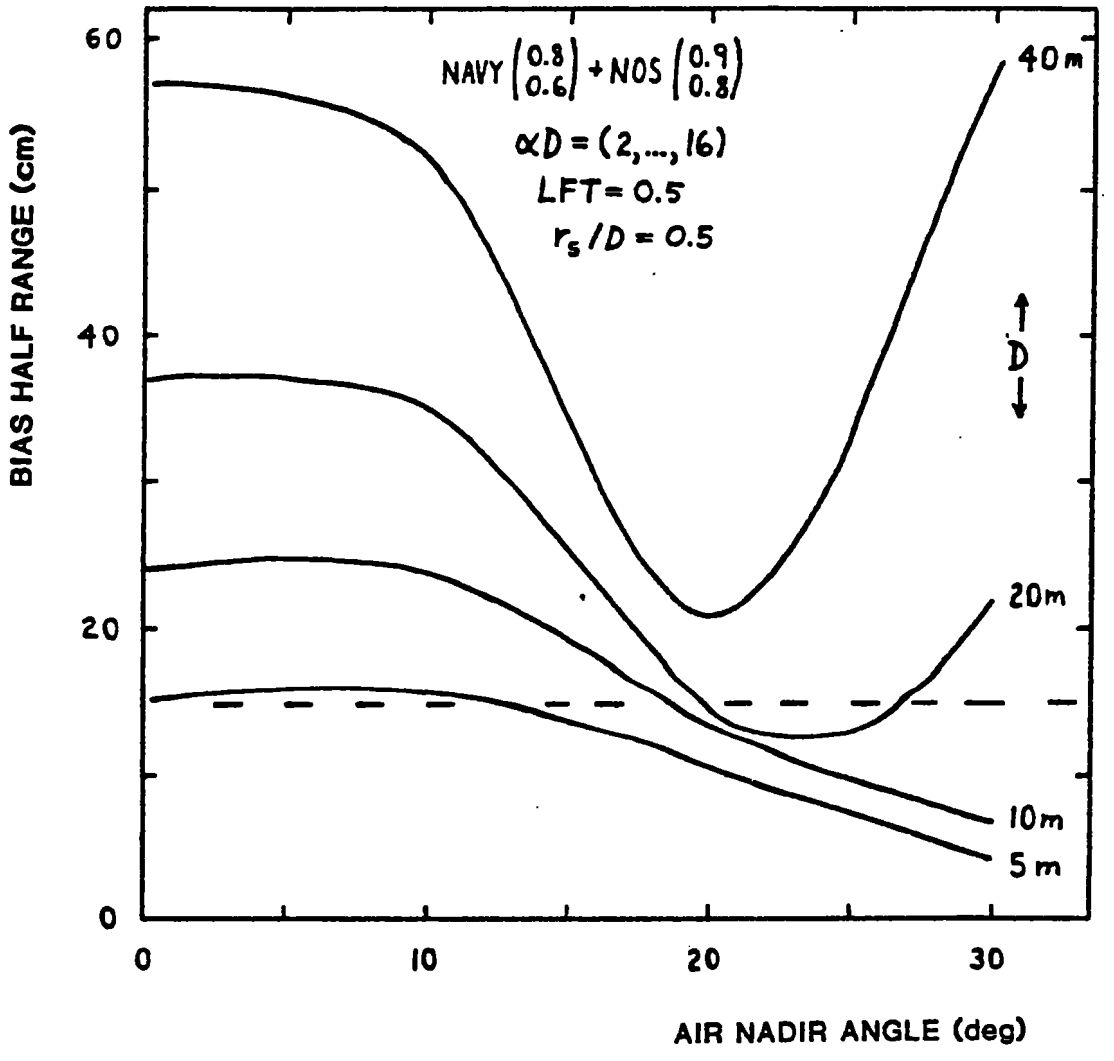

FIGURE 65. BIAS VARIATION FOR LFT 50%

gyro-stabilized scanning mirror. Operation at suboptimal angles will lead to errors in bias prediction which greatly exceed international standards. At nadir, for example, the bias variation for a 50% LFT is seen to be ±37 cm at a 20-m depth and ±47 cm at 30 m. The mean extrema biases for the 50% LFT case are plotted versus depth and nadir angle, respectively, in Figs. 66 and 67.

Because the range of unknown optical depths from 2 to 16 is quite large, it was felt that even marginally increased knowledge of that parameter might reduce the bias variations. To that end, the same procedure was repeated for the case where αD is known (or assumed) to be either less than or greater than 8. The resulting half-ranges are seen in Fig. 68 for a 20-m depth. The resulting minimum half-range for $2 < \alpha D < 8$ is quite a bit smaller, but the half-range for $8 < \alpha D < 16$ is virtually the same as for $2 < \alpha D < 16$. For the high αD case, the angular range for which the bias variation is less than 15 cm expands only slightly to 19° - 28°. This means that most of the total variation occurs at high αDs, and that much higher resolution in an αD estimate would be required to significantly reduce the bias variation.

Figures 69 - 71 contain bias half-range and mean extrema biases for the case of a 20% LFT. The half-range curves are similar to their 50% LFT counterparts except that the half-range minima have been shifted to slightly lower nadir angles. For a 20-m depth, the minimum is at 20°, and for a 15-cm bias uncertainty, the nadir angle range is 17° to 23°. The 40-m minimum is 20 cm at 17°. By interpolation, the 30-m minimum is about 16 cm at 19.5°. The reason for the shift of the minimum to lower angles is that these mean extrema biases are more negative for given depths and nadir angles than those for the higher threshold. The crossover point thus occurs at lower nadir angles. This case is less attractive than for the 50% LFT for an unrelated reason: the resulting random error component is much larger (Guenther and Thomas 1981d).

The character of the bias variations and mean extrema biases for HALS processing is less definitive than for the LFT case. First, the sensitivity to the lower end of the optical depth range is much greater. Because water clarity tends to decrease as depth decreases, it is felt that a lower limit of 2 is appropriate for practical use. If that range were expanded to (0 - 16)

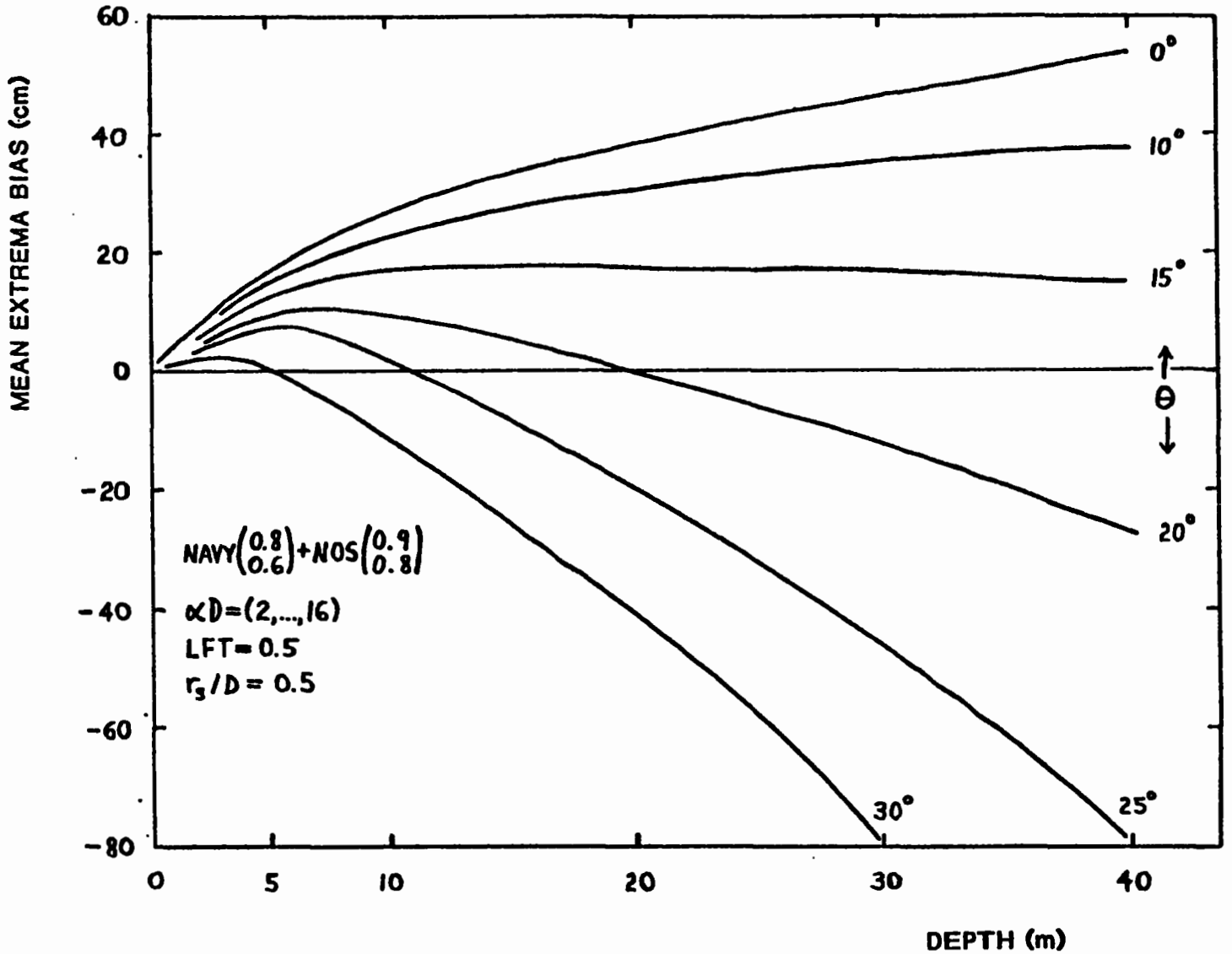

FIGURE 66. MEAN EXTREMA BIASES FOR LFT 50%

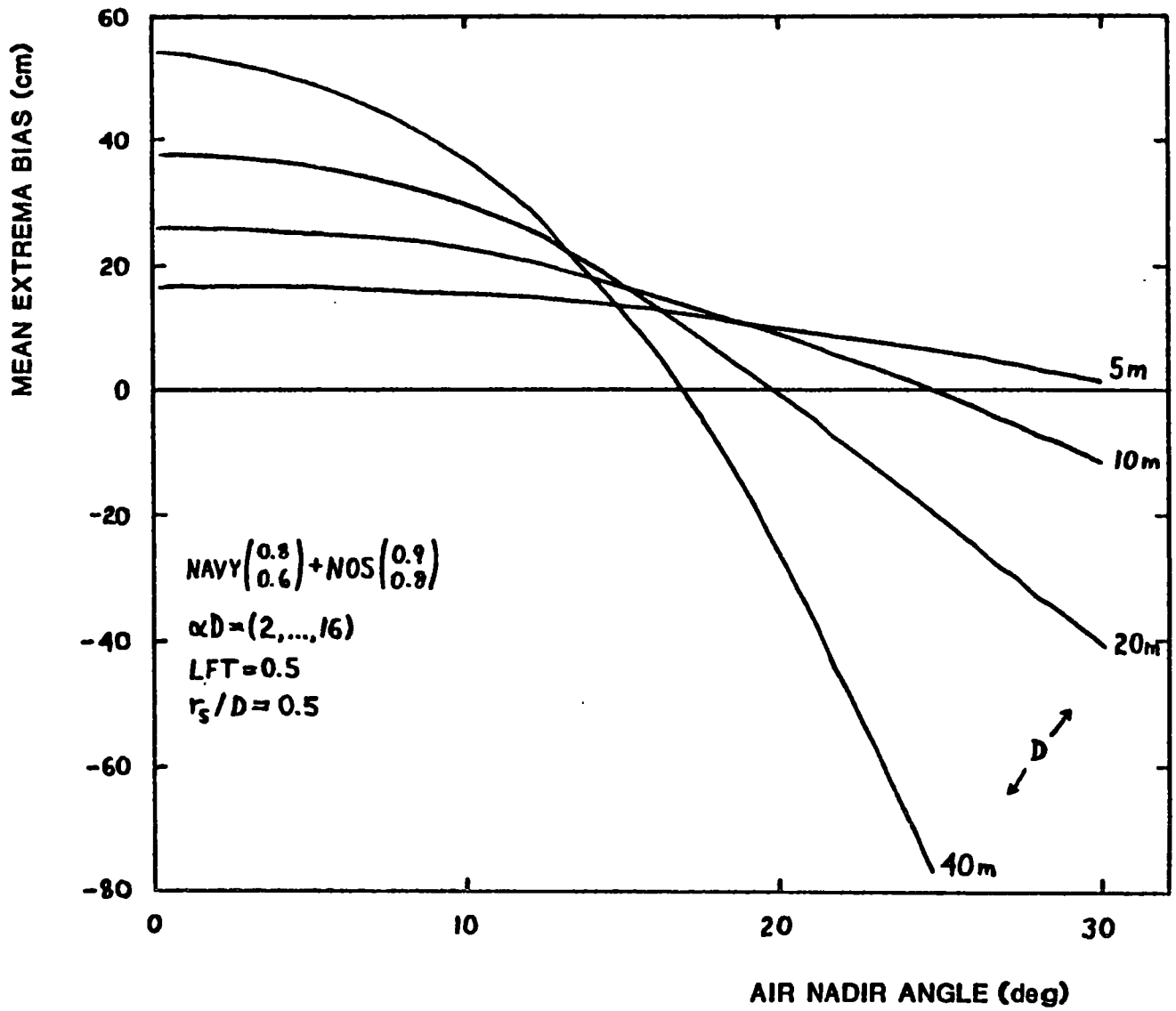

FIGURE 67. MEAN EXTREMA BIASES FOR LFT 50%

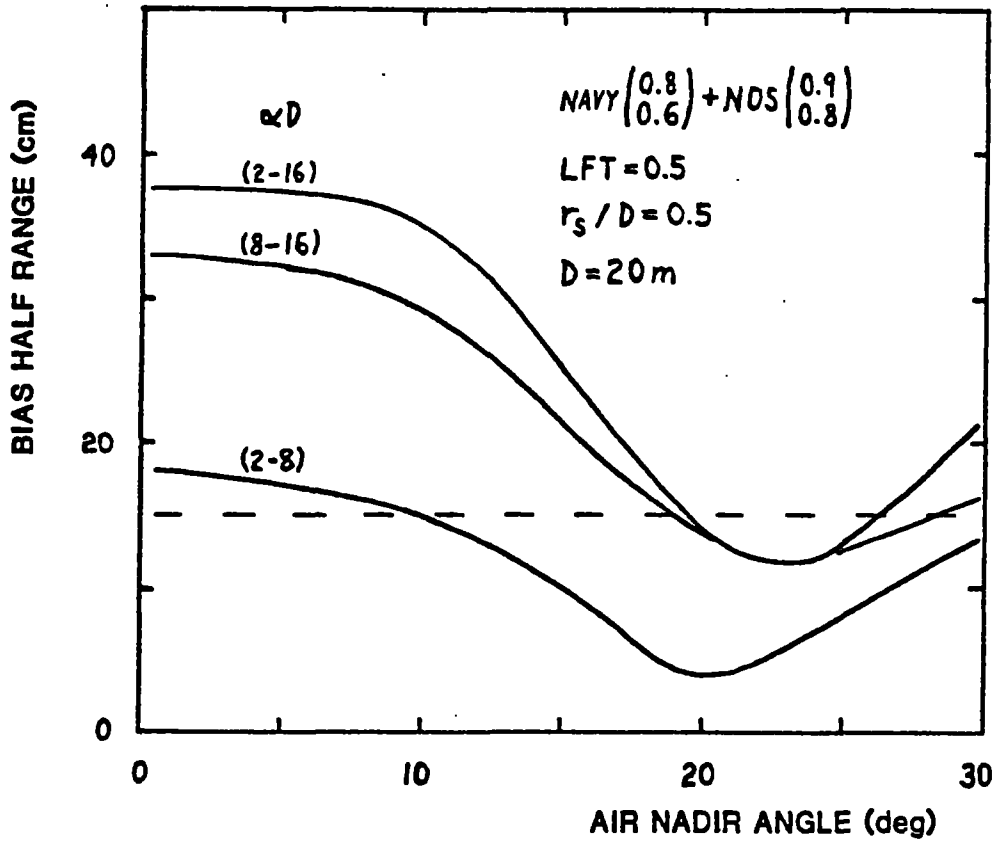

FIGURE 68. BIAS VARIATION FOR SPLIT OPTICAL DEPTH RANGE

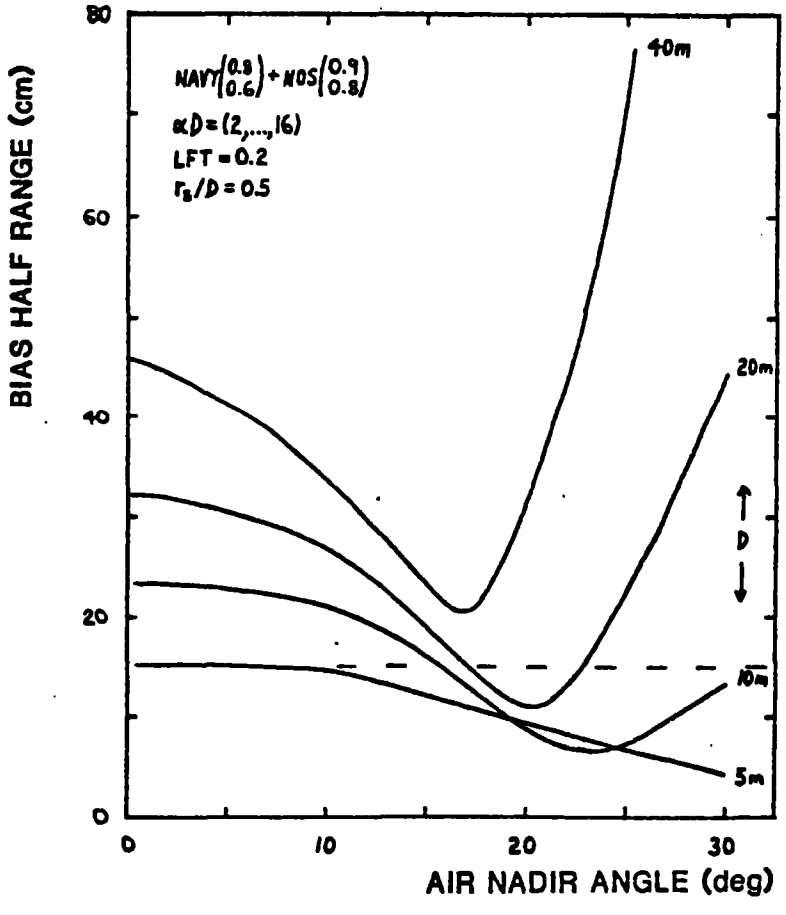

FIGURE 69. BIAS VARIATION FOR LFT 20%

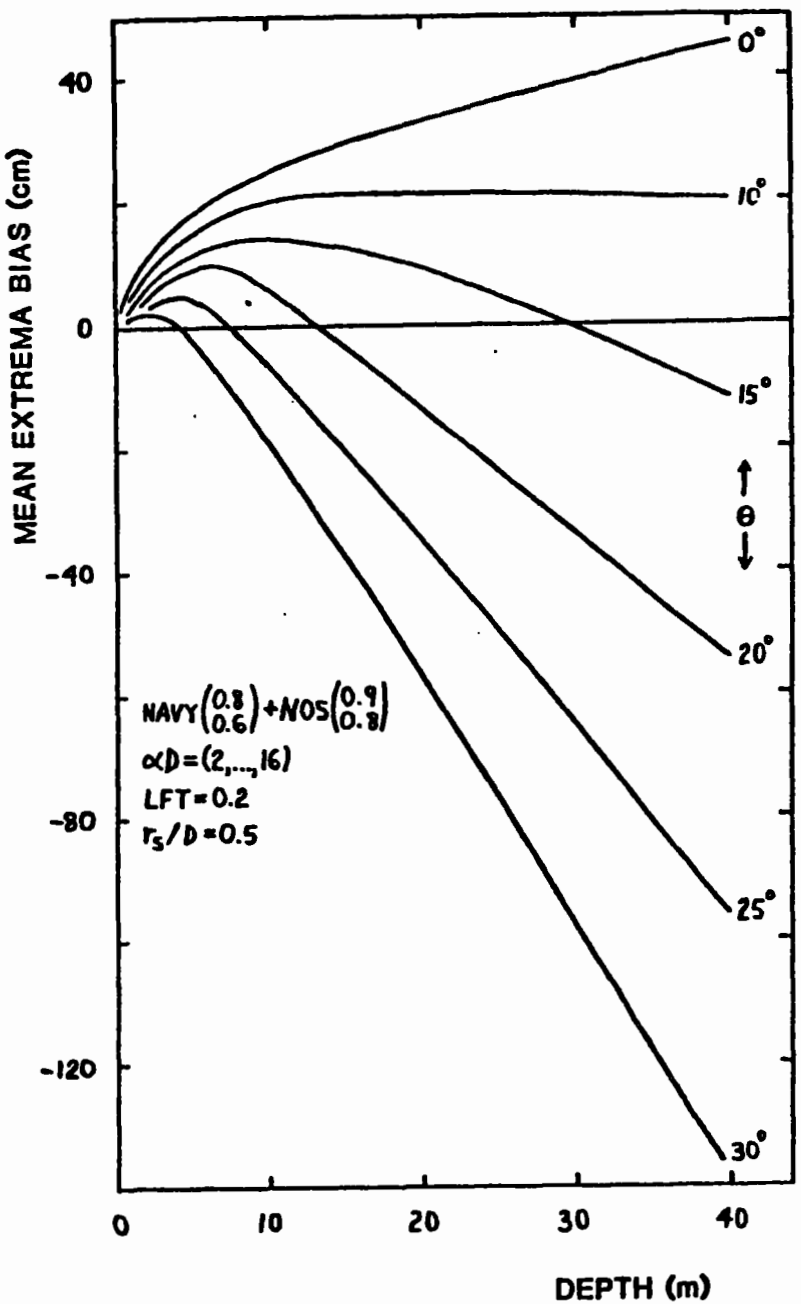

FIGURE 70. MEAN EXTREMA BIASES FOR LFT 20%

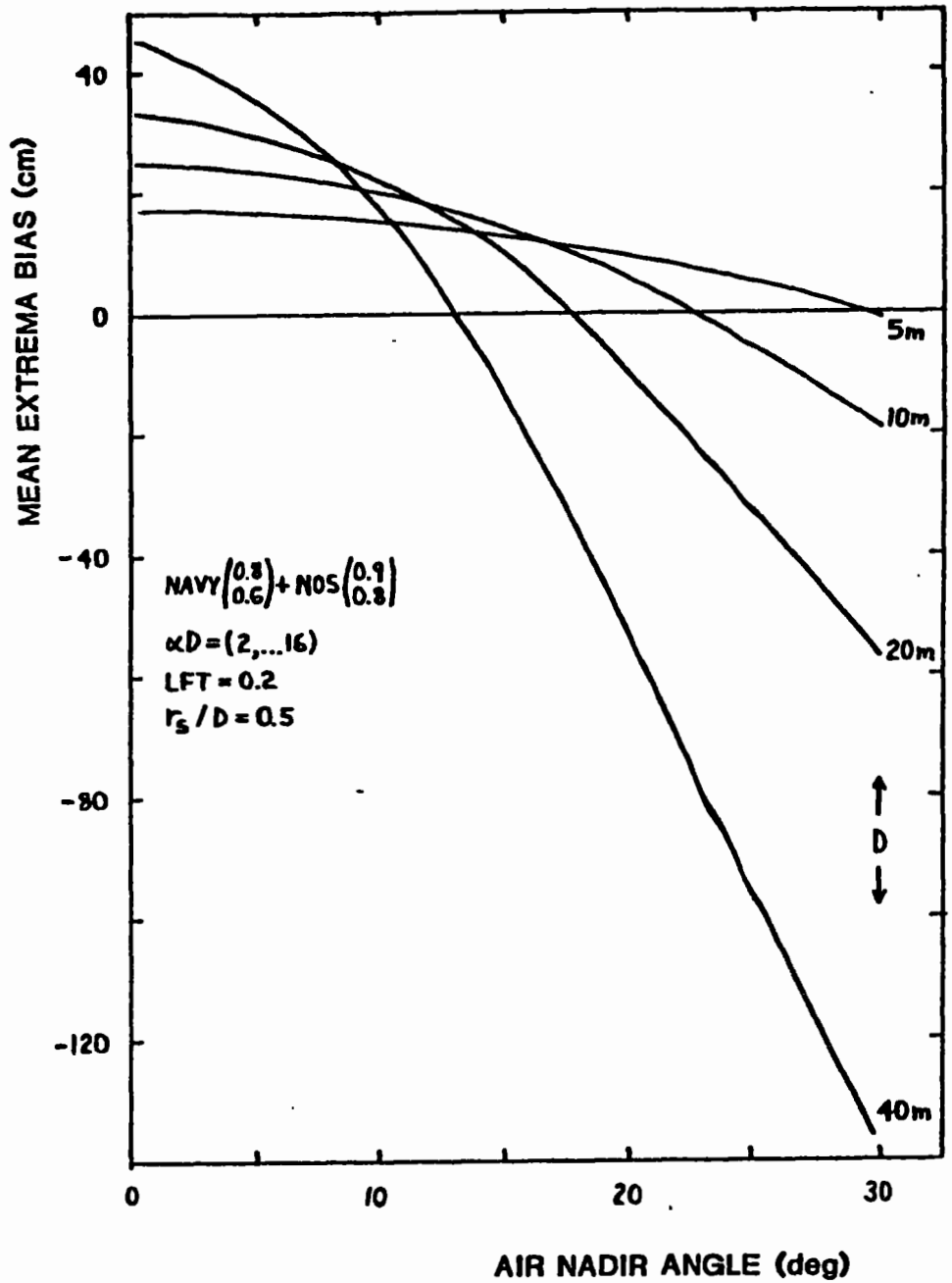

FIGURE 71. MEAN EXTREMA BIASES FOR LFT 20%

instead of (2 - 16), however, significant differences would result due to the frequently large biases evidenced even for $\alpha D=2$. Secondly, because of the previously mentioned plateau in the CFD signal for cases with large nadir angles, low optical depths, and high physical depths (very clean water), the biases will depend heavily on the exact pulse location logic in a real, noisy system. The early detections reported here for the noise-free, idealized case lead to large but fairly constant negative biases across a wide range of optical depths. Slightly altered (more sophisticated) logic could result in much later detections and increased bias dependence on optical depth (and hence increased bias variations and decreased mean extrema biases). Even though the bias variations with optical depth for the idealized case may be relatively low for large biases, operation under such conditions would be undesirable due to sensitivity of the exact bias values to uncertainties in nadir angle, random errors in the simulation results, and random noise in the actual signals. Because of these problems, results for the offending cases, which luckily fall outside the operational region of interest, will not be presented.

Figure 72 shows the bias variation for HALS processing with a difference delay and a CFD delay of 6 ns for a range of (unknown) peak signal-to-background ratios (P_m/B) from 1 to 10. The minimum half-range at a 20-m depth for this case is 17 cm, and the combined minimum over the 5 - 30 m depth range is 20 cm at 14.5°. The reason for the increase in the minimum bias variation over the LFT cases is the added degree of freedom represented by P_m/B. Because the minimum value is unsatisfactorily large, specific information on P_m/B will be required. Bias half-ranges and mean extrema biases for P_m/B fixed at values of 1 and 10 are plotted in Figs. 73 - 74 and 75 - 76. Although the half-ranges are quite similar, the mean extrema biases differ by about 10 cm. The 20-m half-range minima are 9 cm and occur at angles of 14° - 15°. At a 20-m depth, the 15-cm level is not exceeded for nadir angles in the range 14.5° ± 4°. These angles are smaller than those for the LFT cases. The mean extrema biases for the given conditions are more negative than for LFTs, and they change more rapidly with varying nadir angle. The most constraining circumstances for minimum and maximum nadir angle (for half-ranges not to exceed ±15 cm) occur for 5-m and 30-m depths, respectively. For $P_m/B=1$, the 5-m half-ranges exceed 15 cm for angles less than 15°, while for

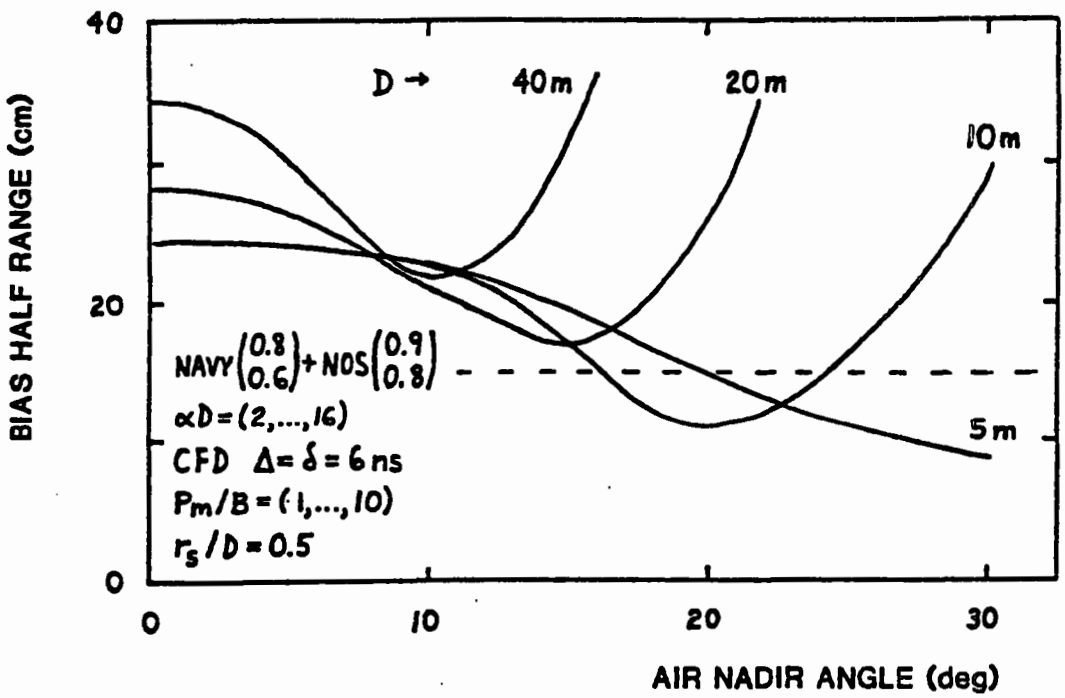

FIGURE 72. BIAS VARIATION FOR CFD (6, 6, 1-10)

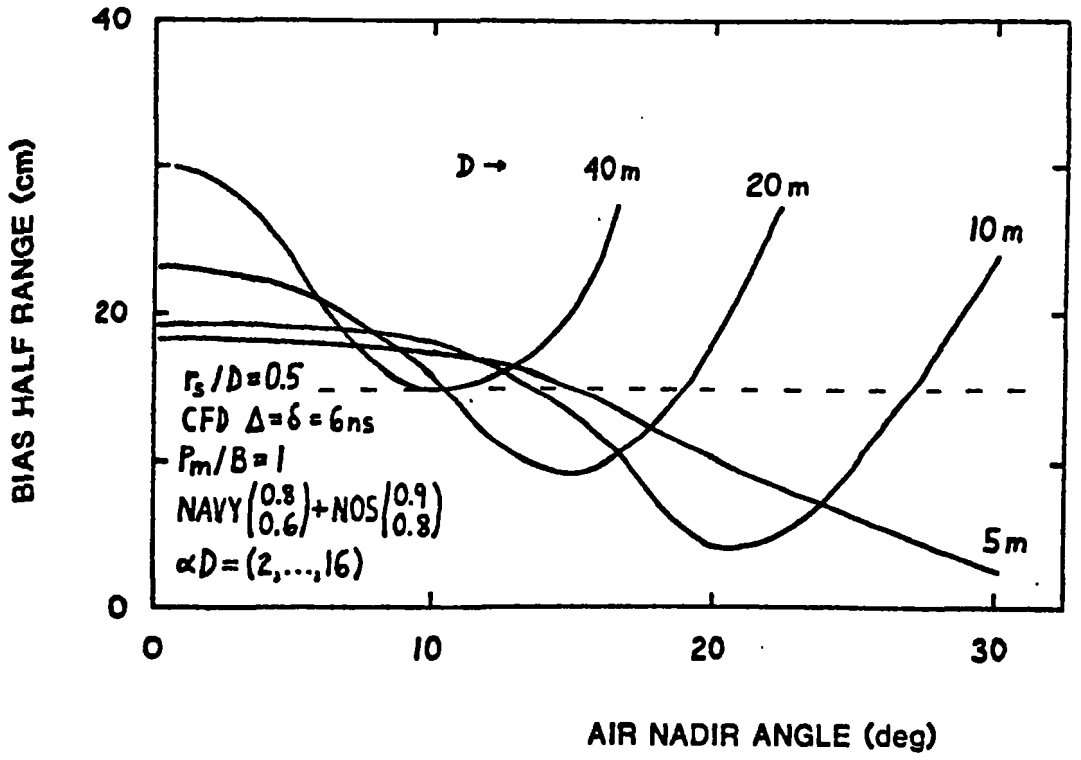

FIGURE 73. BIAS VARIATION FOR CFD (6, 6, 1)

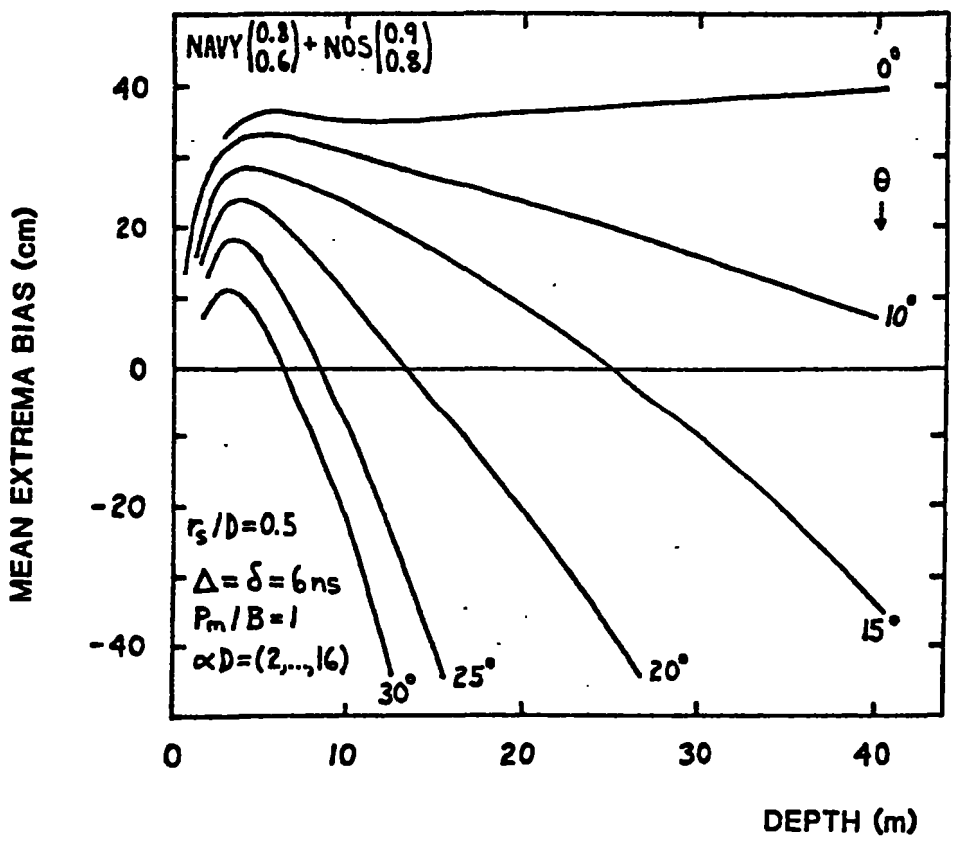

FIGURE 74. MEAN EXTREMA BIASES FOR CFD (6, 6, 1)

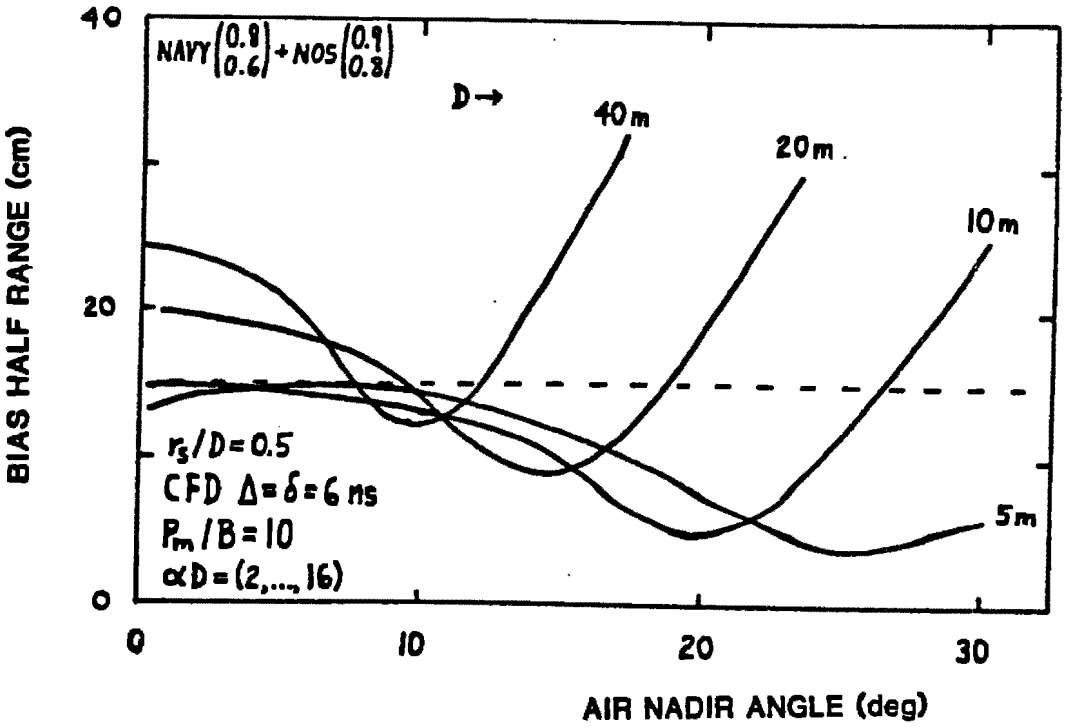

FIGURE 75. BIAS VARIATION FOR CFD (6, 6, 10)

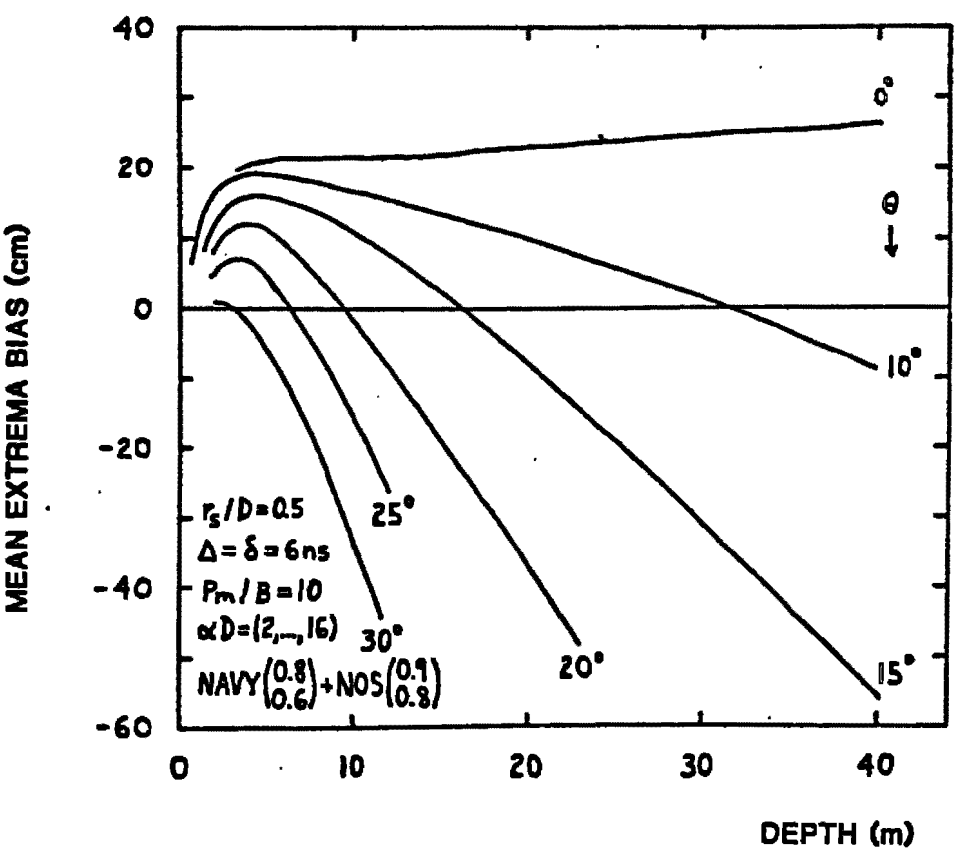

FIGURE 76. MEAN EXTREMA BIASES FOR CFD (6, 6, 10)

$P_m/B=10$, the 30-m half-ranges exceed 15 cm for angles greater than 15.5°. The desired operating angle for the HALS processing scheme is thus 15°. A gyro-stabilized scanning mirror is again highly desirable. Curves for CFD delays of 3 and 10 ns are similar due to the previously noted relative insensitivity of the biases to that parameter. As with the LFT case, splitting biases into two optical depth ranges does not provide a means of significantly improving performance, even though the functionalities are somewhat different.

5.5 Formal Bias Description

For use as bias correctors, the mean extrema biases presented in the figures can be either tabulated or fitted analytically. Smoothed biases tabulated at 5 m, 10 m, 20 m, 30 m, and 40 m can be interpolated linearly over depth and nadir angle, with very small residual errors, for nadir angles up to and including 25°. Alternately, if algebraic representations are desired, the biases can be described in the form

$$B(cm) = aD^n - bD^m(1 - \cos\theta)^k, \tag{9}$$

where B is the bias in centimeters, D is the depth in meters, and θ is the air nadir angle. The coefficients a, b, n, m, and k can be adjusted to fit the bias curves for various cases of signal processing algorithms and parameters. Table 2 presents sets of coefficients for the mean extrema bias curves shown in Figs. 66, 70, 74, and 76 along with their respective RMS of fit and maximum deviation of fit calculated for depths from 5 m - 20 m and nadir angles of 15° - 25° for LFT and 10° - 20° for CFD. The fits themselves are valid from 0° - 25° and for depths to 40 m, as well.

Table 2. Bias Fitting Coefficients

Case	Fig.#	a	b	n	m	k	RMS (cm)	max. dev. (cm)
LFT 50%	66	6.5	27.0	0.58	1.25	1.26	2.5	4.7
LFT 20%	70	8.3	21.5	0.46	1.16	0.98	1.3	2.3
HALS* $\Delta=\delta=6$ ns, $P_m/B=1$	74	32.8	37.4	0.043	1.28	1.18	2.5	5.7
HALS $\Delta=\delta=6$ ns, $P_m/B=10$	76	15.9	21.8	0.13	1.59	1.30	2.6	6.8

* $\Delta\equiv$difference delay, $\delta\equiv$CFD delay

Linear interpolation of tabulated values provides a slightly more accurate, if more cumbersome, representation of the simulation outputs, but it is possible that the inherent smoothing action of the analytic fit over all parameters may provide slightly more consistent results. Regardless of whether CFD biases are derived from tables or a formal expression, they will have to be calculated by interpolation or extrapolation from the two given values of P_m/B. As seen in Guenther (1982), the estimation should be performed linearly on the $\log(P_m/B)$.

6.0 BIAS CORRECTION

6.1 Introduction

As seen in section 5.3, the propagation-induced depth measurement biases depend functionally on the scattering optical depth. The direct or "active" application of specific bias predictions as bias correctors to field data would require sufficiently accurate measurement or estimation of the driving water optical parameter, namely, the scattering coefficient. Sufficiently dense and synoptic sea-truth measurements of the scattering coefficient cannot be economically collected over the large and diverse areas required, and it cannot be obtained from ancillary, passive remote sensing devices. The only viable alternative is thus estimation of the scattering coefficient or the scattering optical depth from quantifiable features of the returning laser waveforms.

The most straightforward and reliable parameter available from the return waveform is the volume backscatter exponential decay coefficient, k_b. It has been demonstrated by Gordon (1982) that for sufficiently large receiver FOV, the value of k_b in shallow water appears to be roughly equal to the value of the diffuse attenuation coefficient, K, of the water. Also for the large field-of-view case, Phillips and Koerber (1984) argue that k_b is equal to the absorption coefficient, a value slightly smaller than K. For limited fields of view, the backscatter decay coefficient is somewhat larger than for the large-FOV case. For a practical system FOV, this increases the coefficient to a value again very near K. In summation, the value of K, or something very near it, can be estimated from individual lidar returns.

The problem is that there is no sufficiently accurate way of obtaining an estimate of the required scattering coefficient, s, from K. From a plot of s versus K data for natural waters, as seen in Fig. 77 (accumulated from a variety of sources), it can be seen that the scatter in the functional propensity is too large. At $K=0.15\ m^{-1}$, for example, the values of s range over a factor of 9, which is far too large to be of use. Similarly, if one notes the propensity for $\omega_0 \cong 0.8$ in many coastal waters, one could make a rough estimate of α from the K/α relationship in section 4. One could then further

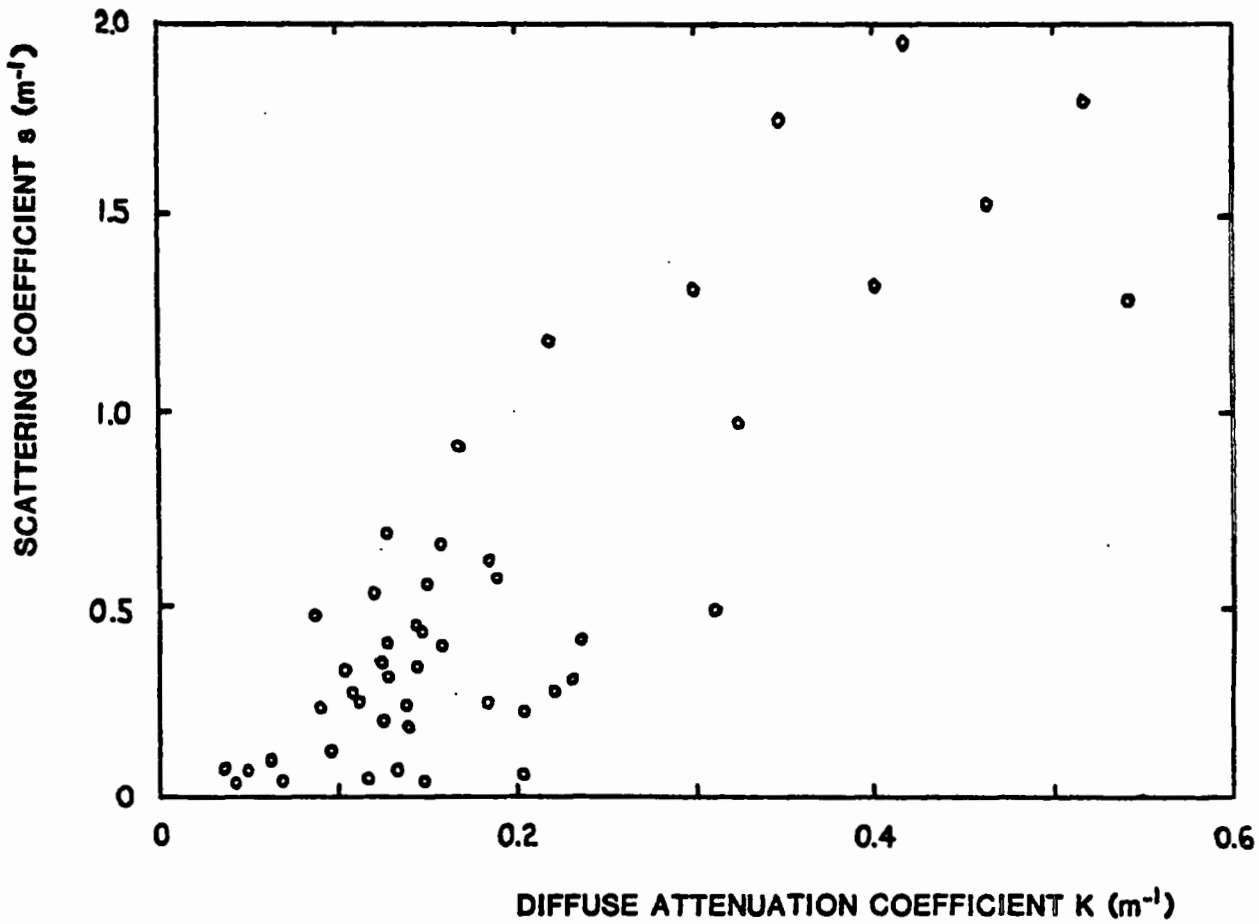

FIGURE 77. SCATTERING COEFFICIENT vs. DIFFUSE ATTENUATION COEFFICIENT MEASURED IN NATURAL WATERS

estimate $s=\omega_0\alpha\cong 0.8\alpha$. For actual cases where $0.6<\omega_0<0.9$, the double errors arising from this approximation are again far too large for the resulting estimates to be of practical use.

Two promising procedures involving the return waveforms have been investigated in some detail. These are the use of extrapolated volume backscatter amplitude to estimate s, and the use of bottom return pulse width to estimate sD. It will be seen that both procedures have attendant problems which cause them to be of questionable utility.

6.2 Extrapolated Backscatter Amplitude

The temporal shape of the volume backscatter return has been calculated for a triangular source pulse with a half width (FWHM), t_0. The model consists of multiple forward scattering, a single backscattering, and multiple forward scattering back to the surface. Let time be measured from a zero reference when the peak of the source pulse is at the air/sea interface. For time, t, define $x\equiv Kct$, where c is the speed of light in water. Similarly, $x_0\equiv Kct_0$. For $0<x<x_0$, the temporal form of the leading edge of the volume backscatter signal is $\rho_v(x)=\sigma(\pi)[1+(1-x-2e^{-x}+e^{-(x+x_0)})/x_0]/K$, where ρ_v is the backscatter reflectivity per unit solid angle, and $\sigma(\pi)$ is the value of the volume scattering function in the backscatter direction (at 180°). This waveform peaks at a time $x_p=\ln(2-e^{-x_0})$ with a peak reflectivity $\rho_v(x_p)=\sigma(\pi)[1-x_p/x_0]/2K$. For $x>x_0$ (the case where the entire pulse is in the water), the trailing edge of the backscatter return is described as $\rho_v(x)=\sigma(\pi)\ e^{-x}\ [e^{x_0}+e^{-x_0}-2]/2Kx_0$. Extrapolating this slope back to x=0 yields $\rho_v'(0)=\sigma(\pi)[e^{x_0}+e^{-x_0}-2]/2Kx_0$ which can be rewritten as $\rho_v'(0)=[\sigma(\pi)x_0/2K][(e^{x_0}+e^{-x_0}-2)/x_0^2]$. The latter term in brackets, for $0<K<0.5\ m^{-1}$, is equal to 1.05±0.025. The amplitude of the extrapolated backscatter reflectivity slope is thus $\rho_v'(0)\cong\sigma(\pi)x_0/2K=ct_0\sigma(\pi)/2$. The value of $\sigma(\pi)$ can thus be estimated from $\rho_v'(0)$ because c and t_0 are known.

An empirical relationship exists between $\sigma(\pi)$ and s in natural waters as seen in Fig. 78. The inset is a plot of Petzold (1972) data for a variety of typical water types from clear, deep ocean to fairly dirty harbor. The full plot includes three nearly opaque river samples (Whitlock 1981) for acedemic

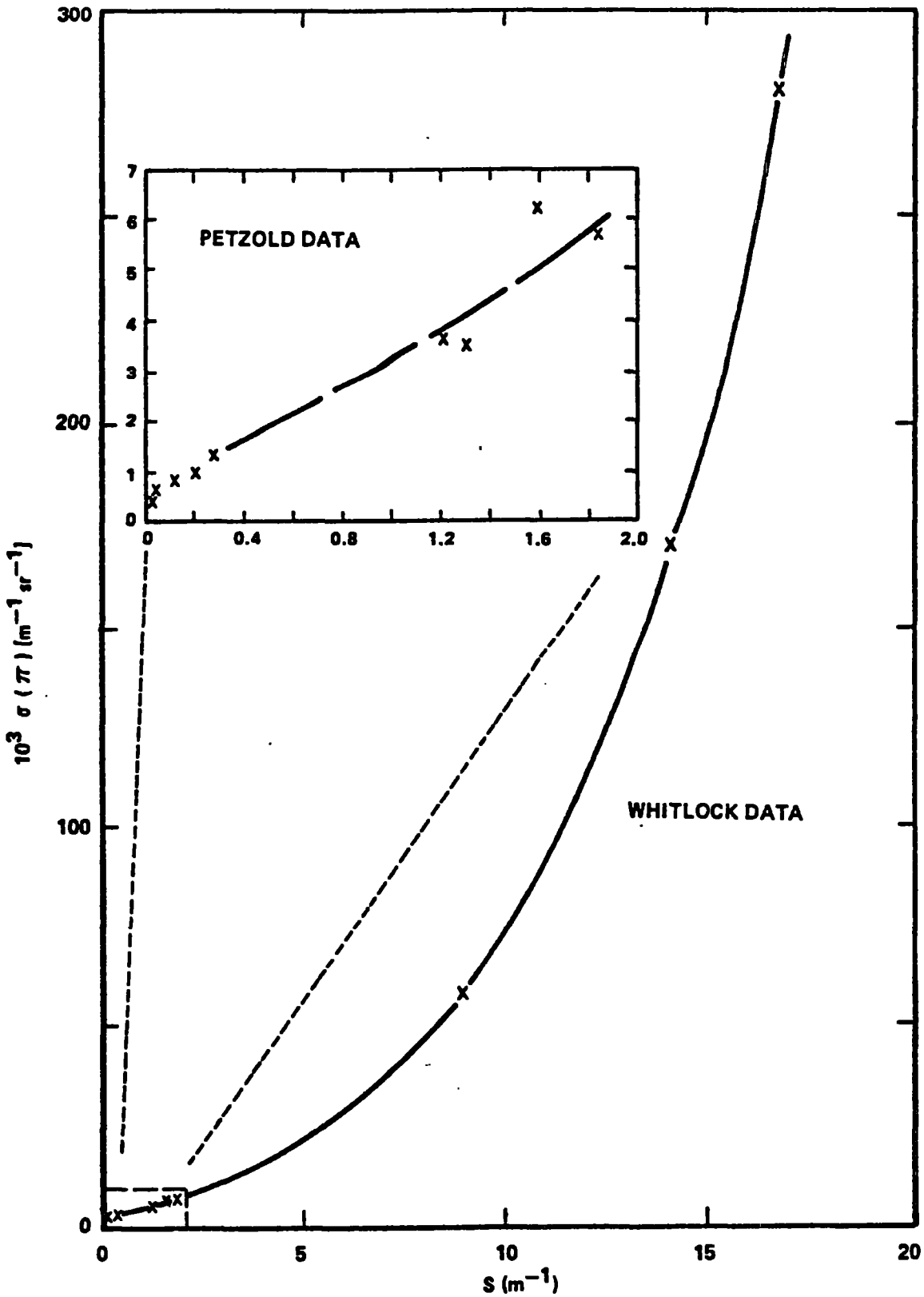

FIGURE 78. VOLUME SCATTERING FUNCTION AT 180° VERSUS SCATTERING COEFFICIENT

interest. Given $\sigma(\pi)$, s can be inferred from these "calibration" curves. The value of s can thus be estimated from the extrapolated backscatter amplitude.

This technique, although theoretically feasible, has several major practical drawbacks. The quantity of interest, $\rho_v'(0)$ is based on an absolute magnitude, i.e., a system voltage level, not a relative quantity such as a slope. Values of $\rho_v'(0)$ are obtained from the absolute magnitude of the extrapolated backscatter power $P_v'(0)$ via a relationship such as

$$P_v'(0) = \frac{m\ \eta_s\ \eta_a\ P_T\ A_R \cos^2\theta}{n_w^{\ 2}\ \ H^2}\ \rho_v'(0), \tag{10}$$

where m is the intercept factor from section 4.3.2 ($\cong$1.25),

η_s is the total optical system efficiency,

η_a is the two-way air path loss,

P_T is the transmitted peak power,

A_R is the receiver aperture area,

θ is the air nadir angle,

n_w is the index of refraction of water, and

H is the aircraft altitude.

Errors in estimating all these quantities lead to errors in the estimate of $\rho_v'(0)$ and subsequently $\sigma(\pi)$ and s. This means that the lidar system must be constantly maintained in a state of absolute radiometric calibration. Errors would arise from varying amplifier gains and PMT voltages, temperature-dependent optical signal variations, dirty optics, laser power fluctuations, etc.

In order for this technique to be of use, the waveforms must be recorded and returned for evaluation in post-flight data processing. The system must contain no nonlinear processes such as partial optical blocks or variable, real-time gain control which affect the shape of the backscatter tail. The laser source pulse must be sharply terminated so the tail of the surface return does not add significant energy into the backscatter signal. The technique will not work in relatively shallow water where the backscatter slope is too short to be accurately extrapolated and is contaminated by the surface and bottom return energies. Furthermore, the automated estimation of backscatter slopes from lidar waveforms would be difficult, time consuming,

and the results frequently imprecise. Finally, given $\sigma(\pi)$, the estimate of s depends on then s versus $\sigma(\pi)$ calibration curve. The existing Petzold data set would need to be further confirmed and expanded to ensure consistancy.

6.3 Bottom Return Pulse Width

It was noted by H. S. Lee (Moniteq 1983) that for nadir beam entry, NAVY phase function, and optical depths limited to a maximum of 16, the IRF pulse widths (at half the peak height) depend largely on the product $\omega_0 \alpha D$ (=sD) rather than on ω_0 and αD separately. This is the same dependence noted in the depth measurement biases. This leads to the concept that measurement of the bottom return pulse widths might be able to provide estimates of sD of sufficient precision to be used as an input (independent variable) for "actively" selecting an appropriate depth measurement bias predictor/corrector for each individual sounding.

In order for such a technique to be practical, a number of criteria must be met. The basic functionality must hold at all nadir angles of interest. The effect of varying phase function must be small, because it is uncontrollable and unknown. A procedure must be found to "deconvolve" the bottom return (i.e., the ERF) to yield an estimate of the IRF which is accurate enough to maintain the key depth scaling property. In addition, the effect of environmental effects on the pulse widths must be small and the added computing burden reasonable. As will now be seen, none of these requirements are fully met in practice.

The plots of pulse width versus sD for various ω_0 are basically "s" shaped and saturate at different levels of pulse width. Plots for different ω_0 tend to be similar to within sD's of ±1, but only to the extent that αD is limited to no more than about 16. For larger αD, the pulse widths for low ω_0 cases appear to approach saturation at lower pulse widths. These trends cannot be precisely defined because the simulation was not carried out for αD larger than 16 and because the precision of the estimates is reduced for low ω_0 due to the inherent loss of signal strength from increased relative absorption (higher K). A loss of sufficient signal strength tends to yield anomalously reduced pulse widths, and the technique will probably not work for

very weak signals. The trends in the results vary slightly with nadir angle, but the above description is applicable from 0° to at least 25°.

The phase function effect on pulse widths is larger than for depth measurement biases and, as seen in Fig. 79, is not insignificant. This occurs because the trailing edge of the bottom return pulse is more affected than the leading edge. More broadly scattering phase functions such as "NOS" result in longer trailing edges for given values of sD. For an average phase function between NAVY and NOS, the uncertainty in sD at high sD for a given pulse width is as large as ±2 for the defining cases. This alone is large, and when added to a number of other error sources, it becomes problemmatic. Also seen is the residual ω_0 effect.

Given a known source pulse, actual deconvolution of a bottom return is impractical because it is a time consuming and noisy process. A simple alternative is to measure the width of the bottom return and subtract the width of the source pulse, either in quadrature or linearly, to estimate the width of the underlying IRF. The results of these procedures are seen for a 20-m depth in Fig. 80 in comparison with the actual width of the IRF. It can be seen that neither approximation is valid for a full range of sD: linear subtraction works best at low sD, and quadrature subtraction works best at high sD. This effect is more evident at 10 m and less evident at 40 m. As a result, neither approximation will scale properly with depth across the full range of sD, because the estimate must behave like the IRF in order to scale properly. This effect has been confirmed by comparing results scaled from 10-m, 20-m, and 40-m ERFs. Since the biases, and hence bias correction errors, are larger at high sD, the quadrature subtraction is preferred, as seen in Fig. 81 for the 15°, NAVY case. It can be seen, for example, that the uncertainty in sD for depths from 10 m - 40 m becomes less than ±1.5 for sD>7. This is the region of interest where most bias variation occurs. Improved estimates of sD could be obtained by interpolation on depth if curves such as these were used for calibration.

For the procedure to yield reliable bias estimates, the pulse widths must be relatively independent of interfering effects. This is not the case. The bottom returns will also be broadened by bottom vegetation, bottom slope,

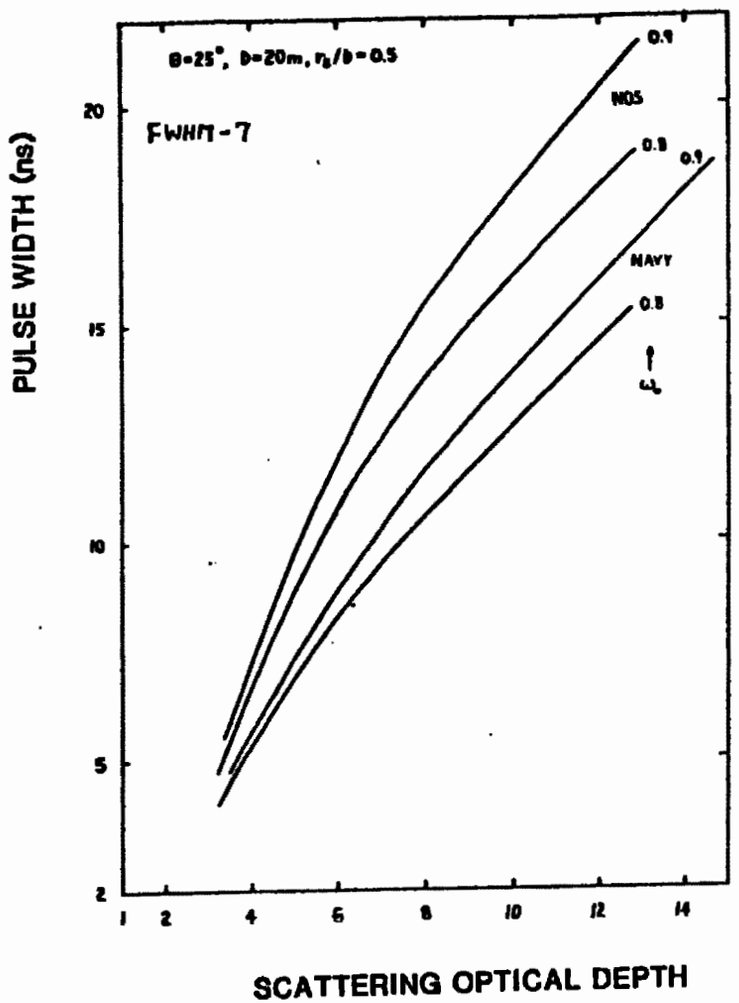

FIGURE 79. PHASE FUNCTION EFFECT ON PULSE WIDTH

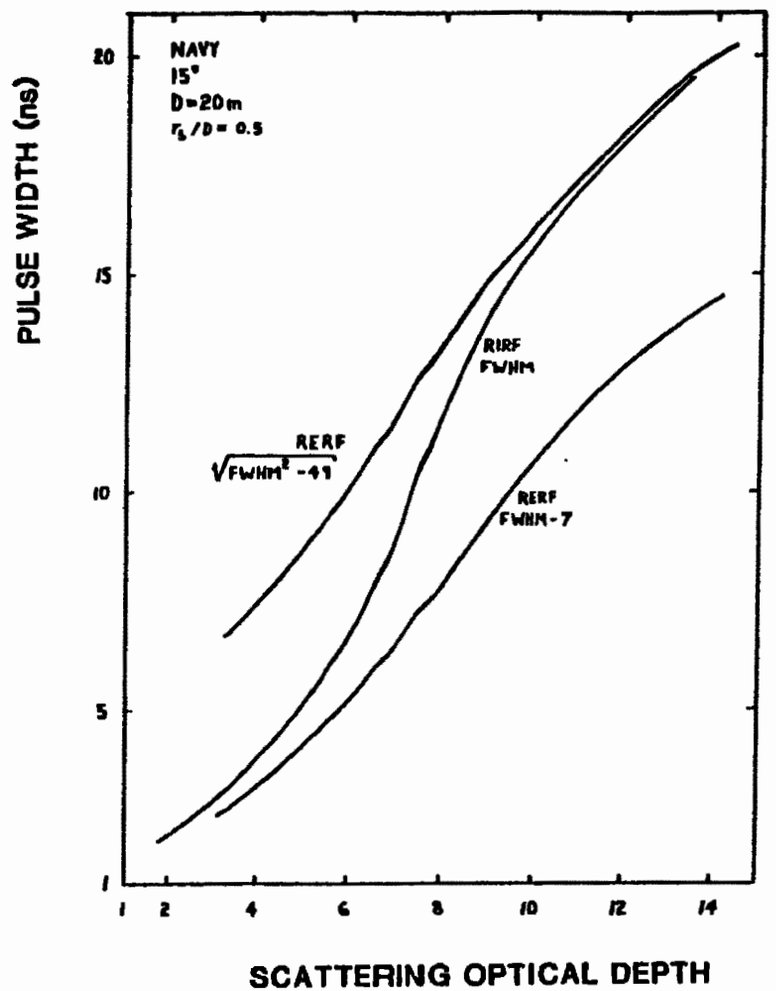

FIGURE 80. COMPARISON OF LINEAR AND QUADRATURE SOURCE WIDTH SUBTRACTION

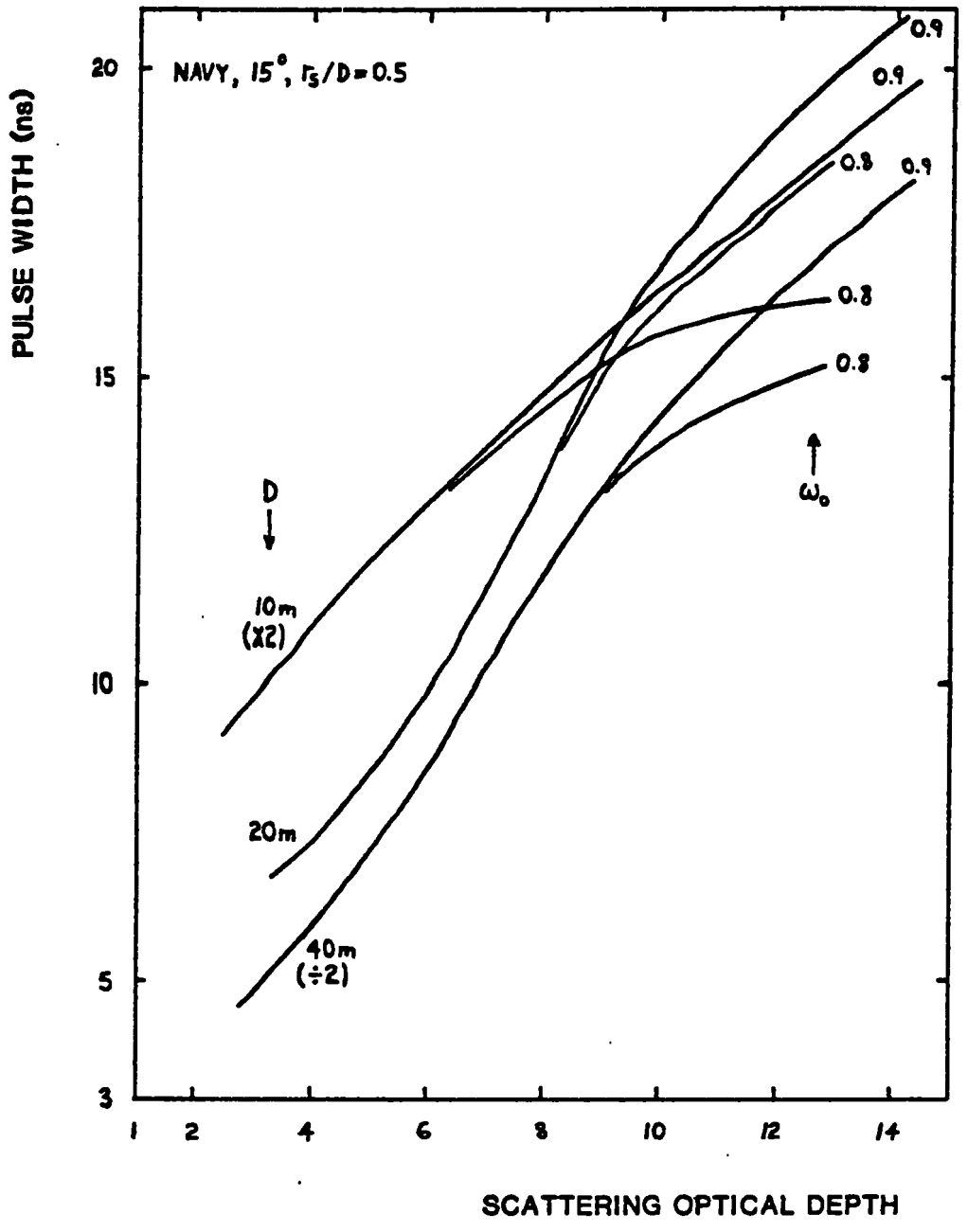

FIGURE 81. DEPTH SCALING WITH QUADRATURE SOURCE WIDTH SUBTRACTION

coral heads, and other such phenomena. The pulse is stretched because part of the return comes from the tops of the plants, and the rest comes from the "true" bottom. The measured depth will be a weighted average which depends on vegetation density and which is slightly shallower than the depth to the true bottom.

The presence or absence of bottom vegetation in a given sounding cannot be known a priori, and the effect can be doubly dangerous if pulse width is used for bias estimation. A broadened pulse implies higher sD. If the nadir angle and depth are such that biases are positive (deep), a higher apparent sD from vegetation broadening will lead to prediction of a deeper bias which will then be subtracted from the already somewhat shallow result.

Airborne lidar hydrography post-flight data processing in the field must be accomplished in no more than a small multiple (i.e., 2-3x) of the data acquisition time in order for the technique to be practical. The computing burden for just positioning and depth determination for the large number of soundings is staggering (Childs and Enabnit 1982). The use of active bias correctors on a pulse-to-pulse basis would require considerable added storage and processing time for estimating, scaling, and correcting pulse widths, computing sD, and computing and applying the bias correctors.

6.4 Bias Correction Conclusions

If the scattering optical depth can be adequately estimated on a pulse-to-pulse basis from the air, detailed bias predictions such as those tabulated in Appendix A can be interpolated or regressed to produce bias correctors. The ability to accurately or efficiently perform this estimation, however, is questionable.

The extrapolated backscatter magnitude technique for estimation of the scattering coefficient, though theoretically feasible, appears to be relatively impractical in application due to severe hardware, software, and accuracy problems.

Although pulse widths appear to be a plausible parameter from which scattering optical depth and hence propagation-induced depth measurement

biases could be estimated on a pulse-to-pulse basis, there are a number of error sources which, when summed, would significantly reduce the effectiveness of the estimation. The results, although not foolproof, could provide a limited measure of bias correction, particularly for non-optimal nadir angles, if the computing burden were acceptable. This may be the largest drawback. It is difficult to recommend a technique with such a low benefit/cost ratio.

It appears to be preferable to restrict the nadir angle of operation to a range appropriate for minimizing the biases (for the pulse processing and location algorithms selected). One can then apply simple, passive bias correctors as previously described in section 5.4 and quantified in section 5.5 (Eq.(9) and Table 2) for a 7-ns source pulse and LFT or HALS processing.

Procedures and bias tables in Guenther and Thomas (1981b) are outdated.

7.0 CONCLUSIONS

The impact of underwater light propagation mechanisms on the depth measurement accuracy of airborne laser hydrography has been investigated via a powerful new Monte Carlo computer simulation procedure. The simulation program provides a set of paths for downwelling photons arriving at the bottom for given sets of optical parameters and system variables. The resulting temporal and spatial distributions are used to compute impulse and actual source or "environmental" response functions at a distant, off-nadir, airborne receiver.

Scattering from particulate materials in the water column causes substantial spatial spreading of the beam. For typical operating optical depths, the half-power beam width is about 28°. Detection of small targets is enhanced by leading-edge pulse location algorithms. The resulting receiver field-of-view requirement for no significant reduction of peak return power is a full angle of 0.7D/H radians. For a 7-ns FWHM source pulse, the peak return power for a sufficient receiver FOV can be described as exponential with depth with a log slope of $-2nK\sec\phi$, where $1.1 < n(s, \omega_0, \theta) < 1.4$.

Depth measurement biases are calculated from environmental response functions, based on the 7-ns source pulse, for several typical signal processing and pulse location algorithms. These biases have been developed for bounding ranges of optical parameters in coastal waters and for all combinations of typical operational system variables. The only external input is the "phase function" scattering distribution. The sensitivity of the biases to phase function is small, but reported biases could differ somewhat from field data should the selected Petzold functions prove not to be representative at small angles.

Resultant biases may be either deep due to multiple scattering or shallow due to geometric undercutting, depending on nadir angle, water depth, and water optical properties. The strongest functionalities are with scattering optical depth, nadir angle, and signal processing and pulse location algorithms. It has been found that the net bias magnitudes can be large compared to international accuracy standards, and that the biases should therefore be corrected out of operational, raw depth data.

These bias predictions, in the form of look-up tables or regressions, can be used as "active" bias correctors for operational data on a pulse-to-pulse basis if the scattering optical depth can be estimated from the waveforms with sufficient accuracy. Because of the significant problems involved in estimating the scattering coefficient or scattering optical depth from the air, however, an alternate approach is presented. It has been shown that for certain limited ranges of scanner nadir angles, whose magnitudes depend on signal processing protocol, the bias variations due to unknown water optical parameters are less than ±15 cm at a 20-m depth and ±20 cm at a 30-m depth. These optimal nadir angles, in the 15° - 23° range, are appropriate for system operation in terms of desired swath width and aircraft altitude.

Constraining operations to preferred nadir angles via appropriate scanner design will permit "passive" bias correction using mean extrema biases which depend only on readily available information such as nadir angle, depth, and minor functionalities such as field of view and, for log/difference/CFD processing, signal-to-background ratio. For linear processing with a fractional threshold pulse location algorithm or for log/difference/CFD processing, the optimum nadir angles and mean extrema biases reported herein may be used for bias correction. For other signal processing and pulse location protocols, corresponding mean extrema bias functionalities must be calculated, and new matching nadir angles must be selected for minimum bias variation.

Systems operating without active bias correction or not within the optimal nadir angle range for passive bias correction will experience uncertainties in depth measurement biases, as functions of unknown water optical properties, which can be significantly larger than international hydrographic accuracy standards permit. Even with limited ground-truth measurements of optical properties, such errors are unavoidable due to the inherent patchiness of coastal waters.

8.0 ACKNOWLEDGMENTS

The authors express gratitude to H. Sang Lee for his insightful ideas and criticism and to the Defense Mapping Agency, the Office of Naval Research, and the Naval Ocean Research and Development Activity who provided funding for a portion of this effort.

9.0 REFERENCES

Chandrasekhar, S., 1960: Radiative Transfer. Dover Publications, New York, N. Y., 385 pp.

Childs, J. D. and Enabnit, D. B., 1982: User Requirements and a High Level Design of the Hydrographic Software / Data Processing Subsystem of an Airborne Laser Hydrography System. NOAA Technical Report OTES 11, National Oceanic and Atmospheric Administration, Rockville, Md., 192 pp.

Duntley, S. Q., 1971: Underwater Lighting by Submerged Lasers and Incandescent Sources. SIO Ref. 71-1, Scripps Institution of Oceanography, Visibility Laboratory, San Diego, Ca., 275 pp.

Gordon, H. R., 1974: Mie Theory Models of Light Scattering by Ocean Particulates. Suspended Solids in Water. Plenum Press, Ed. Ronald J. Gibbs, 73-86.

Gordon, H. R., Brown, O. B., and Jacobs, M. M., 1975: Computed Relationships Between the Inherent and Apparent Optical Properties of a Flat Homogeneous Ocean. Appl. Opt., 14, 417-427.

Gordon, H. R., 1982: Interpretation of Airborne Oceanic Lidar: Effects of Multiple Scattering. Appl. Opt., 21, 2996-3001.

Guenther, G. C., 1982: Effects of Detection Algorithm on Accuracy Degradation from Logarithmic and Difference Processing for Airborne Laser Bathymetric Returns. NOAA Technical Report OTES 6, National Oceanic and Atmospheric Administration, Rockville, Md., 38 pp.

Guenther, G. C. and Thomas, R. W. L., 1981a: Monte Carlo Simulations of the Effects of Underwater Propagation on the Penetration and Depth Measurement Bias of an Airborne Laser Bathymeter. NOAA Technical Memorandum OTES 1, National Oceanic and Atmospheric Administration, Rockville, Md., 144 pp.

Guenther, G. C. and Thomas, R. W. L., 1981b: Bias Correction Procedures for Airborne Laser Hydrography. NOAA Technical Report OTES 3, National Oceanic and Atmospheric Administration, Rockville, Md., 103 pp.

Guenther, G. C. and Thomas, R. W. L., 1981c: Simulations of the Impact of Inhomogeneous Water Columns on the Temporal Stretching of Laser Bathymetry Pulses. NOAA Technical Report OTES 2, National Oceanic and Atmospheric Administration, Rockville, Md., 39 pp.

Guenther, G. C. and Thomas, R. W. L., 1981d: Error Analysis of Pulse Location Estimates for Simulated Bathymetric Lidar Returns. NOAA Technical Report OTES 1, National Oceanic and Atmospheric Admin., Rockville, Md., 51 pp.

Jerlov, N. G., 1976: Marine Optics. Elsevier Scientific Pub. Co., Amsterdam.

Lee, H. Sang (Moniteq Ltd.), 1982, (personal communication).

Levis, C. A., Swarner, W. G., Prettyman, C., and Reinhardt, G. W., 1974: An Optical Radar for Airborne Use Over Natural Waters. Proc. Symp. on The Use of Lasers for Hydrographic Studies, Sept. 12, 1973, NASA/Wallops Flight Center, Wallops Island, Va., U.S. National Aeronautics and Space Administration, Wallops Island, Va., 67-80.

Moniteq Ltd., 1983: Determination of Parameters of Significance for Accuracy Optimization of a Scanning Lidar Bathymeter. Final Report, Canadian Hydrographic Service Contract, Concord, Ontario, Canada, 129 pp.

Petzold, T. J., 1972: Volume Scattering Functions for Selected Ocean Waters. SIO Ref. 72-78, Scripps Institution of Oceanography, Visibility Laboratory, San Diego, Calif., 79 pp.

Phillips, D. M. and Koerber, B. W., 1984: A Theoretical Study of an Airborne Laser Technique for Determining Sea Water Turbidity. Australian J. Phys., 37, 1, 75-90.

Plass, G. N. and Kattawar, G. W., 1971: J. Atmos. Sci, 28, 1187.

Prieur, L. and Morel, A., 1971: Etude Theorique du Regime Asymptotique. Cahiers Oceanographique, 23, 35.

Spanier, J. and Gelbard, E. M., 1969: Monte Carlo Principles and Neutron Transport Problems. Addison-Wesley Pub. Co., Reading, Mass.

Thomas, R. W. L. and Guenther, G. C., 1979: Theoretical Characterization of Bottom Returns for Bathymetric Lidar. Proceedings of the International Conference on Lasers '78, December 11 - 15, 1978, Orlando, Fla., Society for Optical and Quantum Electronics, McLean, Va., 48-59.

Timofeyeva, V. A. and Gorobets, F. I., 1967: On the Relationship Between the Attenuation Coefficients of Collimated and Diffuse Light Fluxes. Isv., Atmospheric and Oceanic Physics (Acad. of Sci., USSR), 3, 291-296 (166-169 in translation).

Wilson, W. H., 1979: Spreading of Light Beams in Ocean Water. Proc. SPIE Ocean Optics VI, October 23-25, 1979, Monterey, Calif.,Society of Photo-optical Instrumentation Engineers, Bellingham, Wash.,208, 64-72.

APPENDIX A. Bias Tabulation

Note: The mean biases presented here are averaged between NAVY and NOS phase functions as well as over various αD and ω_0 combinations. Single-scattering values of 0.8 and 0.6 were associated with NAVY, and 0.9 and 0.8 with NOS.

MEAN BIAS TABLES

Algorithm LFT ; Air nadir angle 0°

Depth (m)	Threshold (%)	FOV(R/D)	Scattering Optical Depth ($\omega_0 \alpha D$) 2	6	10	14
5	20	0.25	2	7	12	18
5	20	0.50	4	11	19	27
5	50	0.25	1	6	11	18
5	50	0.50	3	11	19	26
5	80	0.25	0	4	8	14
5	80	0.50	1	8	15	22
10	20	0.25	2	11	20	29
10	20	0.50	5	15	28	41
10	50	0.25	2	10	19	29
10	50	0.50	4	16	29	43
10	80	0.25	0	7	15	26
10	80	0.50	1	15	28	41
20	20	0.25	3	13	26	38
20	20	0.50	4	19	36	53
20	50	0.25	3	15	28	41
20	50	0.50	4	21	40	60
20	80	0.25	0	11	25	40
20	80	0.50	1	20	42	66
40	20	0.25	1	14	30	55
40	20	0.50	2	17	39	68
40	50	0.25	1	16	35	62
40	50	0.50	1	20	48	82
40	80	0.25	0	15	37	66
40	80	0.50	0	21	52	98

All biases in centimeters

MEAN BIAS TABLES

Algorithm LFT ; Air nadir angle 10°

Depth (m)	Threshold (%)	FOV(R/D)	Scattering Optical Depth ($\omega_0 \alpha D$) 2	6	10	14
5	20	0.25	1	6	11	17
5	20	0.50	3	9	15	22
5	50	0.25	0	4	11	18
5	50	0.50	2	8	16	23
5	80	0.25	-2	2	7	13
5	80	0.50	-1	6	13	20
10	20	0.25	1	8	17	26
10	20	0.50	2	12	23	33
10	50	0.25	-1	8	16	26
10	50	0.50	2	13	23	37
10	80	0.25	-3	5	13	23
10	80	0.50	-1	10	23	37
20	20	0.25	-2	8	18	28
20	20	0.50	-2	11	24	38
20	50	0.25	-3	8	21	34
20	50	0.50	-2	14	30	49
20	80	0.25	-6	7	20	35
20	80	0.50	-5	13	34	58
40	20	0.25	-13	-3	11	27
40	20	0.50	-12	-1	17	39
40	50	0.25	-12	2	21	40
40	50	0.50	-11	7	30	58
40	80	0.25	-14	5	30	56
40	80	0.50	-14	11	45	85

All biases in centimeters

MEAN BIAS TABLES

Algorithm LFT ; Air nadir angle 15°

Depth (m)	Threshold (%)	FOV(R/D)	Scattering Optical Depth ($\omega_0 \alpha D$) 2	6	10	14
5	20	0.25	1	4	9	14
5	20	0.50	2	8	13	19
5	50	0.25	0	4	8	13
5	50	0.50	1	7	14	20
5	80	0.25	-2	1	5	11
5	80	0.50	-1	4	10	16
10	20	0.25	-1	5	11	20
10	20	0.50	0	7	16	24
10	50	0.25	-1	5	13	21
10	50	0.50	0	8	18	28
10	80	0.25	-3	2	11	20
10	80	0.50	-2	7	18	28
20	20	0.25	-6	-2	5	13
20	20	0.50	-6	-2	6	15
20	50	0.25	-6	1	9	18
20	50	0.50	-6	1	11	22
20	80	0.25	-8	0	11	22
20	80	0.50	-7	4	18	32
40	20	0.25	-19	-24	-16	-2
40	20	0.50	-21	-31	-22	-8
40	50	0.25	-16	-11	2	17
40	50	0.50	-16	-12	2	24
40	80	0.25	-16	-5	14	37
40	80	0.50	-17	-4	18	43

All biases in centimeters

MEAN BIAS TABLES

Algorithm LFT ; Air nadir angle 20°

Depth (m)	Threshold (%)	FOV(R/D)	Scattering Optical Depth ($\omega_0 \alpha D$) 2	6	10	14
5	20	0.25	0	3	5	8
5	20	0.50	1	4	8	12
5	50	0.25	-1	2	4	8
5	50	0.50	0	4	8	13
5	80	0.25	-3	-1	1	4
5	80	0.50	-2	2	6	11
10	20	0.25	-2	0	3	7
10	20	0.50	-2	0	4	9
10	50	0.25	-3	1	4	9
10	50	0.50	-2	2	7	13
10	80	0.25	-4	-2	2	6
10	80	0.50	-4	1	8	15
20	20	0.25	-8	-15	-13	-5
20	20	0.50	-11	-21	-18	-10
20	50	0.25	-8	-8	-5	-1
20	50	0.50	-9	-11	-7	3
20	80	0.25	-9	-5	-1	3
20	80	0.50	-8	-6	1	8
40	20	0.25	-24	-60	-58	-41
40	20	0.50	-27	-76	-74	-57
40	50	0.25	-17	-26	-30	-25
40	50	0.50	-18	-32	-35	-27
40	80	0.25	-16	-16	-14	-10
40	80	0.50	-17	-14	-5	3

All biases in centimeters

MEAN BIAS TABLES

Algorithm LFT ; Air nadir angle 25°

Depth (m)	Threshold (%)	FOV(R/D)	Scattering Optical Depth ($\omega_0 \alpha D$) 2	6	10	14
5	20	0.25	-1	1	3	5
5	20	0.50	0	2	4	6
5	50	0.25	-2	0	2	4
5	50	0.50	-1	1	4	6
5	80	0.25	-4	-3	-1	2
5	80	0.50	-3	-1	2	5
10	20	0.25	-4	-5	-5	-5
10	20	0.50	-5	-9	-9	-8
10	50	0.25	-5	-4	-1	2
10	50	0.50	-5	-5	-2	3
10	80	0.25	-5	-5	-1	3
10	80	0.50	-5	-3	1	8
20	20	0.25	-12	-28	-32	-35
20	20	0.50	-15	-42	-48	-50
20	50	0.25	-10	-15	-18	-19
20	50	0.50	-11	-21	-21	-18
20	80	0.25	-10	-11	-10	-9
20	80	0.50	-10	-11	-7	-3
40	20	0.25	-32	-87	-98	-104
40	20	0.50	-35	-118	-140	-143
40	50	0.25	-18	-46	-61	-71
40	50	0.50	-23	-48	-57	-64
40	80	0.25	-13	-29	-41	-47
40	80	0.50	-19	-25	-19	-10

All biases in centimeters

MEAN BIAS TABLES

Algorithm: log / difference (Δ = 6ns) / CFD (δ = 6ns)

Air nadir angle 0°

Depth (m)	Pm/B	FOV(R/D)	Scattering Optical Depth ($\omega_0 \alpha D$) 2	6	10	14
5	1	0.25	21	35	46	52
5	1	0.50	21	40	49	55
5	10	0.25	7	16	23	30
5	10	0.50	8	19	27	35
10	1	0.25	18	32	43	51
10	1	0.50	20	37	49	57
10	10	0.25	6	14	23	30
10	10	0.50	7	18	27	37
20	1	0.25	15	30	43	54
20	1	0.50	16	34	48	60
20	10	0.25	5	13	23	34
20	10	0.50	6	15	28	41
40	1	0.25	11	25	41	57
40	1	0.50	11	26	45	65
40	10	0.25	2	7	20	40
40	10	0.50	2	7	21	43

All biases in centimeters

MEAN BIAS TABLES

Algorithm: log / difference (Δ = 6ns) / CFD (δ = 6ns)

Air nadir angle 10°

Depth (m)	Pm/B	FOV(R/D)	Scattering Optical Depth ($\omega_0 \alpha D$) 2	6	10	14
5	1	0.25	18	33	42	48
5	1	0.50	21	36	45	51
5	10	0.25	6	14	22	29
5	10	0.50	7	17	26	32
10	1	0.25	15	28	37	44
10	1	0.50	17	32	41	46
10	10	0.25	4	11	19	26
10	10	0.50	4	14	22	30
20	1	0.25	9	21	29	35
20	1	0.50	9	22	31	37
20	10	0.25	-2	5	12	19
20	10	0.50	-2	6	15	23
40	1	0.25	-6	0	9	21
40	1	0.50	-6	1	11	22
40	10	0.25	-20	-19	-9	1
40	10	0.50	-20	-18	-9	2

All biases in centimeters

MEAN BIAS TABLES

Algorithm: log / difference (Δ = 6ns) / CFD (δ = 6ns)

Air nadir angle 15°

Depth (m)	Pm/B	FOV(R/D)	Scattering Optical Depth ($\omega_0 \alpha D$) 2	6	10	14
5	1	0.25	17	29	36	41
5	1	0.50	19	31	38	42
5	10	0.25	5	12	17	22
5	10	0.50	6	14	20	25
10	1	0.25	12	21	28	32
10	1	0.50	12	21	28	32
10	10	0.25	1	6	11	16
10	10	0.50	1	5	10	16
20	1	0.25	1	4	8	16
20	1	0.50	0	1	4	9
20	10	0.25	-9	-10	-7	0
20	10	0.50	-12	-16	-11	-4
40	1	0.25	-22	-42	-40	-32
40	1	0.50	-36	-54	-46	-39
40	10	0.25	-50	-63	-59	-44
40	10	0.50	-72	-77	-67	-57

All biases in centimeters

MEAN BIAS TABLES

Algorithm: log / difference (Δ = 6ns) / CFD (δ = 6ns)

Air nadir angle 20°

Depth (m)	Pm/B	FOV(R/D)	Scattering Optical Depth ($\omega_0 \alpha D$) 2	6	10	14
5	1	0.25	15	23	29	32
5	1	0.50	15	25	30	33
5	10	0.25	4	9	13	16
5	10	0.50	4	10	14	18
10	1	0.25	7	10	13	16
10	1	0.50	6	9	12	14
10	10	0.25	-1	-3	0	4
10	10	0.50	-3	-5	-1	4
20	1	0.25	-3	-18	-17	-6
20	1	0.50	-7	-29	-27	-20
20	10	0.25	-19	-36	-34	-21
20	10	0.50	-37	-49	-45	-38
40	1	0.25	-105	-108	-98	-85
40	1	0.50	-152	-143	-135	-134
40	10	0.25	-121	-121	-118	-114
40	10	0.50	-168	-162	-157	-151

All biases in centimeters